Domains and domain dynamics in fluoritestructured ferroelectrics

Cite as: Appl. Phys. Rev. 8, 021312 (2021); https://doi.org/10.1063/5.0047977 Submitted: 18 February 2021 • Accepted: 17 March 2021 • Published Online: 30 April 2021

🗓 Dong Hyun Lee, 🔟 Younghwan Lee, Kun Yang, et al.









ARTICLES YOU MAY BE INTERESTED IN

Next generation ferroelectric materials for semiconductor process integration and their applications

Journal of Applied Physics 129, 100901 (2021); https://doi.org/10.1063/5.0037617

Ferroelectricity in hafnium oxide thin films

Applied Physics Letters 99, 102903 (2011); https://doi.org/10.1063/1.3634052

The origin of ferroelectricity in $Hf_{1-x}Zr_xO_2$: A computational investigation and a surface energy model

Journal of Applied Physics 117, 134109 (2015); https://doi.org/10.1063/1.4916707





Domains and domain dynamics in fluorite-structured ferroelectrics

Cite as: Appl. Phys. Rev. **8**, 021312 (2021); doi: 10.1063/5.0047977 Submitted: 18 February 2021 · Accepted: 17 March 2021 · Published Online: 30 April 2021







Dong Hyun Lee, Dong H

AFFILIATIONS

School of Materials Science and Engineering, Pusan National University, 2, Busandaehak-ro-63-beon-gil, Geumjeong-gu, Busan 46241, South Korea

ABSTRACT

Ferroelectricity in fluorite-structured ferroelectrics such as HfO₂ and ZrO₂ has been attracting increasing interest since its first publication in 2011. Fluorite-structured ferroelectrics are considered to be promising for semiconductor devices because of their compatibility with the complementary metal—oxide—semiconductor technology and scalability for highly dense information storage. The research on fluorite-structured ferroelectrics during the first decade of their conceptualization has been mainly focused on elucidating the origin of their ferroelectricity and improving the performance of electronic devices based on such ferroelectrics. Furthermore, as is known, to achieve optimal performance, the emerging biomimicking electronic devices as well as conventional semiconductor devices based on the classical von Neumann architecture require high operating speed, sufficient reliability, and multilevel data storage. Nanoscale electronic devices with fluorite-structured ferroelectrics serve as candidates for these device systems and, thus, have been intensively studied primarily because in ferroelectric materials the switching speed, reliability, and multilevel polarizability are known to be strongly correlated with the domains and domain dynamics. Although there have been important theoretical and experimental studies related to domains and domain dynamics in fluorite-structured ferroelectrics, they are yet to be comprehensively reviewed. Therefore, to provide a strong foundation for research in this field, herein, domains, domain dynamics, and emerging applications, particularly in neuromorphic computing, of fluorite-structured ferroelectrics are comprehensively reviewed based on the existing literature.

© 2021 Author(s). All article content, except where otherwise noted, is licensed under a Creative Commons Attribution (CC BY) license (http://creativecommons.org/licenses/by/4.0/). https://doi.org/10.1063/5.0047977

TABLE OF CONTENTS

I. INTRODUCTION	2
II. POLYMORPHISM AND DOMAINS IN FLUORITE-	
STRUCTURED FERROELECTRICS	2
A. Polymorphism of fluorite-structured	
ferroelectrics	2
B. Crystallographic hierarchy and polarization	
switching pathways in fluorite-structured	
ferroelectrics	5

C. Domains in fluorite-structured ferroelectrics	7
III. DOMAIN DYNAMICS AND POLARIZATION	
SWITCHING KINETICS	13
A. Classical theory of domain dynamics	13
B. Switching kinetics for fluorite-structured	
polycrystalline thin films	13
C. Polarization switching of fluorite-structured	
ferroelectrics in nanoscale devices	19
IV. NEUROMORPHIC COMPUTING BASED ON	

FLUORITE-STRUCTURED FERROELECTRICS.....

21

²Department of Materials Science and Engineering, North Carolina State University, Raleigh, North Carolina 27695, USA

³Technology Licensing Office, Institute for Research and Industry Cooperation, Pusan National University, 2, Busandaehak-ro-63-beon-gil, Geumjeong-gu, Busan 46241, South Korea

⁴NaMLab gGmbH, Noethnitzer Str. 64, Dresden, Germany

⁵Department of Nanoelectronics, Dresden University of Technology, Dresden, Germany

a) Electronic addresses: jacobjones@ncsu.edu and uwe.schroeder@namlab.com

b) Author to whom correspondence should be addressed: minhyukpark@pusan.ac.kr

A. Neuromorphic computing based on	
ferroelectricity	21
B. Artificial synapses based on fluorite-structured	
ferroelectrics	22
C. Artificial neurons based on fluorite-structured	
ferroelectrics	26
D. Perspectives on neuromorphic computing based	
on fluorite-structured ferroelectrics	27
V. CONCLUSION	28
AUTHORS' CONTRIBUTIONS	29

I. INTRODUCTION

Emerging fluorite-structured ferroelectrics, such as hafnium oxide (HfO₂) and zirconium oxide (ZrO₂) and their solid solutions, have been intensively studied by numerous research groups to elucidate the origin of their unexpected ferroelectricity as well as to improve the performance of electronic devices based on them. From device engineering perspectives, a ferroelectric field-effect transistor (FeFET) with a 28-nm-long channel and a ferroelectric fully depleted siliconon-insulator (FDSOI) device² have been demonstrated, thereby proving their higher scalability and compatibility with the complementary metal-oxide-semiconductor (CMOS) technology compared to those of conventional ferroelectric materials. Moreover, ferroelectric tunnel junctions (FTJs) with bistable or multistable tunneling electroresistances have been demonstrated.3-6 The ferroelectric random access memory (FeRAM) with classical 1 transistor-1 capacitor cells was fabricated by SONY by adopting ferroelectric HfO2 capacitive layer. The utilization of nonvolatile FeFETs, FTJs, and FeRAMs with fluorite-structured ferroelectrics in various futuristic computing systems has been suggested, such as in logic memory hybrid devices for improving the energy efficiency of classical computing systems as well as in neuronal or synaptic devices for developing novel neuromorphic computing systems beyond the state-of-the-art von Neumann computing architecture. It is believed that the discovery of industryfriendly fluorite-structured ferroelectrics is a breakthrough in ferroelectric nonvolatile memory devices although some issues such as limited endurance, low operating speed, limited retention, and performance uniformity in large-scale integrated circuits remain. Solutions and strategies to overcome these issues have been intensively reviewed in recent reports from the viewpoint of materials science and engineering.

Understanding the fundamental physics and chemistry of emerging fluorite-structured ferroelectrics is essential to make an industrial breakthrough for the fabrication of mass-producible commercial products by overcoming the previously mentioned device-related issues. From a crystallographic perspective, the formation of a polar orthorhombic phase (*Pca2*₁) in most polycrystalline films¹⁰⁻¹² or a rhombohedral phase (*R3*) in several epitaxial films¹³ is now generally accepted as the origin of ferroelectricity in fluorite-structured ferroelectrics. The formation of these metastable polar phases could be attributed to the thermodynamic stabilization induced by various factors, ^{14,15} such as doping, surface energy effect, stress/strain, and defect/kinetic mechanism, that suppress the formation of a stable monoclinic phase with a large kinetic energy barrier during processing. ^{16–19} Additionally, the polymorphism arising from the nanoscale competition among several different crystalline phases has been suggested to be strongly correlated

with various sources of spatial inhomogeneities, including doping concentration, $^{20-23}$ defect concentration, $^{24-26}$ and local strain. 27

In addition to the crystalline phase consideration, the domains and domain dynamics of fluorite-structured ferroelectrics have gained considerable research attention. Because nonvolatile ferroelectric memories utilize two or more switchable polarization states, the domains and domain dynamics are deterministic for the high performance of nonvolatile ferroelectric memories, in terms of parameters such as operating speed, reliability, and uniformity in large-scale integration. 8,5,28,29 Although these properties are strongly correlated with the domain and domain dynamics of ferroelectrics, studies on fluoritestructured ferroelectrics have not been comprehensively reviewed to date. Therefore, the domains, domain dynamics, and polarization switching kinetics in fluorite-structured ferroelectrics are reviewed herein, and some perspectives on semiconductor devices for neuromorphic computing, which is considered to be one of the most promising applications for futuristic computing, are provided. Section II provides a comprehensive review of the polymorphism associated with nanoscale competition among different phases, theoretical studies on switching pathways, and theoretical and experimental works on HfO₂ and ZrO2 domains. Section III focuses on the domain wall dynamics and switching kinetics in ferroelectric HfO2 and ZrO2 polycrystalline films studied through both classical and emerging physical models. Section IV reviews previous and recent studies on the applications of fluorite-structured ferroelectrics and summarizes the perspectives on future research topics and the applications for fluorite-structured ferroelectrics, particularly in neuromorphic computing.

II. POLYMORPHISM AND DOMAINS IN FLUORITE-STRUCTURED FERROELECTRICS

A. Polymorphism of fluorite-structured ferroelectrics

The electronic structures of Hf and Zr are known to be ([Xe]4f¹⁴5d²6s²) and ([Kr]4d²5s²), respectively.³⁰ Although there is a distinctive difference between Hf and Zr, whereby a closed subshell of 4f electrons exists only in Hf, the number of outermost electrons for both elements is the same, i.e., four. The ionic radii of Hf (0.83 Å for coordination number of 8) and Zr (0.84 Å for coordination number of 8)³¹ are approximately the same owing to an effect referred to as the lanthanide contraction, which results from the poor shielding of nuclear charges by 4f electrons. They are considered to be rather identical to any other two congeneric elements, 32 showing considerable similarities in their chemical and physical properties. Consequently, it is unsurprising that the oxide form of these atoms would also exhibit similar chemical and physical properties. Notably, crystalline HfO2 and ZrO2 exhibit multiple crystallographic structures under different conditions, although their chemical formulas are consistent, which is denoted as polymorphism. Furthermore, HfO2 and ZrO2 polymorphs share similar crystallographic structures in the same space group, which is why they are often described as isostructural species. The types of their crystallographic structures are shown in Fig. 1; they are categorized mainly as monoclinic (P2₁/c), tetragonal (P4₂/nmc), cubic $(Fm\overline{3}m)$, and orthorhombic phases $(Pca2_1, Pbca, etc.)$, all of which can be derived from the fluorite structure. Moreover, the crystallographic structure of HfO2 phases is identical to that of ZrO2, as shown in Fig. 1, with relatively small differences in their lattice parameters and atomic positions. Since ferroelectricity in crystalline materials depends on non-centrosymmetric elements, it is important to have a deep

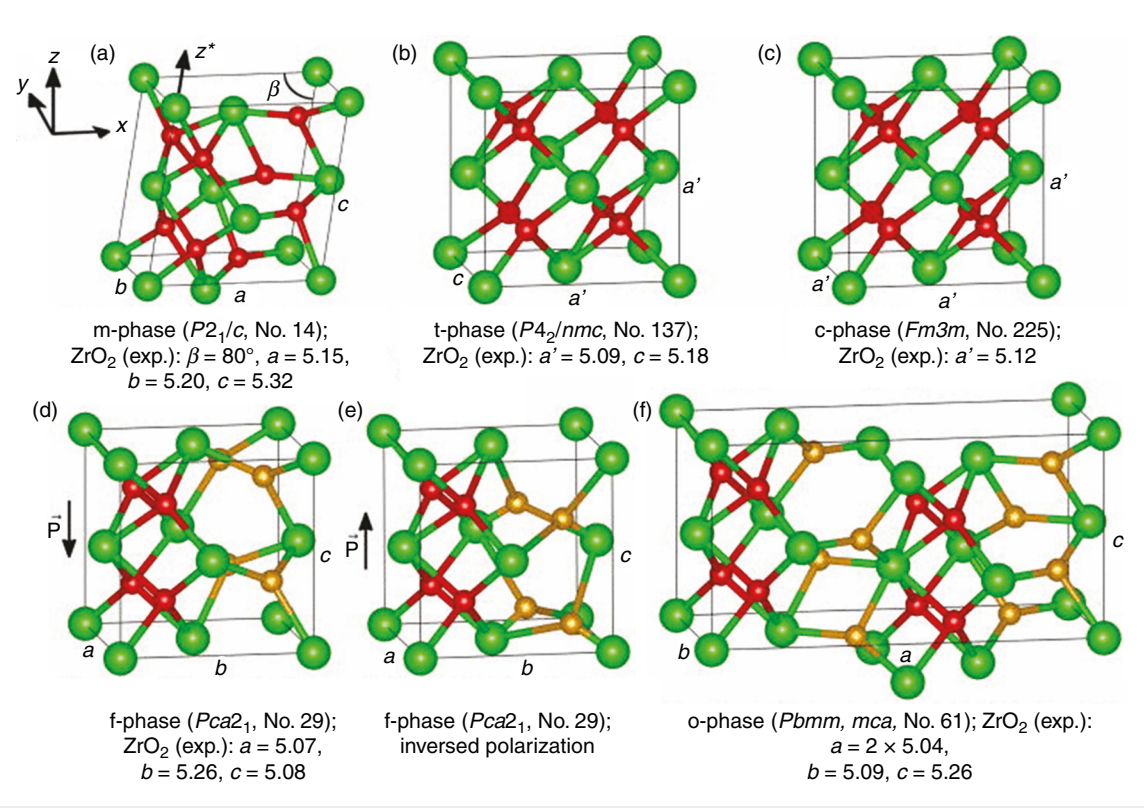


FIG. 1. Crystallographic structures and experimental lattice constants in Å for ZrO₂. Zr atoms are represented in green (big) and O atoms in red (small). In the f-phases, the O atoms mainly responsible for the polarization are highlighted by a golden color. To illustrate the relationship between the f- and o-phases, the corresponding O atoms are highlighted by using a golden color in the o-phase (which is also known as the *Pbca* phase) as well. The polarization axis of the two f-phase cells is marked by black arrows (P). Reproduced from Materlik *et al.*, J. Appl. Phys. **117** (13), 134109 (2015)¹⁴ with the permission of AIP Publishing.

understanding of the polymorphs of HfO₂ and ZrO₂, as well as the conditions under which they can appear. We first discuss the temperature–pressure phase diagram of HfO₂ and ZrO₂.

The stable polymorphs of HfO₂ and ZrO₂ depend on both temperature and pressure. As shown in Figs. 2(a) and 2(b), at atmospheric pressure (\sim 101 kPa), the monoclinic phase ($P2_1/c$) appears over the lowest temperature ranges for both HfO₂ and ZrO₂, which indicates that the monoclinic phase is the most stable phase below \sim 1973 and ~1373 K for HfO2 and ZrO2, respectively. The tetragonal phase $(P4_2/nmc)$ appears at \sim 1973 and \sim 1373 K for HfO₂ and ZrO₂, respectively, followed by the cubic phase $(Fm\overline{3}m)$, which appears at \sim 2773 and \sim 2673 K for HfO₂ and ZrO₂, respectively. ^{33,34} When the pressure exceeds 4 GPa at a temperature below ~1573 and ~873 K for HfO₂ and ZrO2, respectively, the orthorhombic phase appears for both oxides, which is referred to as the orthorhombic-I phase (Pbca), wherein Hf ions are in a sevenfold coordination. As the pressure increases above 14 and 13 GPa for HfO2 and ZrO2, respectively, another orthorhombic phase, which is known as the orthorhombic-II phase (Pnma, not shown), appears, wherein the Hf ions are in a ninefold coordination. 33,34 It should be noted that all the above-mentioned equilibrium phases of HfO₂ and ZrO₂ are known to be centrosymmetric and hence, nonpolar, thereby suggesting that ferroelectricity cannot be induced in either HfO2 or ZrO2 under equilibrium conditions and bulk forms.

From the temperature-pressure phase diagrams of HfO2 and ZrO₂ presented in Figs. 2(a) and 2(b), we can observe two commonalities: (1) both oxides show similar phase transition trends (monoclinic \rightarrow tetragonal \rightarrow cubic) with increasing temperature at 0 GPa and (2) the orthorhombic phases of both oxides appear under extreme conditions (e.g., high pressure). From commonality (1), we can expect that an isomorphous binary phase diagram between HfO2 and ZrO2 exists at atmospheric pressure. Figure 2(c) shows this binary phase diagram of HfO₂-ZrO₂ as a function of composition and temperature at atmospheric pressure. As expected, the binary phase diagram indicates that HfO₂-ZrO₂ shows a complete solid solution as well as consistent phases and phase transitions across the entire compositional range. None of the phases shown in the phase diagram of HfO2-ZrO2 are non-centrosymmetric, which suggests that HfO2, ZrO2, or the mixture of the two cannot exhibit ferroelectricity over any composition and temperature range at atmospheric pressure. Furthermore, none of the non-centrosymmetric phases that allow ferroelectricity were reported in the other binary phase diagrams between HfO2 and oxides, such as SiO_{2}^{35} $Al_{2}O_{3}^{36}$ $La_{2}O_{3}^{37}$ $Gd_{2}O_{3}^{38}$ $Y_{2}O_{3}^{39}$ SrO_{3}^{40} and $Sc_{2}O_{3}^{41}$ thereby implying that the inducement of ferroelectricity in bulk HfO2 (or ZrO₂) is not expected upon adding different chemicals or changing temperatures at atmospheric levels. Although the binary phase diagrams between both HfO2 and other oxides and HfO2 and ZrO2 do not show any non-centrosymmetric phases, it should be noted that the

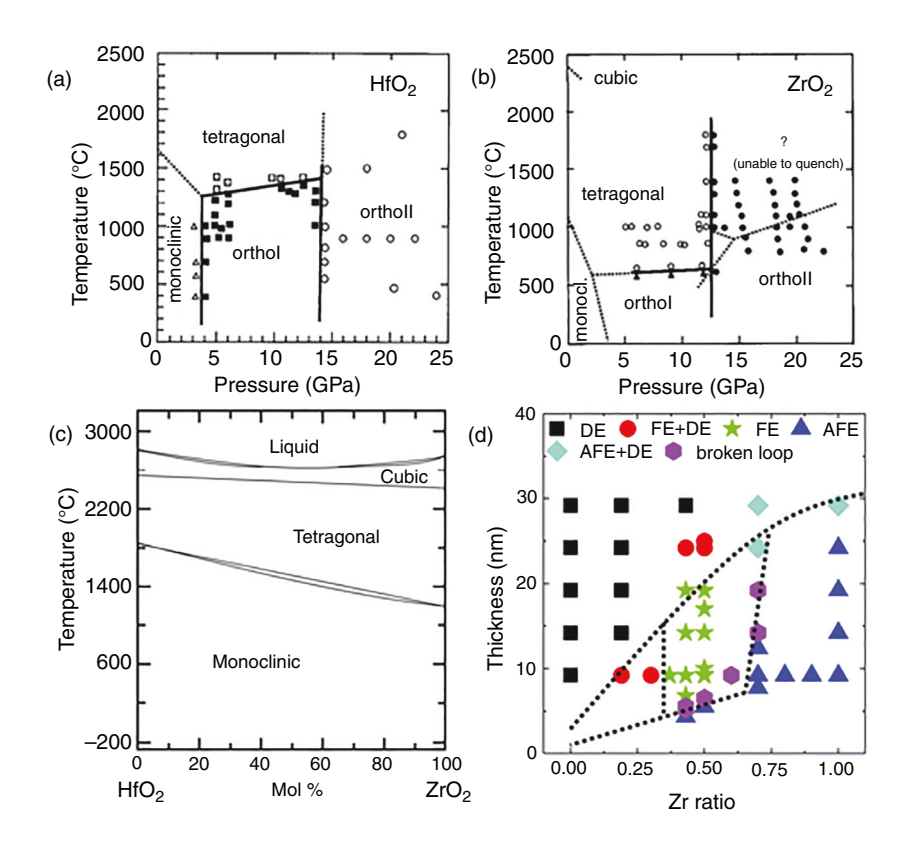


FIG. 2. Pressure-temperature phase diagram of bulk (a) HfO2 and (b) ZrO2. (c) Calculated binary phase diagram of bulk HfO₂ and ZrO₂¹⁰⁵ using thermodynamic data from the literature. Experimental map of P-E characterization results of HfO₂-ZrO₂ thin films with various thicknesses. Note that dielectric (DE)-, ferroelectric (FE)-, and antiferroelectric (AFE)-like hysteresis loops were observed in the experiment conducted by Park et al.88 The crystalline phase of each property can be referred to as monoclinic, polar orthorhombic, and tetragonal for DE, FE, and AFE, respectively. Reproduced with permission from (a) Ohtaka et al., J. Am. Ceram. Soc. **84**(6), 1369–1373 (2001). Copyright 2001, John Wiley and Sons; (b) Ohtaka et al., Phys. Rev. B **63**(17), 174108 (2001).³ Copyright 2001, The American Physical Society; (c) Phase Equilibria Online Database (NIST Standard **Diagrams** Reference Database 31), the ACerS and the NIST, Figure Numbers Zr-186, and (d) Park et al., Nanoscale 9(28), 9973-9986 (2017). Copyright 2017, Royal Society of Chemistry.

discussion in the HfO₂-ZrO₂ system cannot be directly applied to other oxides systems because other oxides do not exhibit fluorite structure like HfO₂ or ZrO₂. From commonality (2), it is reasonable to hypothesize that orthorhombic phases would appear when HfO₂, ZrO₂, or a mixture of the two is fabricated in a form that contains high internal stress/strain, e.g., as can be achieved in thin films.

In 2011, ferroelectricity was first reported in a 10-nm-thick Sidoped HfO₂ thin film by Boescke and co-workers, ¹⁰ and the discovery of unexpected ferroelectricity in HfO2 initiated intensive research on fluorite-structured ferroelectrics. 16-18,42-44 They reported that HfO₂ thin films exhibited ferroelectric hysteresis from the polarizationelectric field (P-E) measurement and butterfly-like curves from the small-signal capacitance-voltage (C-V) measurement, demonstrating unambiguous evidence of ferroelectricity in a material. However, as established in the phase diagram of HfO2, the appearance of ferroelectricity could not be explained on the basis of the presence of the aforementioned phases at any realizable temperature and pressure because they were all centrosymmetric phases. By employing the grazing incidence x-ray diffraction patterns of the HfO2 films, Boescke et al. suggested that the polar orthorhombic phase [Pca2₁, Figs. 1(d) and 1(e)] is the crystallographic origin of the unexpected ferroelectricity. Notably, the polar orthorhombic phase (Pca21) was first reported in partially stabilized Mg-doped ZrO2 at 30 K by Kisi and co-workers in 1989. 45 Following the work of Boescke et al., other researchers have demonstrated that the differences in the free energy of several polymorphic phases are sufficiently small to be overcome, thereby resulting in nanoscale competition among the polymorphic phases. 14,20,46 The polar orthorhombic phase (Pca2₁) can appear because of a suitable combination of driving factors, such as volumetric confinement, ¹⁰ dopant concentration, strain, ^{20–23} and defect concentration, ^{24–26} whose distributions are probably inhomogeneous in polycrystalline thin films. ⁴⁶ Consequently, it is now generally accepted that ferroelectricity is a result of the evolution of the polar orthorhombic phase (*Pca*2₁) in HfO₂ (or ZrO₂). Numerous theoretical and experimental studies also support that the polar orthorhombic phase (*Pca*2₁) exists in HfO₂ thin films and is responsible for the ferroelectric response. ^{11–14,20,23,26,46–48}

The ferroelectricity and polar phase of doped HfO2 or HfO₂-ZrO₂ thin films have been reproduced by several independent research groups. 23,48-57 Figure 2(d) shows an experimental map of the P-E characteristics of HfO2-ZrO2 thin films via atomic layer deposition (ALD).44 When the film is HfO2-rich, the P-E response only shows a dielectric behavior [linear and non-hysteretic, denoted as DE in Fig. 2(d)], which would originate from the stable monoclinic phase. In a ZrO₂-rich film, the P-E response shows an antiferroelectric-like behavior [pinched hysteresis, denoted as AFE in Fig. 2(d)], which is believed to be caused by the metastable tetragonal phase. Meanwhile, strong ferroelectricity is observed via an open P-E hysteresis loop at 50% of the Zr/(Hf+Zr) composition, which is believed to be induced by the metastable polar orthorhombic phase. However, the ferroelectricity shown at 50% of the Zr/(Hf+Zr) composition becomes more enhanced as the thickness decreases, which explains the applicability of this material in applications involving the miniaturization of electronic devices. It is believed that the surface, interface, and grain boundary energies play an important role in stabilizing the metastable polar orthorhombic phase. 14,44,58 Materlik et al. 14 suggested that the

surface and bulk energies of the polar orthorhombic phase are between those of the monoclinic and tetragonal phases. Hence, the formation of the polar orthorhombic phase is expected within a specific thickness range, e.g., <30 nm, as shown in Fig. 2(d), at the transition from the monoclinic to tetragonal phase with decreasing film thickness.1-However, it should be noted that studies on thickness-dependent ferroelectric HfO2-ZrO2 thin films work well on films fabricated via ALD. In the case of chemical solution-deposited ZrO₂ thin films, ferroelectricity could be observed even in films as thick as 390 nm. 59,60 For the case of epitaxial Y-doped HfO2 films, ferroelectricity could be observed even in films that are \sim 1000 nm thick.⁶¹ We could infer that the thickness range for the formation of the polar orthorhombic phase with resulting ferroelectricity is strongly dependent on the deposition method. Because numerous studies employ ALD techniques to fabricate ferroelectric HfO₂–ZrO₂ thin films, we focus on the case of ALDfabricated ferroelectric HfO₂–ZrO₂ thin films throughout this paper.

The phase evolution of doped HfO2 or HfO2-ZrO2 thin films also depends on other factors, such as electric field cycling. Similar to any other ferroelectric material, 62-65 fluorite-structured ferroelectrics exhibit a change in ferroelectric response during the endurance test, whereby the changes in remanent polarization (P_r) and coercive field (E_c) are measured during the repetitive electric field cycling. In the initial stage of the endurance test, the P_r of fluorite-structured ferroelectrics generally increases, which is known as the wake-up effect, 66 and decreases at the late stage of the endurance test, which is referred to as fatigue. Although there are still some debates on which factors would dominate the true origin of the change in the endurance test of fluorite-structured ferroelectrics, numerous studies have suggested that the phase evolution as well as domain depinning play important roles in understanding the endurance test results. Zhou et al. 66 first examined the origin of the wake-up effect and suggested that the depinning of pinned domains in the pristine state during repetitive field cycling would be the origin of the wake-up effect. Kim et al.⁶⁸ and Pesic et al. 75 reported that the wake-up effect observed in Hf_{0.5}Zr_{0.5}O₂ and Sr-doped HfO2 thin films, respectively, could be caused by the dynamic phase evolution, wherein phase transitions occur from the tetragonal to orthorhombic phase at the interface regions or from the monoclinic to orthorhombic phase in the bulk region during electric field cycling.

In this section, the polymorphism in fluorite-structured ferroelectrics with respect to various factors was reviewed based on the existing literature. Although only centrosymmetric phases are observed in the classical phase diagram of bulk HfO2, ZrO2, and their solid solutions, ferroelectricity can be realized in doped HfO2 or HfO2-ZrO2 thin films fabricated via various deposition techniques. The spatial inhomogeneities of various driving factors, such as volumetric confinement, dopant concentration, strain, and defect concentration, are believed to contribute to the nanoscale competition among various crystalline phases in fluorite-structured ferroelectrics, thereby generating a polar orthorhombic phase (Pca2₁) under optimum conditions. Moreover, the wake-up effect generally observed during the endurance test of the fluorite-structured ferroelectrics is probably attributable to the dynamic phase evolution arising from the redistribution of charged defects, such as oxygen vacancies, as well as the depinning of pinned domains. Both the polymorphism arising from the competition between crystalline phases and dynamic phase evolution caused by an external electric field are expected to affect the domain dynamics and

polarization switching kinetics in fluorite-structured ferroelectrics; these will be discussed later in detail.

B. Crystallographic hierarchy and polarization switching pathways in fluorite-structured ferroelectrics

The discovery of ferroelectricity in fluorite-structured ferroelectrics was followed by numerous theoretical studies 15,46,76-80 to elucidate the crystallographic origin and pathways to the formation of the polar phase allowing for ferroelectricity. In 2014, based on the density functional theory (DFT) calculations, Huan et al. 15 studied the possible polar phases that can emerge from higher-symmetry, nonpolar parent phases by combining the minima-hopping method⁸¹ and group theoretical symmetry reduction principles. They presented possible pathways toward the achievement of both polar and nonpolar phases of HfO₂, as shown in Fig. 3(a). For low-symmetry, nonpolar phases, the symmetry-reducing pathway starts from the highest symmetry cubic phase and is consistent with the phase diagram of HfO2 and ZrO2; the highest symmetry cubic phase appears at the highest temperatures, whereas the lower symmetry monoclinic phase appears at 298 K.^{33,3} Huan et al. also showed that the orthorhombic and monoclinic phases of HfO2 can diverge from the intermediate tetragonal phase when the symmetry of the various polymorphs of HfO2 and ZrO2 are considered. This observation is also in agreement with the report by Boescke et al. 10 whereby the metastable orthorhombic and stable monoclinic phases could deviate from the starting tetragonal phase on the basis of the presence/absence of the capping layer.

Barabash et al. 77,82 also studied the relationship among various crystalline phases of HfO2 using DFT calculations. They assumed that all the lattices of the crystalline phases of HfO2, except the orthorhombic-II phase (Pnma), could be considered as slightly distorted cubic lattices (also known as pseudo-cubic structure), including the orthorhombic Pbcm phase, which had been suggested to exist under high pressure conditions in both HfO₂ and ZrO₂. 83,84 Building upon this approach, they considered that half of the oxygen ions occupied the perfect tetrahedral interstitial sites in fluorite structures within the same plane, while the other half of the oxygen ions occupied one of the two possible off-perfect sites with a 50% probability. They suggested that by displacing four oxygen ions to every other $\pm x$ and $\pm y$ direction in the plane normal to the b-axis, while ensuring that the remaining four oxygen ions did not move in the other set of the plane from the "parent" Pbcm lattice, the orthorhombic Pbcm phase could be transformed into other phases, such as monoclinic (P21/c), orthorhombic-I (Pbca), and polar orthorhombic (Pca21), as well as other potential low-energy phases (hypothetical structures, X1, X2, and X3 structure). Nonetheless, two well-known phases, cubic $(Fm\overline{3}m)$ and tetragonal $(P4_2/nmc)$, remain as exceptions in this case because oxygen ions do not move in the cubic phase and are displaced in a single direction for the tetragonal phase. The resulting hierarchy of structures is shown in Fig. 3(b).

In addition to the studies on the phase stability of different HfO_2 phases, there have been several works on the switching pathways for different polarization states of the polar orthorhombic phase $(Pca2_1)$. ^{15,76,77,85} As shown in Figs. 1(d) and 1(e), the two polarization states (up and down) of the polar phase differ in the polarization direction by 180° ; thus, they are topologically equivalent phases. Clima et al. ⁷⁶ first reported that the polar phase of HfO_2 could be switched

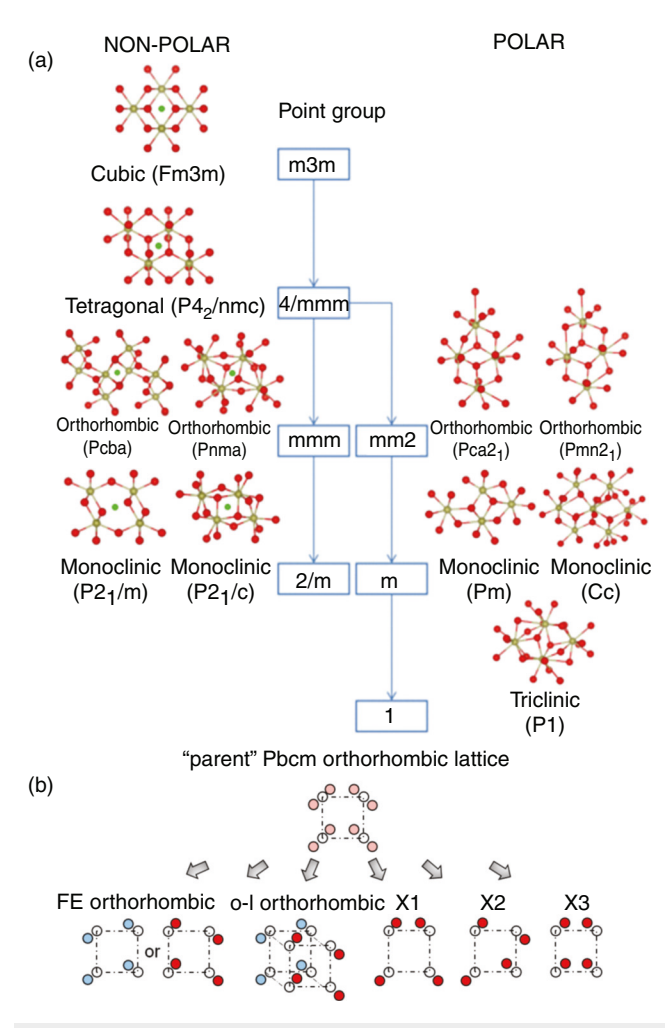


FIG. 3. (a) Flow chart of low energy phases of HfO₂ with respect to the symmetry reduction principle. (b) Possible pathways of known and hypothetical phases diverged from the "parent" *Pbcm* lattice. Note the planes are projected normal to the b-axis from the "parent" *Pbcm* lattice. Reproduced with permission from (a) Huan *et al.*, Phys. Rev. B **90**(6), 064111 (2014). ¹⁵ Copyright 2014, American Physical Society; and (b) Barabash *et al.*, ECS Transactions **75**(32), 107–121 (2017). ⁷⁷ Copyright 2017, The Electrochemical Society.

by moving four threefold-coordinated oxygen ions [oxygen ions are colored as yellow in Figs. 1(d) and 1(e)] upward or downward along the polar axis (here, c-axis) of the unit cell. Based on the nudged elastic band (NEB) approach, they obtained a double-well-shaped potential energy curve as a function of the polarization in the polar phase of HfO₂, as shown in Fig. 4(a). The double-well potential shows that the energy barrier of polarization reversal (\sim 100 meV/f.u.) can be fitted to a fourth-order polynomial, which is consistent with the Landau–Ginzburg formalism⁸⁶ for the second-order phase transition.

While Clima et $al.^{76}$ considered the up and down switching behavior without considering the intermediate metastable phase, Huan et $al.^{15}$ modeled an intermediate phase existing when the polarization of the polar orthorhombic phase $(Pca2_1)$ switched between the up and down states. They proposed that the tetragonal phase may

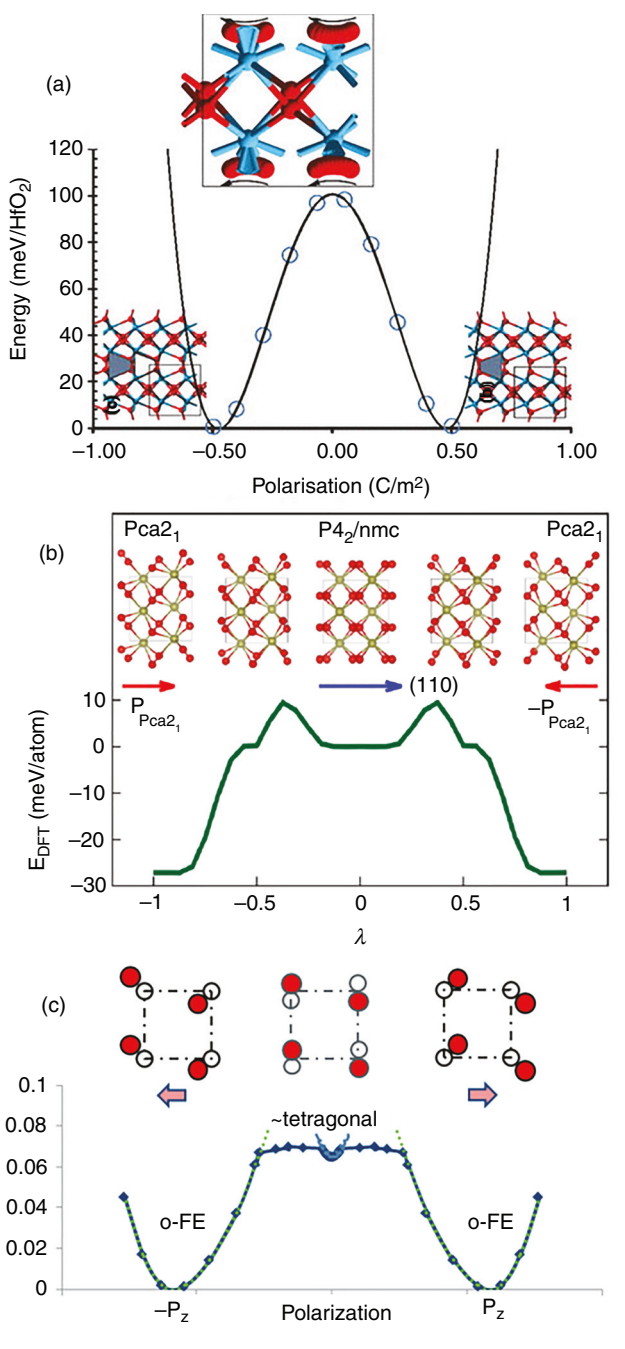


FIG. 4. Minimum energy pathways between the up and down states of the polar phase ($Pca2_1$) from various works: (a) Clima *et al.*⁷⁶ where the blue and red spheres indicate the Hf and O atoms, respectively; (b) Huan *et al.*¹⁵ where the yellow and red spheres indicate the Hf and O atoms, respectively; and (c) Barabash *et al.*⁷⁷ where O atoms are indicated by the red spheres and metal atoms are omitted for convenience. Note the atomic structure is shown along the "in-plane" in Fig. 4(c). Reproduced from (a) Clima *et al.*, Appl. Phys. Lett. **104**(9), 092906 (2014)⁷⁶ with permission of AIP Publishing. Reproduced with permission from (b) Huan *et al.*, Phys. Rev. B **90**(6), 064111 (2014). ¹⁵ Copyright 2014, American Physical Society; and (c) Barabash *et al.*, ECS Transactions **75**(32), 107–121 (2017). ⁷⁷ Copyright 2017, The Electrochemical Society.

serve as the intermediate phase based on the results depicted in Fig. 3(a). It should be noted that the [001] direction (polar axis) of the polar orthorhombic phase (Pca2₁) corresponds to the [110] direction of the tetragonal phase. By setting the tetragonal phase as the reference and modeling ferroelectric domains with two opposite polarization vectors on either side, as depicted in Fig. 4(b), they observed three local polarization minima (up, zero, and down) in the energy pathway curves. The energy barrier required to make a transition between the up and down states of the polar phase is \sim 120 meV/f.u. (\sim 40 meV/ atom), whereas the energy barrier required to transform the intermediate phase (tetragonal) to either the up or down state of the polar orthorhombic phase ($Pca2_1$) is $\sim 30 \text{ meV/f.u.}$ ($\sim 10 \text{ meV/atom}$). This finding suggests that the transition between the up and down polarization states of the polar orthorhombic phase (Pca2₁) (180° polarization switching) may be facilitated by an excursion through the tetragonal phase in response to suitable combinations of stress and/or internal/ external electric fields.

Barabash et al. 77 also studied the switching pathway of the polar orthorhombic phase of HfO2 and ZrO2. Based on the Pbcm "parent" lattice approach discussed above, they assumed that the transition between the up and down states of the polar orthorhombic phase (Pca2₁) may be accompanied by the structural transformation between the polar orthorhombic phase (Pca2₁) and the Pbcm lattice. Although the energetically preferred pathway does not connect the two states (up and down) from the same "parent" Pbcm lattice, both states belong to different "parent" Pbcm lattices, wherein the oxygen ions within the same plane are displaced in different directions. It should be noted that the two "parent" Pbcm lattices differ from the small outof-plane displacements of the oxygen ions; hence, these out-of-plane distortions fully disappear in the intermediate tetragonal-like lattice. They concluded that the switching pathway between the two states of the polar orthorhombic phase (Pca21) did not connect directly and should include the intermediate state of the tetragonal-like structure. Polarization switching occurs for both HfO2 and ZrO2 with a high switching energy barrier of 94 meV/f.u. and 70 meV/f.u., as well as a low switching energy barrier of ~4 meV/f.u. and ~5 meV/f.u., respectively. The resulting switching pathway is depicted in Fig. 4(c).

A comparative study of the possible intermediate phases during the polarization switching between the up and down states of the polar orthorhombic phase (Pca2₁) was also performed by Maeda et al.⁸¹ They reported that two intermediate states seemed the most reasonable, as those states were found in the two lowest energy pathways in their study: (1) orthorhombic phase (*Pbcm*) and (2) tetragonal phase (P42/nmc). They observed an approximately two times higher energy barrier for the switching pathway that involved the orthorhombic phase (Pbcm) at zero polarization (~200 meV/f.u.) than that for the tetragonal phase (P42/nmc) at zero polarization (~75 meV/f.u.). Therefore, the pathway that involves the tetragonal phase $(P4_2/nmc)$ can be considered as the most feasible pathway for polarization switching in the polar orthorhombic phase (Pca2₁) of HfO₂, which is consistent with the previous works by Huan et al. 15 and Barabash et al. 77 Moreover, this observation is consistent with the experimental work conducted by Park and Kim,⁸⁷ wherein two-step polarization switching can be observed in Hf_{0.4}Zr_{0.6}O₂ thin films with the involvement of the intermediate tetragonal phase at zero polarization. Although the experimental observation was for Hf_{0.4}Zr_{0.6}O₂ thin films at a morphotropic phase boundary between the orthorhombic and tetragonal

phases, this observation could be considered as evidence for the tetragonal-phase-induced switching path in fluorite-structured ferroelectrics. 87,88 It should be noted that the two-step polarization switching does not serve as definitive evidence for the existence of an intermediate phase, because polarization switching can be mediated by an intermediate ferroelastic state of the same polymorph, as previously demonstrated. 89,90 When the concentration-dependent changes in the polarization switching processes are carefully examined, the intermediate phase observed in the $\mathrm{Hf}_{0.4}\mathrm{Zr}_{0.6}\mathrm{O}_2$ phase would be the tetragonal phase. 87

In this section, the crystallographic hierarchy and pathway for switching between two polarization states of the polar orthorhombic phase $(Pca2_1)$ are elucidated. From the independent computational and theoretical works discussed, it can be concluded that the pathway involving an intermediate tetragonal phase with zero polarization would be preferable. However, it should be noted that the energy barrier cannot be directly correlated with the energy needed for real polarization switching in materials because switching occurs in a continuous lattice and involves the nucleation and growth of domain walls. This practical switching process governed by the nucleation and growth of inversely polarized domains should be distinguished from the intrinsic switching modeled in the aforementioned computational simulations.

C. Domains in fluorite-structured ferroelectrics

A domain is a spatial region in a crystal or grain wherein the direction of spontaneous polarization is continuous across a finite region of the material. The boundaries between different domains are called domain walls. Based on the configuration of the polarization directions near the domain walls, in a simplistic approach, two types of domain walls can be considered for the polar orthorhombic phase (Pca2₁) in fluorite-structured ferroelectrics: 180° and 90°. It should be noted that the domain wall types in the ferroelectric rhombohedral phase of epitaxial fluorite-structured thin films can be different, and the focus of this paper is on the polar orthorhombic phase $(Pca2_1)$. On the one hand, the 180° domain walls are formed when the polarization direction between two neighboring domains is opposite. On the other hand, the 90° domain walls are formed when the polarization direction between two neighboring domains is perpendicular. Notably, the 90° domain walls are more complex because their motion is accompanied by not only the ferroelectric transition between different directions of spontaneous polarization of the polar phase but also the ferroelastic distortions. Because the first publication of ferroelectricity in fluorite-structured ferroelectrics has been just a decade ago, only a limited number of theoretical works or experimental observations in the ferroelastic nature of the domain walls have been reported. Therefore, in this study, the 180° and 90° domain walls and their motions are mostly referred to as the ferroelectric transition between the up and down states of the polar phase, unless stated otherwise.

Ding et al. 91 studied possible types of domains and domain walls in the polar orthorhombic phase (Pca2₁) using DFT calculations with the NEB approach. Because the polar phase of HfO₂ (Pca2₁) consists of an orthorhombic structure, whereby the lattice constants of the three orthogonal axes are all different, it is possible to make six different variants regardless of the polarization direction. Therefore, three types of 180° and three types of polarization twisting 90°, as well as four types of polarization tilting 90° domain walls could be

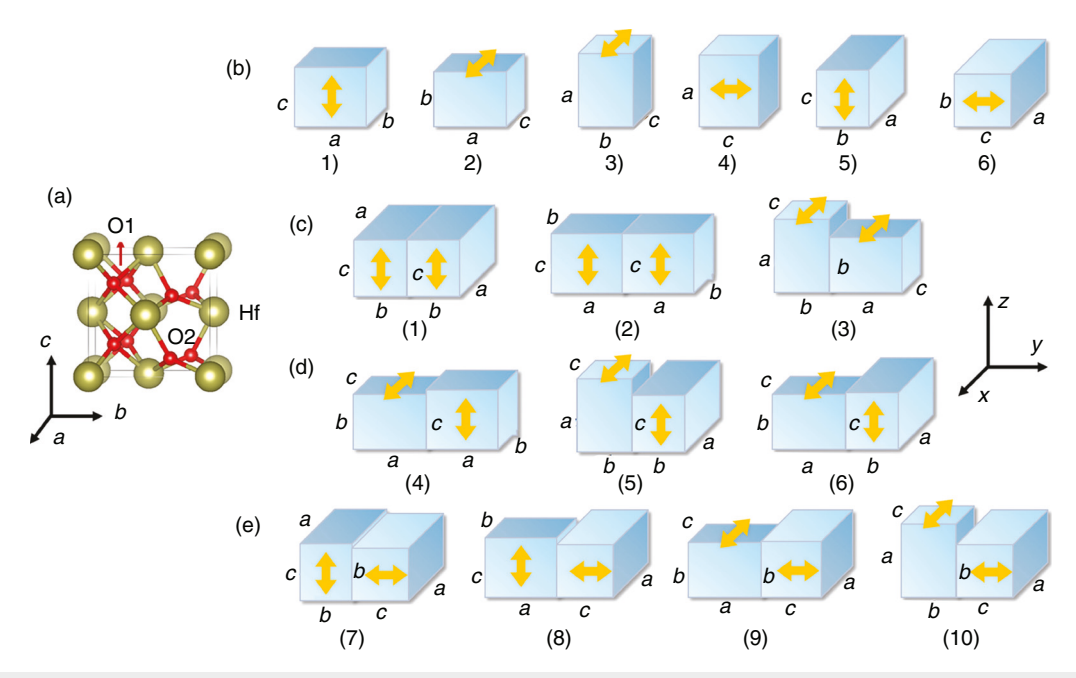


FIG. 5. (a) Atomic structure of the polar orthorhombic phase (*Pca2*₁) of HfO₂. Note that the dark yellow and red spheres represent the Hf and O atom, respectively. (b) Six orthorhombic variants. (c) Three types of 180° domain walls. (d) Three types of twisting 90° domain walls. (e) Four types of tilting 90° domain walls. Reproduced with permission from Ding *et al.*, Acta Materialia **196**, 556–564 (2020). Copyright 2020, Elsevier Ltd.

constructed, making a total of 10 types of nonequivalent domain walls, as shown in Fig. 5. The detailed calculation results of the 10 types of domain walls are summarized in Table I. From their calculations, types (1), (4), and (7) are the most probable domain walls for 180°, polarization twisting 90°, and polarization tilting 90°, respectively, because they show the lowest domain wall energy in each group. Furthermore, the thickness of most domain walls would be low (less than two unit cells) based on the small lattice mismatch observed for most domain walls. Notably, they observed negative domain wall energy in the type (1) domain wall, which was, in principle, impossible. After carefully observing the type (1) domain wall, they found that the

crystallographic structure at the domain wall [boundary between two states of the polar orthorhombic phase ($Pca2_1$)] was very similar to the atomic structure of the Pbca orthorhombic phase. In particular, Materlik $et\ al.^{14}$ reported that the crystallographic structure of the Pbca orthorhombic phase [Fig. 1(f)] appeared to be an antiferroelectric phase wherein the two dipoles were arranged in an antiparallel configuration within the unit cell. The negative domain wall energy ($-18\ mJ/m^2$) found in the type (1) domain wall can be attributed to the formation of a local Pbca orthorhombic phase at the domain wall. Notably, the free energy of the Pbca orthorhombic phase is lower than that of the polar orthorhombic phase ($Pca2_1$) over a wide temperature

TABLE I. Summary of 10 types of domain walls in ferroelectric HfO₂. Reproduced with permission from Ding *et al.*, Acta Materialia **196**, 556–564 (2020). Copyright 2020, Elsevier Ltd.

Domain wall category	Domain	Mismatching		Domain wall	Mignation	I ammont awas	
	wall type	Along x	Along z	energy (mJ/m ²)	Migration barrier (eV)	Longest axes relation	Ref. 94
180°	1	0	0	-21.3	0.93	Parallel	Undistinguishable
	2	0	0	218.5	0.50		
	3	0	4.15%	610.0	0.34	Tilt	Found
90° (P twist)	4	0.53%	0.53%	233.7	0.19	Parallel	Not found
	5	3.56%	3.56%	473.2	0.45	Twist	Found
	6	3.56%	0.53%	422.4	0.51	Tilt	Found
90° (P tilt)	7	0	0.53%	435.5	0.07	Parallel	Found
	8	4.15%	0.53%	874.7	0.23	Tilt	Not found
	9	3.56%	0	887.6	0.14	Tilt	Found
	10	3.56%	4.15%	655.9	0.49	Twist	Found

range.¹⁴ Thus, it is reasonable to believe that the formation of the local Pbca orthorhombic phase at the domain wall can be the origin of the negative domain wall energy. Recent theoretical findings in the negative domain wall energy of ferroelectric HfO2 also support the possibility of the formation of a local *Pbca* orthorhombic phase at the domain wall. 22 Regarding the smallest (or even negative) domain wall energy found in the type (1) domain wall, Ding et al. concluded that the type (1) domain wall could be easily formed in HfO2-based ferroelectrics and was expected to be the microscopic mechanism for the 180° polarization switching under an external electric field. It should be noted that the formation of the local Pbca orthorhombic phase at domain walls and the negative domain wall energy is unexpected and cannot be understood from the viewpoint of the thermodynamics of ferroelectrics. Additionally, they reported that the large E_c of the HfO₂-based ferroelectrics could be caused by the large domain wall migration barrier (0.93 eV) observed from the type (1) domain wall. A recent theoretical study by Lee et al. 92 also reports that the domain walls in HfO2 are surprisingly thin and domain walls will not be efficiently propagated, although they can only move by hopping over a large energy barrier, which is consistent with the results of Ding et al. Furthermore, Lee et al. 92 proposed that the ferroelectric order could theoretically exist in HfO2 films with nanometer-scale thickness, which will have a significant impact on both the scientific and industrial communities. The experimental observations of domains in HfO₂-based films using various characterization techniques are now discussed.

The existence of domains can be revealed using various characterization techniques. There are two main ways to characterize domains in ferroelectric materials: (1) static and (2) dynamic measurements. Here, static measurements include structural characterizations, such as transmission electron microscopy (TEM) and x-ray diffraction (XRD) analysis, whereby the time-independent characteristics of domains (e.g., domain size, boundaries, and orientations) can be measured. Dynamic measurements include electrical characterizations, such as P-E hysteresis measurement and piezoresponse force microscopy (PFM), whereby the time-dependent characteristics of domains (e.g., switching time, nucleation time, and coercive field) can be measured as a function of time and voltage. Notably, some advanced static measurement techniques, such as in situ TEM or in situ XRD, may enable the acquisition of both time-dependent and time-independent characteristics of domains in ferroelectric materials; however, they are not common experiments as they additionally require special equipment.

One of the most effective techniques to directly visualize domains is TEM. Figure 6(a) shows a dark-field TEM image of Gd-doped HfO₂ thin films. The grains in Gd-doped HfO₂ films typically have a lateral dimension of 20–30 nm and a vertical dimension of 20 nm, which is consistent with other reports in HfO₂-based thin films. ^{44,47,93} Grimley *et al.* ⁴⁷ showed the grain size, atomic structure, and interphase boundary of polycrystalline Gd-doped HfO₂ films determined through high-angle annular dark-field (HAADF) scanning transmission electron microscopy [STEM; Fig. 6(b)]. The magnified view of the orthorhombic phase region shown as d in Fig. 6(b) could be further separated by a sharp domain wall [pointed with the white arrow in Fig. 6(d)] into two domains that were determined by inspecting the atomically resolved positions of the projected Hf atom sublattice. The distance map for each atom shown in Fig. 6(e) emphasizes the existence of a domain wall between the O1 and O2 regions (orthorhombic phase

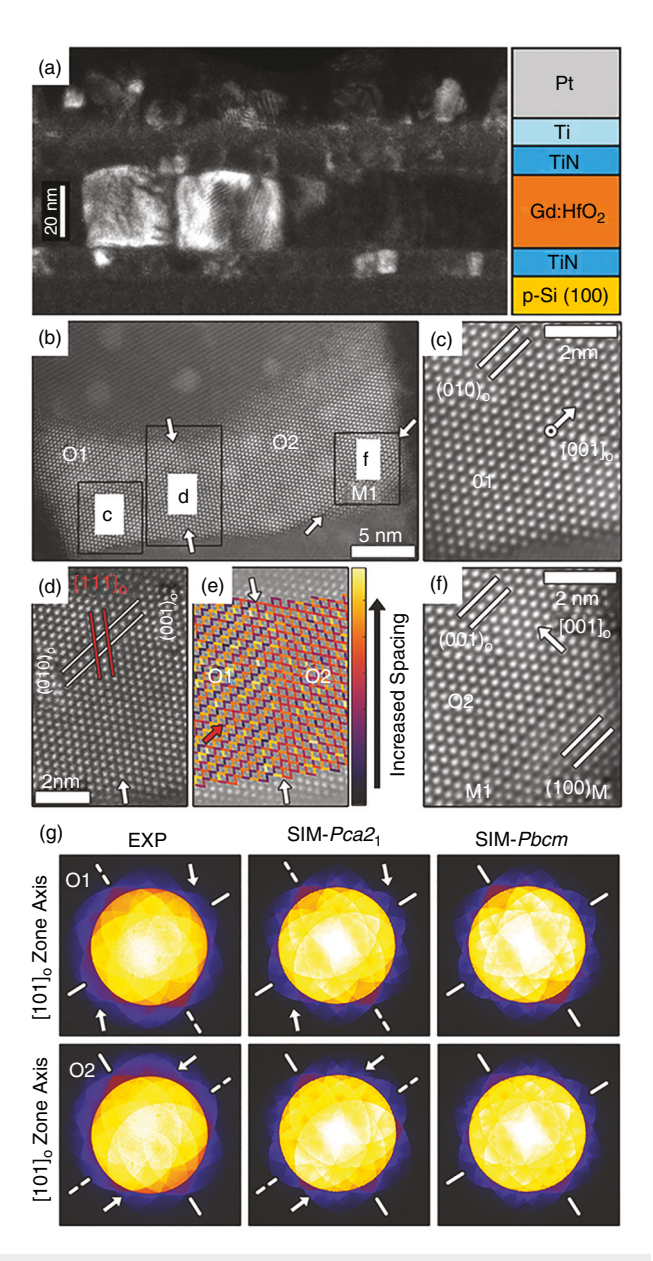


FIG. 6. (a) DF TEM image of polycrystalline Gd-doped HfO2 and (b) its HAADF-STEM image with orthorhombic (O) and monoclinic (M) regions separated by boundaries indicated by white arrows. (c) and (f) magnified regions from (b) where the planes and the polar directions are indicated by lines and white arrows, respectively. (d) Magnified region from (b) where O1/O2 boundary exists and (e) distance map for each atom column shown in (d) where colored lines emphasize changes in the projected symmetry (red arrow provides a visual guide). (g) PACBED patterns observed from O1 and O2 regions (EXP) and simulated PACBED patterns of the Pca2₁ and Pbcm phase. The presence and lack of a mirror plane are shown as solid and dashed lines. The white arrows shown in the O1 and O2 patterns highlight symmetry breaking in the patterns. The 90° rotated arrows of the O1 and O2 patterns indicate the presence of the 90° domain wall between the O1 and O2 regions. Reproduced from (a) Hoffmann et al., J. Appl. Phys. 118(7), 072006 (2015), 26 with permission of AIP Publishing. Reproduced with permission from (b-g) Grimley et al., Adv. Mater. Interfaces 5(5), 1701258 (2018). 47 Copyright 2018, John Wiley and Sons.

regions with different orientations). The change in symmetry can be comprehensively evaluated via position-averaged convergent beam electron diffraction (PACBED) analysis, whereby missing symmetry in the pattern indicates a lack of inversion symmetry in the material. The lack of inversion symmetry occurs for the Pca2₁ phase along the [001]_O direction, and it can be found from multiple areas in the sample, as indicated by the white arrows in Figs. 6(c) and 6(f). The type of domain walls can be further identified by examining the change in symmetry. For example, the experimentally observed PACBED patterns of both the O1 and O2 regions seem to match well with the simulated PACBED patterns of the Pca21 phase shown in Fig. 6(f). The 90° rotated symmetry breaking and mirror plane in the O1 and O2 PACBED patterns (indicated by white arrows and solid lines in the pattern, respectively) indicates that the O1 and O2 regions are rotated by 90°. These results show that the domain wall found in this region is a 90° domain wall.

Various types of domain walls are more easily found when the sample is epitaxially grown. Kiguchi *et al.*⁹⁴ studied the domain structures in epitaxially grown 7 mol. %-Y-doped HfO₂ (YHO-7) deposited on (100)-oriented yttria stabilized zirconia (YSZ). They first obtained the atomic structure of Hf in YHO-7/YSZ (100) epitaxial thin films from HAADF-STEM images [Figs. 7(a)-7(c)] and compared them with the simulated atomic structures of Hf in the polar phase [Figs. 7(a)'-7(c)'] projected from different orthogonal directions. It is noteworthy that Hf was used to construct atomic structures because O would not be shown in the HAADF-STEM images owing to its lower Z-contrast (relative to Hf). Knowing that the YHO-7 films are epitaxial and the atomic structures in all three orthogonal directions are given,

various types of domain walls are identified from the HAADF-STEM images shown in Figs. 7(d) and 7(e). It should be noted that the types of domain walls found in this study are also recorded in Table I. Furthermore, domains and domain boundaries could also be defined using geometrical phase analysis (GPA) based on high-resolution transmission electron microscopy (HRTEM) images. To be specific, the GPA enables the conversion of the HRTEM image into a strain map by differentiating the displacement field, which results from analyzing the change in phase of the intensity of the Fourier series of the HRTEM image. The strains are approximately zero within the domains but reasonably higher along the boundaries; thus, domain walls/boundaries can be mapped by superimposition on the HRTEM image. The resulting domain map of the polycrystalline 4.2% Si-doped HfO₂ thin film with an average domain size of a few nanometers is shown in Fig. 7(f).

Another TEM-based technique to analyze the spatial distribution of the crystallographic phases and orientations is the so-called transmission electron backscatter diffraction (EBSD) or low energy transmission Kikuchi diffraction (LETKD). It was demonstrated by Keller and Geiss that the LETKD could analyze the spatial distribution of crystallographic phase and orientation in nanoscale thin films. Lederer $et\ al.$ conducted LETKD on the polycrystalline $Hf_{0.5}Zr_{0.5}O_2$ thin films, and reported that the polar c_o -axis is dominantly in-plane oriented, suggesting that the in-plane polar axis would be the origin of small P_r value of $Hf_{0.5}Zr_{0.5}O_2$ films before wake-up. Lederer $et\ al.$ also showed that LETKD could be applied to quantitatively analyze the spatial distribution of crystallographic phases and orientations in the ferroelectric gate oxide in the integrated FeFETs. 98 The advantage

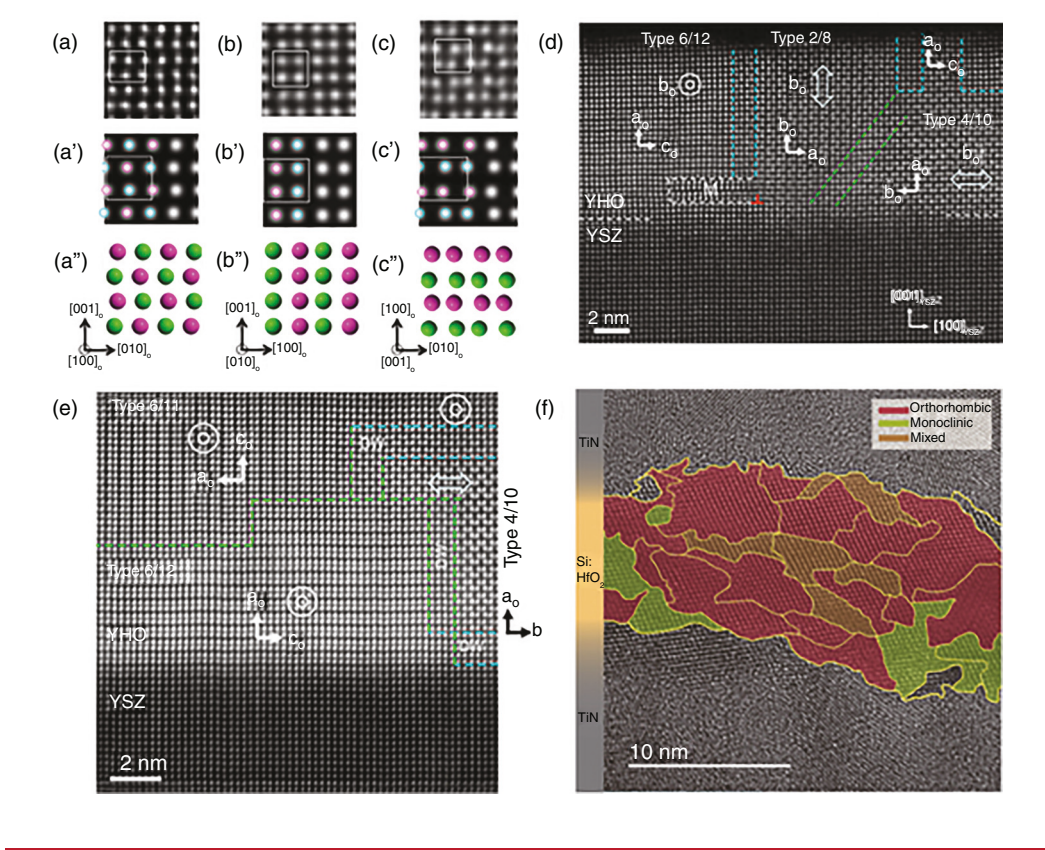


FIG. 7. (a-c) Hf atomic columns experimentally observed from the HAADF-STEM images of YHO/YSZ (100) epitaxial thin film. (a'-c') Hf atomic columns acquired from the multislice simulation. (a"-c") Structure model of Hf in the polar phase of HfO2 (Pca21). Note all images were projected along [100]_O, [010]_O, and [001]_O directions. Open circles in (a'-c') correspond to the same colored Hf atoms in (a"-c") and open squares show unit cells. (d-e) Various types of domain walls observed from HAADF-STEM images. (f) Phase and domain distribution of polycrystalline 4.2% Si: HfO2. Note the yellow lines indicate domain boundaries. Reproduced with permission from (a-e) Kiguchi et al., Jpn. J. Appl. Phys. 57(11S) (2018). Copyright 2018, The Japan Society of Applied Physics; and (f) Lee et al., ACS Appl. Mater. Interfaces 11(3), 3142-3149 Copyright 2019, American Chemical Society.

of using the LETKD is that the spatial distribution of crystallographic phases and orientations can be statistically analyzed for a rather wide area compared to the previously discussed TEM work.

While the domains and domain walls in the local area of the ferroelectric HfO2 thin films are directly observed via TEM, XRD is also used to study the orientation of domains on average in ferroelectric HfO₂ thin films. Katayama et al. 99 reported that, according to the types of substrate used in the experiment, the polar orthorhombic (Pca2₁) YHO-7 films can exhibit preferred out-of-plane orientation along different axes during deposition. In other words, the polar orthorhombic (Pca2₁) YHO-7 films can be textured uniaxially along the out-of-plane direction. The in-plane XRD patterns (θ -2 θ coupled geometry) of the YHO-7 films grown on (001) YSZ and (001) ITO//(001) YSZ substrates scanned along $\Phi = 45^{\circ}$ are shown in Figs. 8(a) and 8(b), respectively, where angle Φ represents the rotational axis along the out-of-plane direction. The sharp reflection peak of YHO-7 110 in Fig. 8(a) indicates that the polar orthorhombic (Pca2₁) domains exhibit preferred out-of-plane orientation along the bo- (nonpolar) or c_o-axis (polar). Conversely, the absence of the reflection peak of YHO-7 110 in Fig. 8(b) indicates that the polar orthorhombic (Pca2₁) domains exhibit preferred out-of-plane orientation along the ao-axis (nonpolar). This work demonstrates the ability to control the orientation of the polar orthorhombic (Pca21) domains in YHO-7 and provides a deep analysis to identify the domain structures using XRD.

Shimizu et al.¹⁰⁰ used synchrotron micro-beam x rays on two selected electrodes, where one was placed in the pristine region and the other was in the poled region. The resultant XRD patterns

measured for the pristine and poled regions are plotted as red and black lines, respectively, as shown in Figs. 8(c) and 8(d). It is worth noting that the integrated area under the ITO 0012 reflection peak of the pristine and poled patterns (as well as the area under the ITO $00\overline{10}$ reflection peak) seem to be similar, which indicates that the interaction volume of x ray and the sample would be similar for both regions. Therefore, comparing the intensity change in certain reflection peaks of the HfO₂ phase between two regions (pristine and poled) may elucidate the domain reorientation behavior in HfO2 under the application of an external field. The appearance of YHO-7 060/006 reflection peaks for the poled XRD pattern in Fig. 8(c) implies that the volume fraction of either the b₀-axis (nonpolar)- or c₀-axis (polar)-oriented domains increases as the sample is poled. Similarly, the disappearance of the YHO-7 050 reflection peak for the poled XRD pattern in Fig. 8(d) indicates that the volume fraction of the b₀-axis (nonpolar)oriented domain decreases as the sample is poled. Through these measurements, it is shown that ferroelectric/ferroelastic domain reorientation occurs as the sample is poled, particularly from the bo-axis (nonpolar)- to the c_o-axis (polar)-oriented domains. In other words, the electric field induces domain reorientation from the b_o-axis (nonpolar)-oriented domains to the c_o-axis (polar)-oriented domains. Because the XRD patterns of the poled region were acquired under static conditions where no electric field was applied during the XRD measurement, the increase in the volume fraction of the co-axis (polar)-oriented domains seemed to remain the same after the removal of the electric field. They concluded that this domain reorientation was an irreversible process that could be referred to as

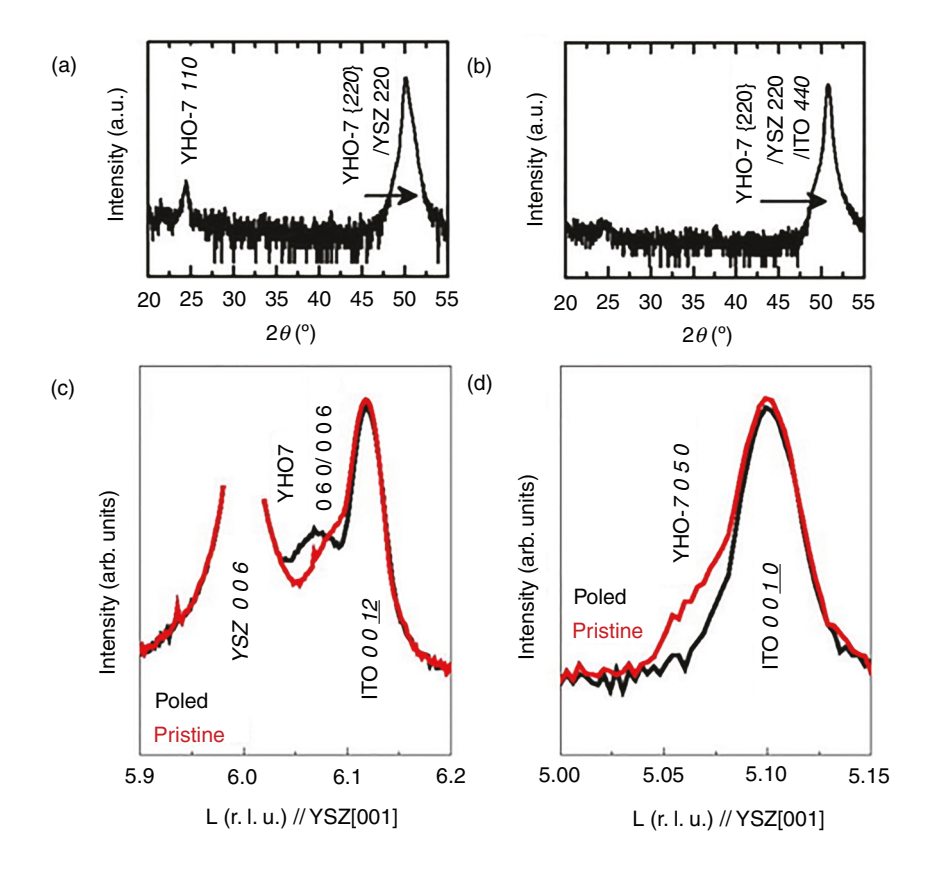


FIG. 8. In-plane XRD patterns (θ –2 θ coupled geometry) of epitaxial YHO-7 films grown on (a) (001) YSZ and (b) (001) ITO//(001) YSZ substrates scanned along $\Phi = 0^{\circ}.$ XRD patterns of pristine and poled YHO-7//(001) ITO//(001) YSZ scanned along the L-axis [(c): 5.90-6.20 and (d): 5.00-5.15] in reciprocal space where L-axis is parallel to the YSZ [001] direction. Note that the red and black lines indicate the XRD patterns of the pristine poled regions, respectively. Reproduced from (a-b) Katayama et al., J. Appl. Phys. 119(13), 134101 (2016); and (c-d) Shimizu et al., Appl. Phys. Lett. **113**(21) (2018)¹⁰⁰ with permission of AIP Publishina

ferroelastic domain reorientation. Hence, once ferroelastic (non-180°) domain reorientation occurs, the subsequent polarization switching behaves as the 180° domain switching. The increase in the volume fraction of the c_o -axis (polar)-oriented domains was also confirmed by comparing domain fractions from their HAADF-STEM images of pristine and poled samples (not shown here).

In addition to the static measurements, dynamic measurements, such as PFM, were conducted to confirm the existence of domains in ferroelectric HfO₂. ^{101–103} Buragohain *et al.* ¹⁰² studied domain structures and domain dynamics in La-doped HfO₂ via PFM. The surface topography image acquired by means of atomic force microscopy (AFM), as presented in Fig. 9(a), shows that the root mean square surface roughness of the sample is sufficiently low to be consistent with

nanoscale grains. For the same area, the phase and amplitude images shown in Figs. 9(b) and 9(c), respectively, were acquired via PFM. The comparison between the surface topography [Fig. 9(a)] and phase images [Fig. 9(b)] indicates that the La-doped HfO₂ film consists of polydomains with an average domain size of several hundred nanometers. It should be noted that the resolution limit of the PFM image is approximately 500 nm, 104 which is 25 times (or more) higher than the measured domain size (~20 nm) in the STEM by Grimley *et al.* 47 Accordingly, the precise domain size might not be resolved in the PFM study. However, the spatial variations in the domain configurations and switching kinetics in domains can be investigated by examining the change in PFM images as a function of pulse duration time. Figure 9(d) shows the PFM images of the instantaneous domain

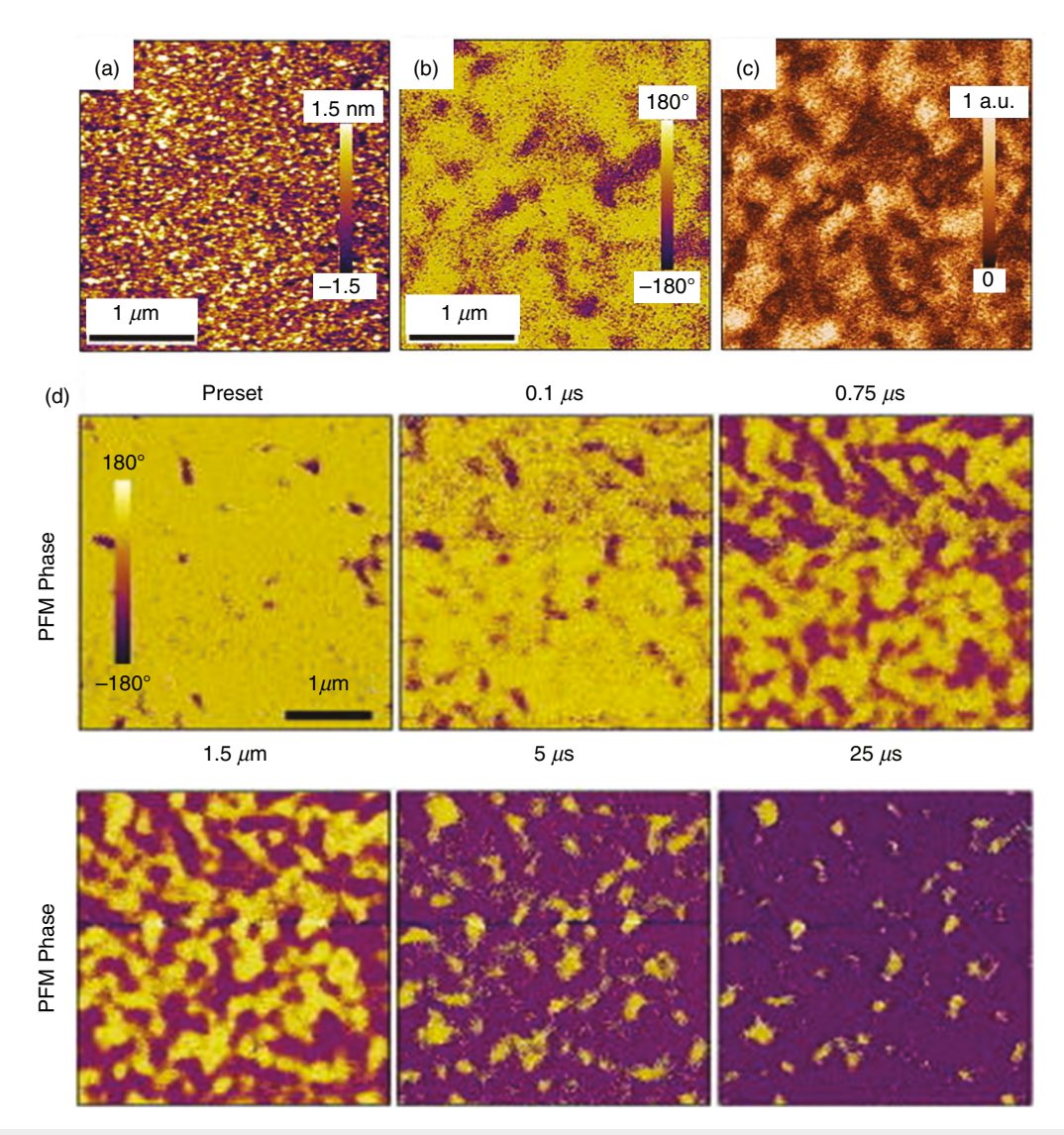


FIG. 9. (a) Surface topography image acquired via AFM and (b) phase and (c) amplitude image acquired via PFM for La-doped HfO₂. (d) PFM phase image of instantaneous domain configurations developing at different stages of polarization reversal under the application of 4.0 V pulses of increasing duration. Reproduced from Buragohain *et al.*, Appl. Phys. Lett. **112**(22), 222901 (2018)¹⁰² with permission of AIP Publishing.

configurations at different duration times of $4.0 \,\mathrm{V}$ switching pulse acquired from the La-doped HfO₂ film. It can be seen that domains start to grow from the initial islands where the polarity is already aligned along the same direction of the applied bias. The initial islands represent: (1) pinned domains that had not been removed during the wake-up process or (2) domains that were not switched during the application of bias. It should be noted that the domains do not fully grow to the same phase even at a pulse time of $25 \,\mu\mathrm{s}$. Therefore, it can be concluded that the domain dynamics in La-doped HfO₂ films may follow the nucleation-limited switching (NLS) model, which will be discussed in more detail in Sec. III.

In this section, previous theoretical and experimental studies on domains in fluorite-structured ferroelectrics are comprehensively reviewed. From the theoretical works, it was suggested that the zerowidth domain walls would be made by forming a Pbca metastable phase at the exact interface between two neighboring domains where the polarization directions are opposite to 180°. This is possible because the bulk free energy of the Pbca orthorhombic phase is lower than that of the polar orthorhombic phase (Pca2₁) at a wide range of temperatures owing to the negligible entropy difference between the two orthorhombic phases. Moreover, it has been suggested that the domain wall energy in the polar orthorhombic phase (Pca21) can be negative, which seems contradictory to the classical understanding of domain walls in ferroelectrics. From the experimental works, it was identified that grains of 20-30 nm are the basis of the polycrystalline HfO₂-based films.²⁶ Since the domain size was determined to be smaller than 10 nm, only a few domains would exist within one grain. Both the 90° and 180° domain walls could be directly imaged using STEM techniques, 47,94,95 and the minute differences in the XRD patterns in the epitaxial ferroelectric YHO-7 films could elucidate the types of domains and domain switching in HfO2. 99,100 Furthermore, the spatial distribution of the substrate-normal polarization could be visualized using state-of-the-art PFM techniques at a larger scale. 102 As previously mentioned, however, merely a limited number of works on domains in fluorite-structured ferroelectrics have been reported to date; thus, further studies are warranted to understand the nanoscale domains in fluorite-structured ferroelectrics.

III. DOMAIN DYNAMICS AND POLARIZATION SWITCHING KINETICS

A. Classical theory of domain dynamics

The kinetics of polarization switching in ferroelectric materials under an external electric field has been one of the most important research topics in the field of ferroelectricity. From the viewpoint of the application of ferroelectrics, the switching kinetics are expected to critically affect the device performance. Thus, there have been important theoretical works to describe the polarization switching process consisting of the nucleation and growth of domains differently polarized relative to the initial poled state. The growth of domains with opposite polarization can be considered as the motion of the domain wall from the switched domains to the unswitched region. Therefore, the velocity of the domain wall is a critical factor for determining polarization switching kinetics before the coalescence stage. The relation of the switching time (τ) with applied field (E) has been well described by the empirically proven law by Merz:

$$\tau = \tau_0 \exp\left(\frac{E_a}{E}\right),\tag{1}$$

which relates the polarization switching time (and domain wall velocity) with the applied field (E). Here, E_a is the activation field, which is a temperature-dependent property of ferroelectric materials. It can be easily noticed from Eq. (1) that the switching time is monotonic with respect to the activation field, thereby suggesting that ferroelectric materials with higher activation fields would have longer switching times under the equivalently applied electric field. When the applied field increases, the polarization switching time is expected to decrease.

Merz's law describes the phenomenological observables associated with the polarization switching of ferroelectric materials. However, this model does not describe the polarization switching processes or its mechanisms. When an external field higher than the coercive field is applied to the ferroelectric material, oppositely polarized domains can nucleate and grow through domain wall motion. When the oppositely polarized nuclei grow in the pre-poled matrix, coalescence among different domains occurs and polarization switching during coalescence is not duly described by Merz's law. Thus, additional mechanisms are required to comprehensively describe polarization switching kinetics.

B. Switching kinetics for fluorite-structured polycrystalline thin films

The most widely accepted model for polarization switching kinetics based on Merz's law is the Kolmogorov–Avrami–Ishibashi (KAI) model. This simple but powerful model was developed by Ishibashi based on the theory of Kolmogorov and Avrami, and it originally accounted for crystal growth during phase transition with nucleation and growth mechanisms. $^{109-111}$ In the KAI model, when an external field is applied, the nucleation of reversed domains is supposed to occur stochastically and instantaneously, meaning that a distribution of switching times is not considered in the KAI model; instead, it is assumed that the nucleus can grow unlimitedly until it meets other domains with a constant rate determined by the applied electric field. Consequently, domain wall motion dominates the switching time over the nucleation time of reversed domains. The polarization reversal $[\Delta P(t)]$, which is attributed to the relative fraction of the reversed domains at a given time (t) in the KAI model, is represented by

$$\Delta P(t) = 2P_s[1 - \exp\{-(t/\tau)^n\}],$$
 (2)

which is similar to the Avrami equation showing the time-dependent relative fraction of the transformed crystalline phase. ¹¹¹ The P_s , τ , and n are the spontaneous polarization, switching time, and dimensionality factor, respectively. Despite the simple form of Eq. (2), the KAI model has been reported to describe the polarization switching kinetics in single crystalline bulk and thin films, which can be relatively free from the spatial inhomogeneities caused by various factors associated with polycrystallinity. ^{112–117}

For polycrystalline ferroelectrics, which are generally expected to have spatial inhomogeneities in various aspects, their polarization switching kinetics are more complicated such that the switching kinetics cannot be duly described by the KAI model without additional assumptions regarding spatial inhomogeneities. To explain these differences, Tagantsev *et al.*¹¹⁸ proposed a new model, i.e., the NLS model, wherein it was assumed that the polarization switching rate

was determined by the nucleation of inversely polarized domains. When the growth of a single domain is considered in polarization switching according to the NLS model, the kinetics can be described by the KAI model. However, in contrast to Eq. (1) for the KAI model, the distribution in the switching time should be additionally considered to understand multidomain switching in the NLS model. As the growth of inversely polarized domains is restricted to a small volume owing to the domain wall pinning by the spatial inhomogeneities of the film stemming from various types of defects, the effect of the growth stage of the reversed domain would be negligible compared to the effect of the nucleation waiting time. Generally, the Lorentzian distribution in logarithmic switching time is considered to describe spatially inhomogeneous nucleation processes. Therefore, the time-dependent polarization switching under a constant external electric field according to the NLS model can be formulated as 118

$$\Delta P(t) = 2P_s \int_{-\infty}^{\infty} \left[1 - \exp\left\{ -(t/\tau)^n \right\} \right] F(\log \tau) d(\log \tau). \tag{3}$$

In Eq. (3), $F(\log \tau)$ is the distribution function of switching time on a logarithmic scale. Jo *et al.*¹¹⁶ suggested that the distribution could be well described based on the Lorentzian distribution as

$$F(\log \tau) = \frac{A}{\pi} \left[\frac{w}{(\log \tau - \log \tau_1)^2 + w^2} \right]. \tag{4}$$

Here, A, w, and $log \tau_1$ are a normalization constant, half width at half-maximum of the distribution, and median logarithmic value of the distribution, respectively.

Mueller and his co-workers first reported that the polarization switching of the Si-doped HfO2 film deposited via ALD could be consistently understood through the NLS model, 119 which was followed by numerous studies on nucleation-limited polarization switching kinetics in ferroelectric-doped HfO₂ films by various research groups. 95,120-123 Generally, the fluorite-structured ferroelectric thin films fabricated via ALD have been reported to contain various types of defects, including dopants, residual impurities, and grain boundaries, thereby causing inhomogeneity. The atomic layer deposited, poly-crystalline doped HfO₂ films consist of small 10-30-nm grains depending on the underlying substrate. The frequently observed grain diameters of fluorite-structured ferroelectric thin films is smaller than the conventional ferroelectric thin films such as Pb(Zr,Ti)O3 and SrBi₂Ta₂O₉ films by 1-2 orders of magnitude, and such small grain diameters critically limit the domain size. Since the domain size of the fluorite-structured ferroelectrics was determined to be smaller than 10 nm, only a few domains exist within one grain. Grain boundaries contain a high number of defects and charges, which reduce the domain wall velocity drastically by several orders of magnitude compared to the single-crystalline counterparts. Quite likely, nucleation limited switching only occurs within one grain with minimal impact on neighboring grains.

Lee et al. 95 elucidated the effect of defects on the switching kinetics and switching time distribution in TiN/Si:HfO₂/TiN capacitors, whereby an 8-nm-thick Si-doped HfO₂ film was deposited via ALD. Figures 10(a) and 10(b) show $\Delta P(t)/2P_s$ values as a function of the logarithmic width (t) of the electric pulses over a height range of 0.7–3.0 V, which is utilized for polarization switching in Si-doped HfO₂ thin films in preset (a) and woken-up (b) states, respectively.

Moreover, 10 and 10 000 cycles with a magnitude and frequency of 3 V and 10 kHz, respectively, were induced for each preset and wokenup state. To examine the effect of the heights and widths of the electric pulses, the ferroelectric Si-doped HfO₂ thin film was pre-poled using a negative electric trapezoidal pulse with a height of 3 V and width of 125 μ s for rise time and duration before applying a positive electric pulse. In fluorite-structured ferroelectric thin films deposited via ALD, the pristine P_r value is mostly unoptimized; thus, the P_s value increases with the electric field cycling with pulse trains of sufficient height, width, and number of pulses—this phenomenon is referred to as the "wake-up effect."⁷⁵ The wake-up effect has been an important research topic in the field of fluorite-structured ferroelectrics because the cycle number-dependent variations in P_s value can cause a reliability and a cost issue, especially in semiconductor devices whereby reliability is essential and cost is critical for practical applications.

In Figs. 10(a) and 10(b), the $\Delta P(t)/2P_s$ values (dots) were fitted based on the NLS model [Eq. (3)] with the assumption of the Lorentzian distribution of switching time. Figure 10(c) shows the distribution of the logarithmic switching time in the preset (solid line) and woken-up (dashed line) states in the Si-doped HfO₂ films, examined using electric pulses as high as 2.0, 2.4, and 3.0 V. From Fig. 10(c), it is evident that the width [w in Eq. (4)] of the Lorentzian distribution of $\log \tau$ decreases after wake-up field cycling. However, the median value of the logarithmic switching time, $\log \tau_1$, increases during wake-up field cycling.

Furthermore, the switching kinetics with different defect concentrations were investigated by means of Monte Carlo simulation to better understand the role of defects in polarization switching kinetics. It was assumed that the defects were randomly distributed with arbitrary magnitudes and that the defects did not drift due to the external electric field. 66,75,120 Figures 10(d)-10(f) depict the results of the Monte Carlo simulation of the ferroelectric polarization hysteresis loop and switching properties as a function of the defect ratio. Here, the 0% defect film could be considered as an ideal epitaxial film. Figure 10(d) shows the polarization vs electric field characteristics extracted by the Monte Carlo simulation, which reveals that spontaneous polarization and E_c are expected to decrease with increasing defect concentration. In Fig. 10(e), the simulated step-dependent evolutions in the $\Delta P(t)/2P_s$ values with defect concentrations of 4%, 16%, and 36% followed the solid curves of the NLS model described using Eqs. (3) and (4), while that for the 0% defect concentration was consistent with the KAI model. It should be noted that the step number of the Monte Carlo simulation can be considered to be qualitatively similar to the switching time in experiments. The distribution of $\log \tau$ in Fig. 10(f) shows that when the film contains more defects, the switching time distribution becomes broader, thereby causing a logarithmic change in the time-dependent switched polarization $[\Delta P(t)]$ under a constant electric field. This means that when the films become homogeneous, the distributions become sharpened and collapse into a delta function-like distribution, which is consistent with the ideal KAI model. Therefore, the defects of polycrystalline thin films should be one of the reasons that contribute to NLS.

Lee *et al.*¹²¹ suggested that the behavior of the partially reversed polarization in the Si-doped polycrystalline 10-nm-thick HfO_2 thin film was governed by the NLS model and that the activation field affects the switching rate by adapting to the well-known Merz's law.¹⁰⁸ Figure 11(a) shows that the $\Delta P(t)/2P_s$ value depends on the

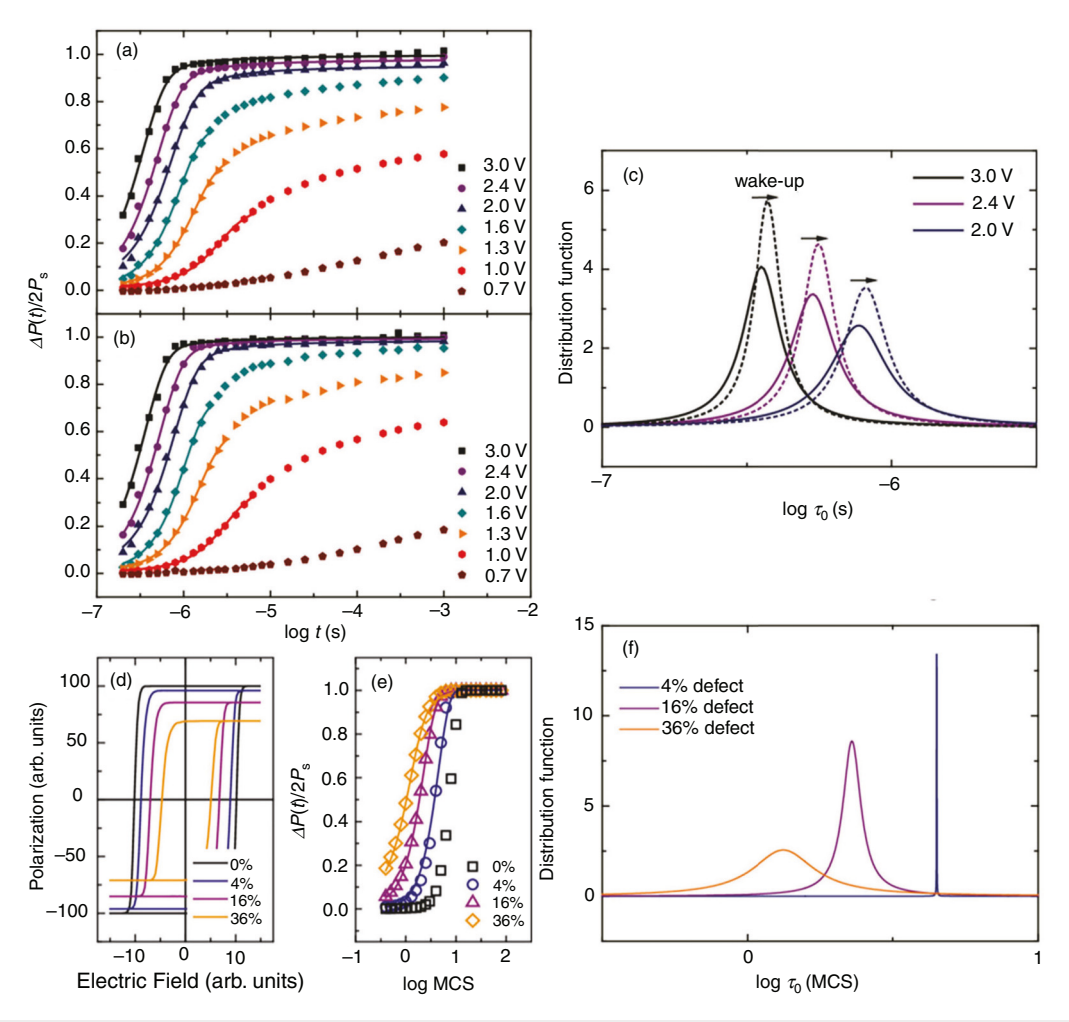


FIG. 10. Time-dependent switched polarization $[\Delta P(t)]$ as a function of the external voltage (V_{ext}) at room temperature for (a) preset and (b) woken-up. (c) Solid lines and dashed lines correspond to Lorentzian distributions of the fitting functions for preset and woken-up cells, respectively. (d) Monte Carlo simulations of the ferroelectric polarization hysteresis loop as a function of the defect ratio. (e) Monte Carlo step (MCS) dependence of ferroelectric polarization switching as a function of the defect ratio under an external field E = 9.0 (a.u.). (f) Lorentzian distributions of fitting functions for 4% (solid navy line), 16% (solid purple line), and 36% (solid orange line) defect ratios, respectively. Reproduced with permission from Lee *et al.*, ACS Appl. Mater. Interfaces 11(3), 3142–3149 (2019). (2019), American Chemical Society.

logarithmic switching time and pulse height varying from 0.9 V to 3 V. The films were pre-poled at a voltage of -3 V for 125 μs before the pulse switching measurement. The $\Delta P(t)/2P_s$ value could be consistently fitted based on Eq. (3) [see solid curves in Fig. 11(a)]. The activation field extracted from the characteristic switching time calculated from the data in Fig. 11(a) by applying Eq. (1) is 1.9 MV/cm, which is 2–6 times higher than that of conventional perovskite materials. $^{115-117}$

Lee et al.¹²¹ also utilized PFM to characterize the dynamics of the domain wall propagation under an external field according to Merz's law. Figures 11(c)-11(f) show local PFM phase images in the substrate-normal direction after applying a voltage pulse of 6 V with widths of 100 μ s, 20 ms, 100 ms, and 1 s, on the negative pre-poled regions to confirm the domain wall velocity, which is determined by its activation field and external electric field. Figure 11(g) shows the changes in the domain radius measured from the PFM images with external pulse widths. The dashed line in Fig. 11(g) is the minimum

resolution limit of the experimental setup. The applied electric field was calculated from a first-order approximation by $E = (V \cdot a)/(r \cdot d)$, where V, a, r, and d represent the applied voltage, tip radius, domain radius, and film thickness, respectively. The velocity of the domain walls to the substrate-parallel direction as a function of the calculated electric field is presented in Fig. 11(h), which is four orders of magnitude lower than the typical values of conventional ferroelectrics. Buragohain et al. 102 found a reduction in domain wall velocity by two orders of magnitude than observed in Pb(Zr,Ti)O3 in similar PFM measurements in capacitors for the same ratio of the applied field to the coercive field. Lee et al. 121 plotted ν [= 1/ τ from Eq. (1)] and estimated the activation field to be 9.3 MV/cm.¹²¹ Moreover, the energy required to change a single ferroelectric dipole to the other was also calculated theoretically using first-principles calculations. The calculated energy barrier for domain wall propagation by a distance of one unit cell in HfO_2 is 1.3 eV, which is \sim 69% higher than that of PTO

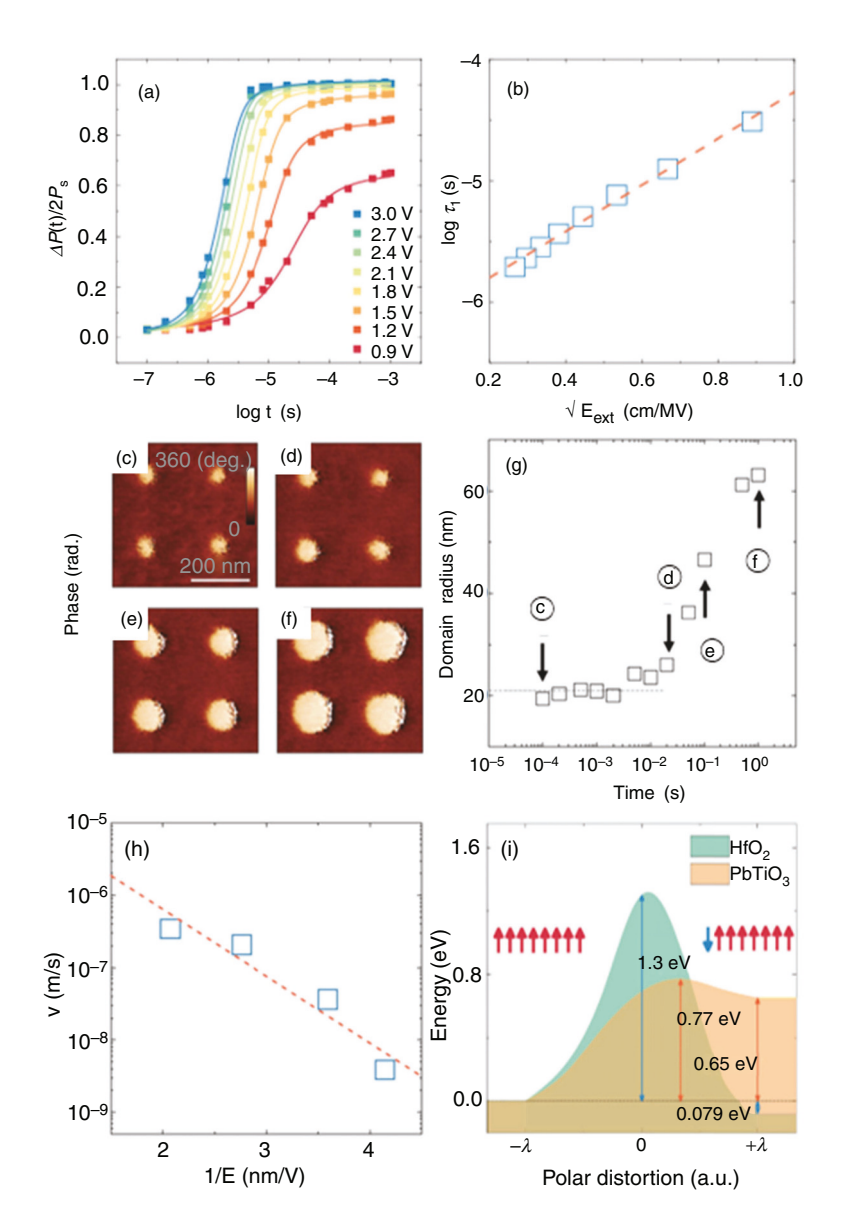


FIG. 11. (a) Time and voltage dependence of the switched polarization $\Delta P(t)$ measured at room temperature. The solid lines represent the fitting results using the NLS model, considering the Lorentzian distribution of the characteristic switching time for ferroelectric nucleation. (b) External voltage dependence of the characteristic switching time. (c-f) PFM phase images after positive poling with a pulse height of 6 V and widths of 100 μ s, 20 ms, 100 ms, and 1 s, respectively. Before the measurement, the sample was poled with a negative bias of $-6 \, \text{V}$. (g) Voltage pulse width dependence of the equivalent domain radius for the switched region. The dashed gray line represents the minimum domain size resolution (~20 nm). (h) Electric field dependence of the domain wall velocity. (i) Energy landscapes of HfO2 and PbTiO3 for a single dipole flip. Reproduced with permission from Lee et al., ACS Appl. Mater. Interfaces 11(42), 38929-38936 (2019). Copyright 2019, American Chemical Society.

(0.77 eV), as shown in Fig. 11(i). Because of the high energy barrier to flip a single dipole, it is expected that the switching speed of the partially switched states of fluorite-structured ferroelectrics will be slower while the states are more stable than those of conventional ferroelectrics, which is discussed in more detail in Sec. IV.

Hyun $et\ al.^{120}$ provided another description of the switching kinetics of polycrystalline $Hf_{0.5}Zr_{0.5}O_2$ films. They asserted that the inevitable parasitic circuit components could affect the resistance of the electrode, as well as that of the spatial heterogeneity-induced inhomogeneous field distribution. They applied a switching dynamic model based on an inhomogeneous field mechanism (IFM) suggested by Zhukov $et\ al.,^{127}$ considering the inevitable circuit components for describing the switching dynamics. Figure 12(a) depicts the circuit model with the parasitic circuit components, which has been studied by Hyun and co-workers. In Fig. 12(a), serial resistance R_s is the total resistance that

probably originates from various resistances, such as electrode resistance, contact resistance of probe and electrode, as well as internal resistance of the analyzer. Parasitic capacitance $C_{\rm p}$ could originate from the non-ferroelectric phase in the ferroelectric film and capacitance of the circuit components. Moreover, i_R is the current that flows through $R_{\rm s}$, which is expected to be affected by time-dependent changes in the various circuit parameters affecting $R_{\rm s}$ and $C_{\rm p}$. When the voltage is applied to the schematic measurement circuit, including the ferroelectric capacitor, $C_{\rm p}$ is expected to be charged first because the charging of the dielectric capacitor is generally faster than the polarization switching of ferroelectrics. When the voltage V_0 is applied, the dielectric charging current i_p can be formulated as

$$i_R = i_p = \frac{V_0 - V_F}{R_s} \exp\left(-\frac{t}{R_s C_p}\right). \tag{5}$$

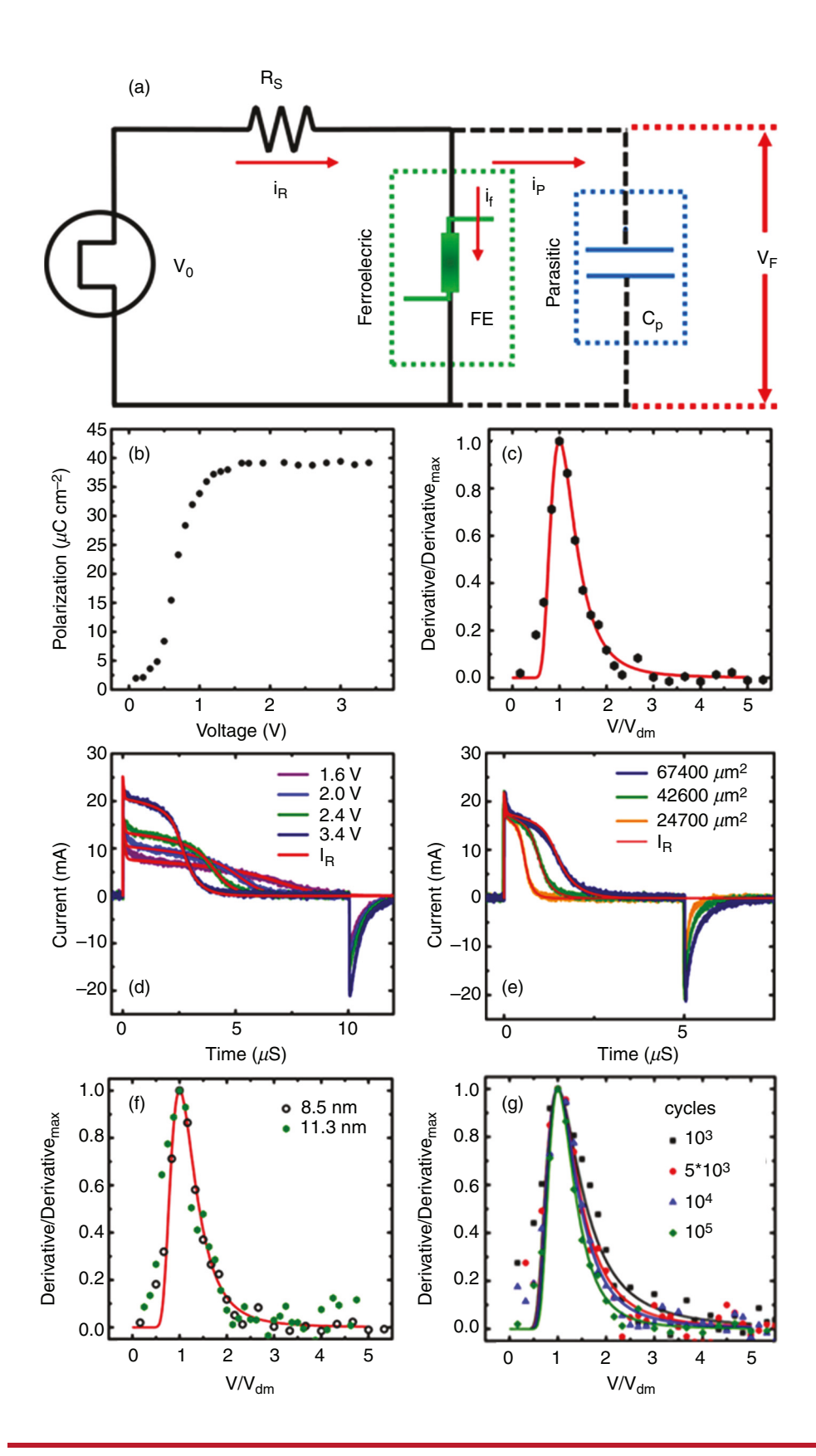


FIG. 12. (a) Schematic diagram of the composed testing circuit for pulse measurement with a nonlinear switching element (dotted green box) and a parasitic capacitance element (dotted blue box). (b) Voltage dependence of polarization reversal of the 8.5-nm-thick Hf_{0.5}Zr_{0.5}O₂ (HZO) film with an electrode area of $102\,300\,\mu\text{m}^2$. (c) Normalized derivative of polarization reversal as a function of normalized voltage and fitted curve based on the IFM model (red line). (d) Switching current with various applied voltages and simulated curve based on Eq. (7) (red lines). (e) Switching current of the 8.9-nmthick film with various electrode areas under 3.56 V (4 MV/cm) and simulated curve based on Eq. (7) (red lines). (f) Normalized derivative of polarization reversal as a function of normalized voltage in 8.5-nm-thick (black circle) and 11.3-nm-thick (green dot) HZO films and fitted curve based on the IFM model (red line). (g) Normalized derivative of polarization reversal as a function of normalized voltage in the 8.5-nm-thick HZO film with wake-up cycle various Reproduced with permission from Hyun et al., ACS Appl. Mater. Interfaces 10(41), 35374–35384 (2018). Copyright 2018, American Chemical Society.

When the polarization of the ferroelectric begins to switch, the current i_f flowing to the ferroelectric capacitor can be calculated as

$$i_f = A \frac{dP(t, V_F)}{dt}. (6)$$

In Eq. (6), A represents the area of the ferroelectric capacitor; thus, the current i_R according to Kirchhoff's law can be calculated as

$$i_R = i_p + i_f = \frac{V_0 - V_F}{R_s} = C_p \frac{dV_F}{dt} + A \frac{dP(t, V_F)}{dt}.$$
 (7)

According to the IFM model, the local field (E) in the ferroelectric capacitor is not equivalent to the macroscopic electric field ($E_{\rm F}$) owing to the spatial inhomogeneity. Consequently, the spatial inhomogeneity is expected to show a distribution of switching times, τ in Eq. (1). The distribution of the normalized field (E/E_F) is supposed to comply with a Gaussian distribution. Consequently, polarization reversal $\Delta P(E_{\rm F},t)$ is determined as

$$\Delta P(E_F, t) = P_s erfc \left[\frac{\frac{E_a}{E_F \ln(1/\tau_0)} - 1}{\sigma \sqrt{2}} \right]. \tag{8}$$

In Eq. (8), σ represents the standard deviation of E/E_F. Figure 12(b) shows the polarization reversal [Δ P(V,t)] of 8.5-nm-thick Hf_{0.5}Zr_{0.5}O₂ thin films with an electrode area of 102 300 μ m² as a function of the electric pulse height at a pulse width of 10 μ s. Figure 12(c) shows the normalized derivative of the polarization reversal (∂ Δ P/ ∂ V_F) as a function of V/V_{dm}, where V_{dm} is the voltage whereat the derivative of polarization reversal is maximum. According to the IFM model, the normalized derivative of Δ P(V,t) can be fitted as follows:

$$\frac{\partial \Delta P(V,t)/\partial V}{\partial \Delta P(V,t)/\partial V|_{max}} = \frac{1}{\xi^2} \exp\left[1 - \frac{1}{\xi^2} - \gamma \frac{(1-\xi)^2}{\xi^2}\right]. \tag{9}$$

In Eq. (9), ξ denotes V/V_{dm}, and $\gamma = 2/(\sqrt{1+8\sigma^2}-1)$; thus, σ can be calculated. C_p can be determined by integrating the discharging current over t, while R_s can be derived from the RC constant estimated from the exponentially decaying discharging current. Finally, the switching current presented in Fig. 12(d) can be predicted using Eq. (7) by adjusting the E_a and τ_0 values in Eq. (8). The activation field estimated from the linear plot of log (switching time) vs the inverse of the electric field was 8.94 MV/cm, and $\tau_0 = 10^{-10}$ s. As shown in Fig. 12(e), the switching time increased with the electrode area. This is because the larger electrode area causes a higher C_p value, which cannot be examined by means of the NLS model. Furthermore, Hyun $et\ al.^{120}$ compared the polarization switching behavior according to the IFM model in 8.5- and 11-nm-thick $Hf_{0.5}Zr_{0.5}O_2$ thin films. Thicker films are expected to have a higher fraction of the nonpolar

monoclinic phase according to the surface/grain boundary energy model. 14,44,50 However, the differences in the normalized derivative of $\Delta P(V,t)$ vs the V/V_{dm} plot in Fig. 12(f) were negligible. Hyun et al. 12 suggested that the monoclinic phase grains and ferroelectric orthorhombic phase grains would exist in parallel; thus, the monoclinic phase grains would negligibly affect the homogeneity of the field distribution along the substrate-normal direction, thereby resulting in polarization switching kinetics. Figure 12(g) shows the normalized derivative-normalized voltage plot analyzed after 10^3 , 5×10^3 , 10^4 , and 10⁵ field cycles during the endurance test to examine the effect of wake-up field cycles. The parameters extracted from the results are summarized in Table II. The R_s values presented in Table II are analogous before and after the cycles because there is nothing to be changed by wake-up cycle relating to R_s, which primarily represent the spreading resistance of the electrode. During wake-up field cycling, it is suggested that the increase in P_r and the decrease in ε_r are accompanied by the transition from the tetragonal to orthorhombic phase.¹ Moreover, charged oxygen vacancies, which are concentrated at the interfacial region adjacent to the electrodes, are redistributed throughout the film more homogeneously during repetitive electric field cycling. It is expected that the distribution of the local electric field would become narrow because this distribution depends on the distribution of charged defect concentrations in the film. Additionally, charge injection, domain depinning, and local breakdown of interfacial regions can occur. 134 Local phase transitions, from the non-polar tetragonal to the polar orthorhombic phase, ferroelastic polar axis orientation changes, charge injection, and redistribution of charged defects are expected to narrow the distribution of the local electric field; thus, the σ values would decrease with an increasing number of wake-up field cycles during the endurance test. Therefore, the IFM model modified by Hyun et al. 120 could be used to reasonably describe the switching kinetics of fluorite-structured ferroelectrics with various reliable parameters.

More recently, Materano $et~al.^{122}$ examined various switching mechanism models in doped HfO_2 thin films. First, they considered the Landau–Khalatnikhov (LK) model originating from the Landau–Devonshire (LD) theory describing the double-well-shaped free energy in ferroelectric materials. The switching event is described as the transition from one energy minimum to the other, which is promoted by the application of an external electric field, and can be written as

$$G = \frac{\alpha}{2}P^2 + \frac{\beta}{4}P^4 + \frac{\gamma}{6}P^6 - PE,\tag{10}$$

where $\alpha = \alpha_0$ (T – T₀), while coefficients β and γ are negative and positive, respectively. The minimum free energy with respect to the polarization P can be expressed for the electric field as

TABLE II. Kinetic parameters extracted by pulse measurement and fitting with various wake-up cycle numbers. Reproduced with permission from Hyun *et al.*, ACS Appl. Mater. Interfaces **10**(41), 35374–35384 (2018). Description of the permission of the permission from Hyun *et al.*, ACS Appl. Mater. Interfaces **10**(41), 35374–35384 (2018).

Cycles	$2P_{\rm r}$ [μ C cm ⁻²]	σ	$R_s \; [\Omega]$	$C_p[nF]$	$E_a [MV cm^{-1}]$	$\tau_0~[\times 10^{-11} \mathrm{s}]$	A $[\mu m^2]$
10	31.6	0.53	147	4.16	9.76	14	105 300
5×10^3	34	0.43	151	3.94	9.41	12	106 300
10^4	36	0.37	156	3.79	9.12	11	102 000
10^{5}	40	0.32	135	3.77	8.94	10	102 300

$$E = \alpha P + \beta P^3 + \gamma P^5. \tag{11}$$

The graph of Eq. (11) is an S-shaped curve for P–E characteristics, from which the intrinsic coercive field, on which the energy barrier between the two polarization states totally disappears, can be estimated. Since the intrinsic coercive field is one that flips the entire polarization direction of unit cells, the experimental coercive field is significantly lower than the intrinsic coercive field. Although the LK model shows differences in usual measurements, this approach is useful for evaluating the negative capacitance (NC) effect predicted by the LD theory or accumulative polarization switching under a subcoercive electric field. Als, 138, 139

Materano et al.122 also examined the coercive field of Hf_{0.5}Zr_{0.5}O₂ films deposited via ALD using the Du-Chen model, which was similar to the classical nucleation theory (CNT) approach based on the perspective of Gibbs energy. 108,140,141 This approach for HfO2-based ferroelectrics was first proposed by Mulaosmanovic et al. 123 In the CNT, the formation of the new phase generates a change in the free energy in the material. The Gibbs free energy deceased by the volume and increased by the surface, thereby stabilizing the barrier of the new phase. When the radii of the nuclei reach the critical values of the critical energy barrier, the nuclei can grow by the probability of the Arrhenius relation. 142 The Du-Chen model, in the case of domain switching, supposes that the nucleation of the reversed domain governs domain switching, similar to the NLS model; thus, the kinetics of domain switching are related to the rates of the nuclei to overcome the critical energy barrier. The energy barrier can be lowered by the applied electric field; therefore, the average nucleation waiting time (τ), which is a reciprocal of the nucleation rate, can be expressed as

$$\tau = \tau_0 \exp\left(\frac{\alpha}{k_B T} \cdot \frac{1}{V_{sw}^2}\right),\tag{12}$$

where τ_0 is the proportionality constant, α is a parameter associated with the free energy of the domain properties of the material, k_B is the Boltzmann's constant, and V_{sw} is the switching voltage. Equation (13) was first derived in Ref. 123 for FeFET, which is a study we will discuss in Sec. III C. In the study by Materano *et al.*, ¹²² they reconsidered Eq. (13) and plotted the time applied to the field until there occurred a 50% switched polarization state of the Hf_{0.5}Zr_{0.5}O₂ film with respect to the switching voltage, which showed that the average nucleation waiting time decreased as the voltage increased.

When the ferroelectric film becomes thinner, the stability of the switched domain can also be affected. It is known that the film has a higher coercive field than the thicker ferroelectric film, which is called the size effect. Tagantsev formulated the size effect as a relation between the coercive field and the film thickness L, $E_c \sim L^{-2/3}$, 145,146 but the actual relation of the size effect was approximately the grain size d rather than the film thickness, as demonstrated by Materano $et\ al.$ with differently doped and deposited thin HfO_2 films; thus, it should be $E_c \sim d^{-2/3} \cdot (1.147-149)$ For example, when plotting the relationship between the thickness and the coercive field of the ZrO_2 prepared through chemical solution deposition, it does not appear to follow the aforementioned relationship. However, when the thickness of the thin film prepared via CSD is 30 nm or more, it is known that the average grain size is 10 to 20 nm, and it seems to follow the trend well when the thin film is plotted vs the grain size instead of the thickness of the thin film. 148

Meanwhile, the IFM model has been applied to the same material using Eq. (9), and it seemingly provides a good fit of the experimental data. Notably, no phenomenological description of the polarization switching is provided by the IFM model, which performs a statistical analysis based on the principle that each single grain perceives a different local field according to its surroundings. They insisted that when the three models were combined, a more complete picture, including thermodynamic, kinetic, statistic, macro- and microscopic aspects of switching in thin HfO_2 -based films, could be obtained.

C. Polarization switching of fluorite-structured ferroelectrics in nanoscale devices

The nucleation process in ferroelectric materials is generally known to be stochastic, and stochastic polarization switching is expected when nucleation governs the polarization switching process. 109-111,116,118 For large-scale ferroelectrics, polarization switching seems to occur continuously with stochastic switching time following the Lorentzian distribution because the time differences among nucleation events are infinitely small. The statistically averaged behavior of NLS in ferroelectrics is expected to resemble deterministic polarization switching rather than nanoscale stochastic polarization switching. However, for nanoscale devices with several grains and nucleation sites, the polarization reversal could show a discontinuous stochastic tendency because of the various values of coercive voltage. 123 The discontinuous stochastic behavior is one of the key properties for materials applicable to artificial neurons, which show potential pulses when the neuron reaches a certain threshold potential by external stimuli. Thus, materials with stochastic behaviors are highly important toward achieving artificial neurons for the nonvolatile memory (NVM) approach for neuromorphic computing.

Mulaosmanovic et al. 123 reported the stochastic behavior of a nanoscale FeFET comprising ferroelectric Si-doped HfO2 gate oxide with a 30-nm-long and 80-nm-wide channel (L_G and W, respectively). The schematic structure of the FeFET with the Si-doped HfO2 is shown in Fig. 13(a). Figure 13(b) shows the I_D-V_G (gate voltage) curves analyzed using a pulse train, the schematic of which is shown in the inset of Fig. 13(b). The pulse train is composed of positive write pulses (V_p > 0), whose height increases successively and negative reset pulses $(V_N = -5 \text{ V})$ with a pulse width (t_{PW}) of 500 ns to reset the polarization state. They assumed that the nanoscale FeFET had three columnar grains with three different coercive voltages, which give rise to three abrupt changes in the I_D-V_G curve by controlling the write pulse height. Another critical factor that influences polarization switching by an electric pulse is the pulse width. Figure 13(c) shows the changes in V_T (threshold voltage) as a function of t_{PW} when V_P ranges between 2.2 and 2.8 V. The schematic pulse train is shown in the inset of Fig. 13(c), and the effect of controlling t_{PW} was conducted 20 times for each V_P value. As shown in Fig. 13(c), the abrupt V_T changes, with steps consisting of a few grains having analogous coercive voltages, could be confirmed by controlling t_{PW} for various V_P values. Figure 13(d) shows the standard deviation of the switching time, in which abrupt V_T changes could be observed from the 20 repeated experiments shown in Fig. 13(c). The polycrystalline Si-doped HfO₂ thin films used in this study are generally spatially inhomogeneous with defects, including residual impurities and grain boundaries. Thus, it was hypothesized that the switching kinetics of the FeFET was purely governed by the NLS concept, based on the

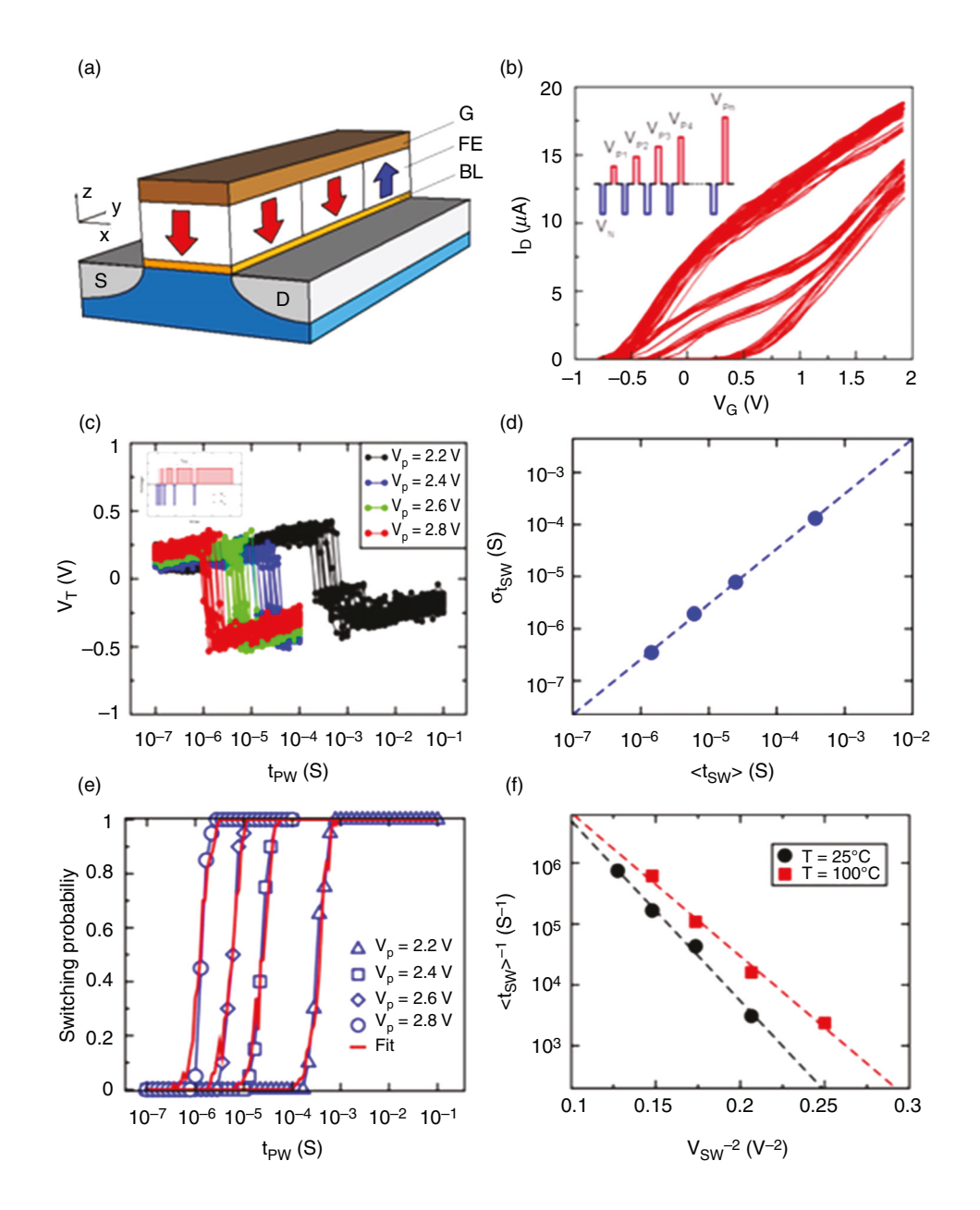


FIG. 13. (a) Schematic illustration of an FeFET structure. (b) I_D-V_G curve readout after each of the progressively increasing V_P pulses in the inset. (c) V_T vs t_{PW} graph corresponding to 20 repetitions of procedure in the inset with the gate voltage waveform with logarithmically increasing pulse width t_{PW} shown for four different V_P levels. For $V_P=$ 2.8, 2.6, and 2.4 V, the measurement was truncated at tPW = 100 μ s, in order not to stress the device over longer pulse widths. (d) Standard deviation vs mean value of switching time t_{SW} extracted from (c). (e) Fitting of switching probability curves corresponding to four different VP levels used in (c). (f) The plot of experimental mean switching time t_{SW} vs switching voltage for two different temperatures is in agreement with nucleation dominated switching model. Reproduced with permission Mulaosmanovic et al., ACS Appl. Mater. Interfaces 9(4), 3792-3798 (2017). 2017, American Chemical Copyright Society.

Du–Chen model presented in Eq. (12) regarding the critical number of generated nuclei, n, which can be expressed as

$$\tau_n = \tau_{n0} \exp\left(\frac{\alpha}{k_B T} \cdot \frac{1}{V_{\text{cw}}^2}\right),\tag{13}$$

where τ_{n0} is the shortest nucleation time. The generation rate of the switched nucleus is $\lambda_n = 1/\tau_n$, while the time elapsed between each nucleus generation is ΔT_i . They assumed that the switching process follows the Poisson process; thus, the probability density function of ΔT_i was suggested according to Eq. (14) as follows:

$$p_{\Delta T_i} = \lambda_n e^{-\lambda_n \Delta T_i}. (14)$$

Here, the total switching time of polarization reversal is the sum of each time, ΔT_b elapsing between the generation of nuclei about the total number of nuclei n:

$$t_{SW} = \sum_{i=1}^{n} \Delta T_i, \tag{15}$$

and the mean value and variance of t_{sw} can be written as Eqs. (16) and (17), respectively:

$$\langle t_{sw} \rangle = \frac{n}{\lambda_w}$$
 (16)

and

$$\sigma_{t_{sw}}^2 = \frac{n}{\lambda_u^2}.$$
 (17)

From the results presented in Figs. 13(c) and 13(d), it is possible to obtain n and λ_n using Eqs. (16) and (17). Here, the fitted number of n was five, according to the work of Mulaosmanovic $et~al.^{123}$ By using the n value, it is possible to obtain t_{sw} in probabilistic switching according to Eq. (14) by summing up ΔT_{is} which is exponentially distributed as described by Eq. (15). Figure 13(e) shows the switching probability— t_{PW} curves for V_P values of 2.2 to 2.8 V with the fitted curves (red curves) based on the measured results (open dots). Figure 13(f) shows the $\langle t_{sw} \rangle^{-1} - V_{sw}^{-2}$ plot, which is consistent with Eq. (13), wherein $\langle t_{sw} \rangle^{-1}$ increases with temperature when V_{sw} is fixed. This behavior is qualitatively in agreement with the Du–Chen model and experimental switching observations in ferroelectric capacitors. 141

In summary, although the KAI model could simulate the switching kinetics of epitaxial films and single crystals, the polarization switching kinetics of the ALD fluorite-structured ferroelectrics could not be described with the KAI model. The spatial inhomogeneities in fluorite-structured ferroelectric thin films should be considered to understand their polarization switching kinetics. Lee et al. 95 examined the impact of defects on the polarization switching kinetics influenced by the wake-up effect and showed that polarization switching kinetics could be understood based on the NLS model. Moreover, the high activation field of fluorite-structured ferroelectrics compared to that of conventional ferroelectrics could be confirmed by applying classical domain wall dynamics, thereby obeying Merz's law. 121 Hyun et al. 120 suggested that inhomogeneous film and parasitic circuit components could cause inhomogeneous field distributions in ferroelectric Hf_{0.5}Zr_{0.5}O₂ thin films, so they adopted the IFM model to explain their switching kinetics. Materano et al. 222 showed that the LK, Du-Chen, and IFM models did not mutually exclude each other but rather described different aspects of the polarization switching phenomenon and could contribute toward forming a complete picture of the latter. However, for nanoscale devices, Mulaosmanovic reported stochastic switching kinetics of the fluorite-structured ferroelectrics with a stepwise and abrupt V_T change, which could be attributed to the stochastic NLS of several grains. 123 The stochastic polarization switching was suggested to be a key property for achieving neuronal behaviors in NVM neuromorphic computing, which would be discussed in detail in Sec. IV.

IV. NEUROMORPHIC COMPUTING BASED ON FLUORITE-STRUCTURED FERROELECTRICS

A. Neuromorphic computing based on ferroelectricity

In Secs. II and III, the characteristics of domains and their dynamics in fluorite-structured ferroelectrics in theoretical and experimental studies were comprehensively reviewed. From theoretical works, the energy barrier between the two polarization states of the $Pca2_1$ orthorhombic phase has been established to be as high as \sim 40 meV/atom (\sim 120 meV/f.u.), which is several times higher than that in conventional ferroelectrics, such as BaTiO₃. ^{15,76,85} The experimentally observed high coercive field can be attributed to the high kinetic energy barrier, although the practical polarization switching is governed by the nucleation and growth mechanism, wherein the coercive field is much lower than the intrinsic coercive field. From a recent computational simulation conducted by Lee *et al.*, ⁹² the width of the domain wall in the fluorite-structured ferroelectric was reported to be

zero because of the existence of the Pbca orthorhombic phase whose unit cell is identical to the two parallel $Pca2_1$ orthorhombic unit cells with the two opposite polarizations. Interestingly, the free energy of the Pbca phase, which is identical to the 180° domain wall in the $Pca2_1$ orthorhombic phase was reported to be even lower than that of the $Pca2_1$ orthorhombic phase. Such a trend has been confirmed in several computational simulations, even without considering domain walls. From the classical viewpoint of domain wall energy, this result implies that the domain wall energy is negative, which is contradictory to conventional ferroelectric knowledge.

Another strikingly important point is that the energy barrier heights between the partially switched polarization states are much higher than those in conventional perovskite-structured ferroelectrics. 92 This result was consistent with the high activation field experimentally estimated in Chae et al.'s work, 121 which assumed that the domain wall motion in fluorite-structured ferroelectrics could be modeled by canonical Merz's law and estimated an activation field of 9300 kV/cm, which was 4.9 times higher than that of ferroelectric BaTiO₃. However, the high energy barrier between partial polarization states also implies that the partially switched polarization states would remain stable owing to the high energy barriers. Chae et al. 121 also examined the retention of the partial polarization states using a ferroelectric tester and reported that the partial polarization states could remain stable for over 1000 s, even at an elevated temperature of 85 °C. The high energy barrier between different polarization states would result in a high activation field required for the domain wall motion and long retention time of the partial polarization states.

The multiple polarization states and resulting multiple conductivity states of fluorite-structured ferroelectrics that can be formed in FeFETs or FTJs are known to be suitable for neuromorphic memory applications. Yoon *et al.*¹⁵¹ suggested that the partial polarization states of perovskite-structured ferroelectrics could be formed by various forms of pulse trains, which they referred to as adaptive learning. After this pioneering work, the ferroelectric materials and electronic devices they fabricated have been considered as promising candidates for neuromorphic systems. ^{5,150,152–165}

Fluorite-structured ferroelectrics, such as HfO₂ and ZrO₂, are currently used in commercial semiconductor devices such as gate oxides in metal–oxide–semiconductor field-effect transistors (MOSFETs) and the dielectric layer in cell capacitors of dynamic random-access memories, thereby proving that fluorite-structured ferroelectrics are compatible with the state-of-the-art CMOS technology. ¹⁶⁶ Therefore, devices utilizing fluorite-structured ferroelectrics to mimic synapses and neurons should be highly promising from the viewpoint of materials science and engineering.

Among various ferroelectric memory devices, FeFETs and FTJs are considered to be suitable for synaptic analog devices in neuromorphic computing systems because their synaptic weight can be controlled by multilevel conductivity, which is coupled to the polarization states. 162 Notwithstanding their rather short history of $\sim\!10\,\mathrm{years}$, FeFETs and FTJs containing fluorite-structured ferroelectrics have been reported to exhibit performances suitable for synaptic devices in spiking neural networks (SNNs). Besides, neuronal device is another application of FeFETs, with their characteristic role as an integrator of electric pulses, as demonstrated in a recent work. 150 Previous research on neuromorphic computing applications of fluorite-structured ferroelectrics are comprehensively reviewed in this section.

The biological neuromorphic system consists of two main units: neurons and synapses, which should be mimicked by an electronic device to achieve an artificial neuromorphic computing system through two main approaches: one is to utilize state-of-the-art CMOS technology, while the other is to utilize novel types of devices like emerging nonvolatile memories. In the former method, circuit units are fabricated with MOSFETs to mimic the operation of neurons and synapses, whereas in the latter approach utilizes novel devices, and most prominent nonvolatile memory devices, such as resistive switching memories, phase-change memories, FeFETs, FTJs, and floating gate or charge trapping transistors. Currently, artificial neurons and synapses fabricated based on CMOS can exhibit performances superior to those of the novel device approach, and a CMOS-based system is used in the current neuromorphic computing system. However, the energy and area efficiency of the CMOS-based approach is insufficient; thus, the novel device approach is also attracting interest to achieve energy and area efficiency in neuromorphic computing systems. In this section, our main focus is on utilizing emerging fluoritestructured ferroelectrics in emerging nonvolatile memory approaches.

B. Artificial synapses based on fluorite-structured ferroelectrics

It is already known that FeFETs and FTJs can be utilized for emerging neuromorphic computing systems, and this has been recently reviewed by Oh et al. 162 However, conventional ferroelectric materials, such as perovskite-structured ferroelectrics, have suffered from their insufficient scalability (the device scaling was stopped at the 130 nm technology node) and incompatibility with the CMOS system. The ferroelectricity discovered in doped HfO2 and ZrO2 in 2011 revived the research on ferroelectric memory devices with their scalability and CMOS compatibility. Notwithstanding its short history, a 28-nm-long FeFET channel was fabricated and reported in 2012. In that report, a bistable channel memory window of 0.8 V could be achieved, although its endurance was limited to $\sim 10^4$ – 10^5 program/ erase cycles. It was also confirmed that the fluorite-structured ferroelectrics is compatible with standard materials in the semiconductor industry, such as Si and metal nitrides. 8,9,166,167 With the established ALD technique, fluorite-structured ferroelectric thin films could be uniformly deposited on three-dimensional nanostructures. 8,9,166 By employing ALD techniques, FTJs with fluorite-structured ferroelectrics were also fabricated with two distinguishable tunneling electroresistance states. 170 Fujii et al. 171 first reported the FTJ with ferroelectric HZO followed by numerous reports on FTJs with ferroelectric-doped -6,172-174 Since the discovery of ferroelectricity in HfO2 or HZO.3fluorite-structured oxides, such as HfO2 and ZrO2, ferroelectric memory devices could compete with other emerging memory devices, such as resistive and phase-change random-access memories, based on the previously mentioned properties.

Oh *et al.*¹⁶² examined the partial polarization switching behavior of TiN/Hf_{0.5}Zr_{0.5}O₂/TiN capacitors using various types of pulse trains and suggested that FeFETs with the ferroelectric Hf_{0.5}Zr_{0.5}O₂ gate oxide could be utilized as synaptic devices with multilevel channel conductivity, which were achievable by various Hf_{0.5}Zr_{0.5}O₂ polarization states. Figures 14(a)–14(c) show the pulse trains consisting of pulses with identical heights and widths, pulses with increasing widths, and pulses with increasing heights, respectively. ¹⁶² Figures 14(d) and 14(e) show the pulse number-dependent polarization states during the (d)

potentiation and (e) depression processes of the TiN/HZO/TiN capacitor with the three different previously mentioned schemes of pulse trains, as presented in Figs. 14(a)–14(c). As shown in Figs. 14(d) and 14(e), Scheme C, consisting of a pulse train with increasing height, showed the most promising potentiation and depression with the widest available range of polarization states. However, for the cases of Scheme A of the pulse train with identical height and width, as well as Scheme B of pulse train with increasing width, the maximum achievable polarization was restricted to less than 1/3 of that of Scheme C. Thus, Oh *et al.* ¹⁶² concluded that Scheme C should be the most appropriate for the synaptic operation of the ferroelectric TiN/HZO/TiN capacitor with the largest number of polarization states to reliably achieve multilevel polarization states.

Figure 14(f) shows the cycle-to-cycle variation for each of the 32 polarization states measured in 10 switching cycles for Scheme C, and the absence of overlap of the adjacent polarization states can be confirmed from the result, at least for the 10 repetitive potentiation/depression processes. Figure 14(g) shows 32 levels of drain current (I_d, left y-axis) and channel conductivity (G, right y-axis) during potentiation and depression process at a read voltage (V_{read}) of 0.5 V obtained from simulation. Although Oh *et al.* did not fabricate FeFET devices with ferroelectric HZO gate oxides, the multilevel channel conductivity, which was governed by the polarization states of the ferroelectric gate oxide, could be simulated, as shown in Fig. 14(g).

Mulaosmanovic *et al.*¹⁶¹ proposed an FeFET-based synapse fabricated via a CMOS-compatible high-k metal gate process, using a 10-nm-thick Si-doped HfO₂ film as the ferroelectric layer. Both the channel width and length of the FeFET were 500 nm. The authors adopted non-identical pulses (increasing pulse height and width) to achieve a large number of intermediate conductance states (> 30) for both switching transitions (i.e., from P \downarrow to P \uparrow , and vice versa), which corresponded to the processes of potentiation and depression of synaptic weights. Finally, the authors demonstrate the spike-timing-dependent plasticity (STDP) rule, which is believed to underlie the memory and learning mechanisms in the biological brain and is essential to SNNs.

Kim and Lee¹⁵⁸ fabricated a ferroelectric thin-film transistor (FeTFT) with an Indium Gallium Zinc Oxide (IGZO) channel and $Hf_{0.5}Zr_{0.5}O_2$ gate oxide and examined its analog synaptic behavior. Figure 15(a) shows the schematic structure of the fabricated FeTFT, while Fig. 15(b) shows the drain current–gate voltage transfer curve when the drain–source voltage was fixed at 1 V. ¹⁵⁸ The characteristic anticlockwise hysteresis could be confirmed, thereby proving that the channel conductivity could be controlled by the polarization of $Hf_{0.5}Zr_{0.5}O_2$. Moreover, the gate leakage current (I_G) could be controlled under 10^{-8} A, thereby showing that the changes in I_{DS} did not originate from the gate leakage current.

To examine the synaptic behavior with the multilevel conductivity of IGZO controlled by the polarization states of $Hf_{0.5}Zr_{0.5}O_2$, the type of pulse train should be decided among the various types discussed in Figs. 14(a)-14(c). In the work conducted by Kim and Lee, ¹⁵⁸ the pulse train with increasing height was utilized similar to the work by Oh and co-workers, ¹⁶² as shown in Figs. 15(c) and 15(d). To evaluate the potentiation and depression processes of the synaptic devices, the pulse schematics in Figs. 15(c) and 15(d) were adopted, respectively. It should be noted that the pulse height increased from 2.7 to

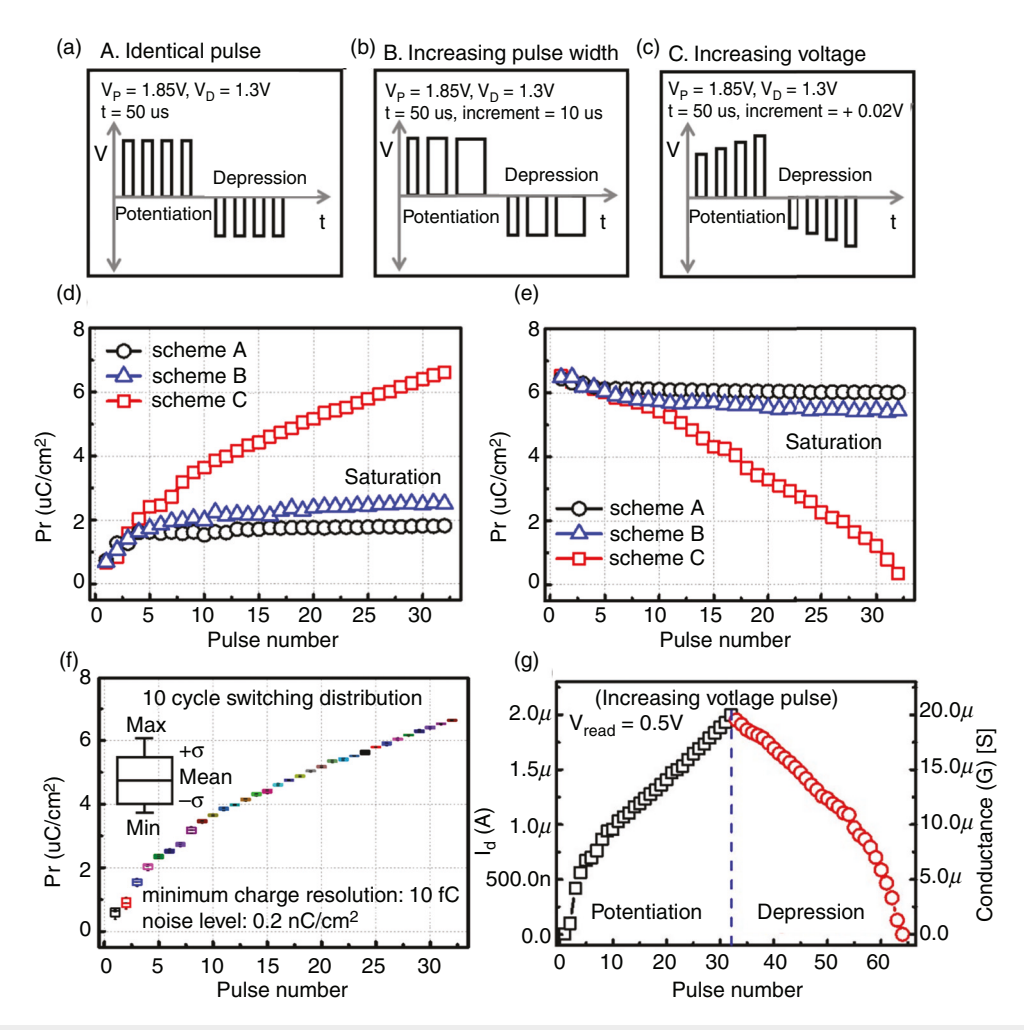


FIG. 14. (a)–(c) Various programing pulse schemes applied to the TiN/HZO/TiN stack. (d) Potentiation and (e) depression characteristics of the polarization state of the TiN/HZO/TiN capacitor. (f) Cycle-to-cycle variation of each polarization state during 10 switching cycles for Scheme C. (g) FET drain current and conductance for 32 levels of the potentiation and depression curve at V_{read} = 0.5 V obtained from simulations. Reproduced with permission from Oh *et al.*, IEEE Electron Devices Lett. **38**(6), 732–735 (2017). Copyright 2017, IEEE.

 $4.3~\rm V$ with a step size of $25~\rm mV$ in the pulse train used for potentiation, while the increment was from $-2~\rm to$ $-3.6~\rm V$ in the pulse train used for depression, also at a step size of $25~\rm mV$. From the polarization–voltage curve of the Al/IGZO/HZO/TiN capacitor, the ferroelectric hysteresis was slightly imprinted to the positive bias region; thus, different pulse trains heights were used for the potentiation and depression processes.

Figure 15(e) depicts the evolution of conductance during the potentiation and depression processes conducted using the schemes presented in Figs. 15(c) and 15(d). Sixty-four different levels of conductance could be reliably formed, thereby suggesting the multilevel conductivity control via the polarization states of HZO. The linearity parameters for potentiation and depression were -0.8028 and -0.6979, whereas the G_{max}/G_{min} ratio was higher than 10. An artificial neural network was simulated to perform supervised learning on the Modified National Institute of Standard and Technology database. A two-

multilayer perceptron neural network with 400 input neurons and 10 output neurons was utilized [Fig. 15(f)]. The details of the simulation can be found in the paper by Kim and Lee. As shown in Fig. 15(g), a 91.1% accuracy could be achieved after 125 training epochs, which was comparable to the recognition accuracy of 94.1% for the ideal synapse neural network. Such a high accuracy could be attributed to the 64 levels of conductance states with good linearity ($A_{\rm p}\approx-0.8028$ and $A_{\rm d}\approx-0.6979$) and $G_{\rm max}/G_{\rm min}$ values higher than 10.

Kim and Lee¹⁵⁸ also examined the cycle-to-cycle variation from the endurance test of 100 potentiation and depression processes, while Figs. 15(h) and 15(i) show the variations in the 64 conductance levels from the endurance test. The cycle-to-cycle variation was 2.36%, thereby proving the reliable operation of the fabricated ferroelectric synaptic device. The device-to-device variation was also examined for 40 different FeTFTs, and it was found to be as low as 3.93%, thereby proving the uniformity of the fabricated array of the FeTFTs. This

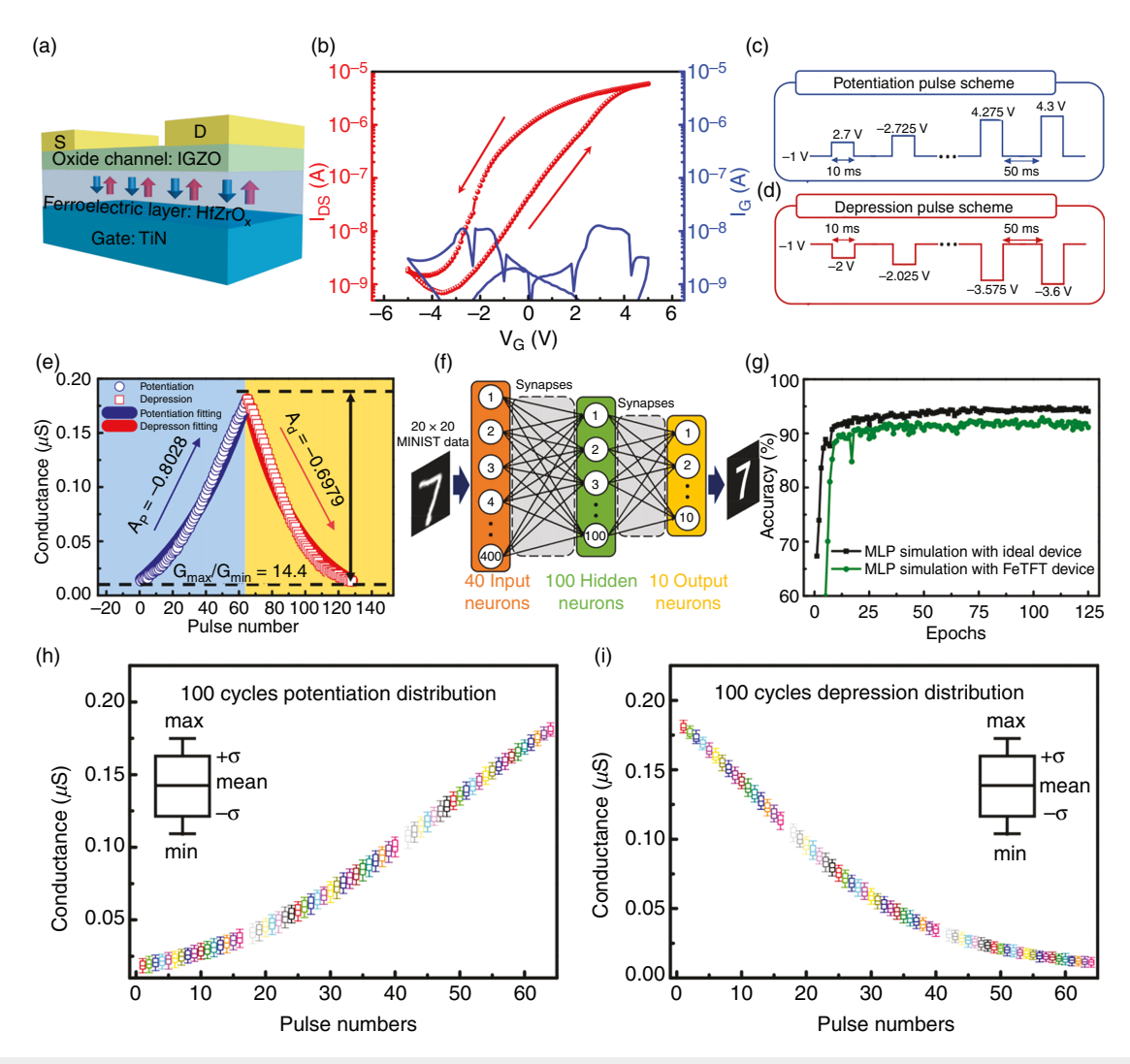


FIG. 15. (a) Schematic structure of ferroelectric thin-film transistor (FeTFT). (b) Transfer curve of FeTFT. Pulse schemes for (c) potentiation and (d) depression applied to the gate electrode. (e) Potentiation and depression properties of the FeTFT with incremental pulse schemes. (f) Schematic illustration of two-layer multilayer perceptron neural network. (g) Simulated pattern recognition accuracy of the two-layer multilayer perceptron neural network based on FeTFTs compared to an ideal neuromorphic device. Cycle-to-cycle variations of (h) potentiation and (i) depression operations for 100 cycles. Reproduced with permission from Kim and Lee, Nano Lett. 19(3), 2044–2050 (2019). Copyright 2019, American Chemical Society.

could be attributed to the well-established ALD process for the ferroelectric HZO.

Another important device for ferroelectric synapses is FTJ, which utilizes the polarization-dependent tunneling conduction of charge carriers through an ultrathin ferroelectric film. In FTJs, the quantum-mechanical tunneling current through the ferroelectric layer could be controlled by its polarization, and this concept was first suggested by Esaki *et al.*¹⁷⁵ in 1971. However, the experimental proof of the tunneling electroresistance (TER) effect on the free surface of ferroelectric materials was provided in 2009 by several independent research groups. ^{176,177} Subsequently, numerous works ^{3-6,152,155,160,170,172-174,178-184} on practical FTJs have been conducted. In a broad definition, an FTJ can be categorized into one of the resistive switching mechanisms; ¹⁸⁵ its application to synaptic devices is identical to that of memristors in principle. The film thickness of

fluorite-structured ferroelectrics required to have a tunneling current density sufficient for distinguishing between ON and OFF states is even smaller than that used for FeFETs. Generally, few-nm-thick films are in high demand because the tunneling current density exponentially decreases with the film thickness. This is tough to achieve if the ferroelectric is polycrystalline as in ALD grown fluorite structured ferroelectrics. Therefore, the double-layer FTJ is often utilized where a very thin dielectric tunneling layer is used in series with the ferroelectric to decouple the tunneling from the ferroelectric layer. ^{173,185–190}

In 2016, Chernikova *et al.*¹⁹¹ reported ferroelectricity in a 2.5-nm-thick $Hf_{0.5}Zr_{0.5}O_2$ film directly formed on a Si substrate via PFM. Although the tunneling current density was not investigated in that study, the film thickness of 2.5 nm was identical to the 5-unit cells, which should be sufficiently thin to achieve sufficient tunneling current. ¹⁹¹ Fujii

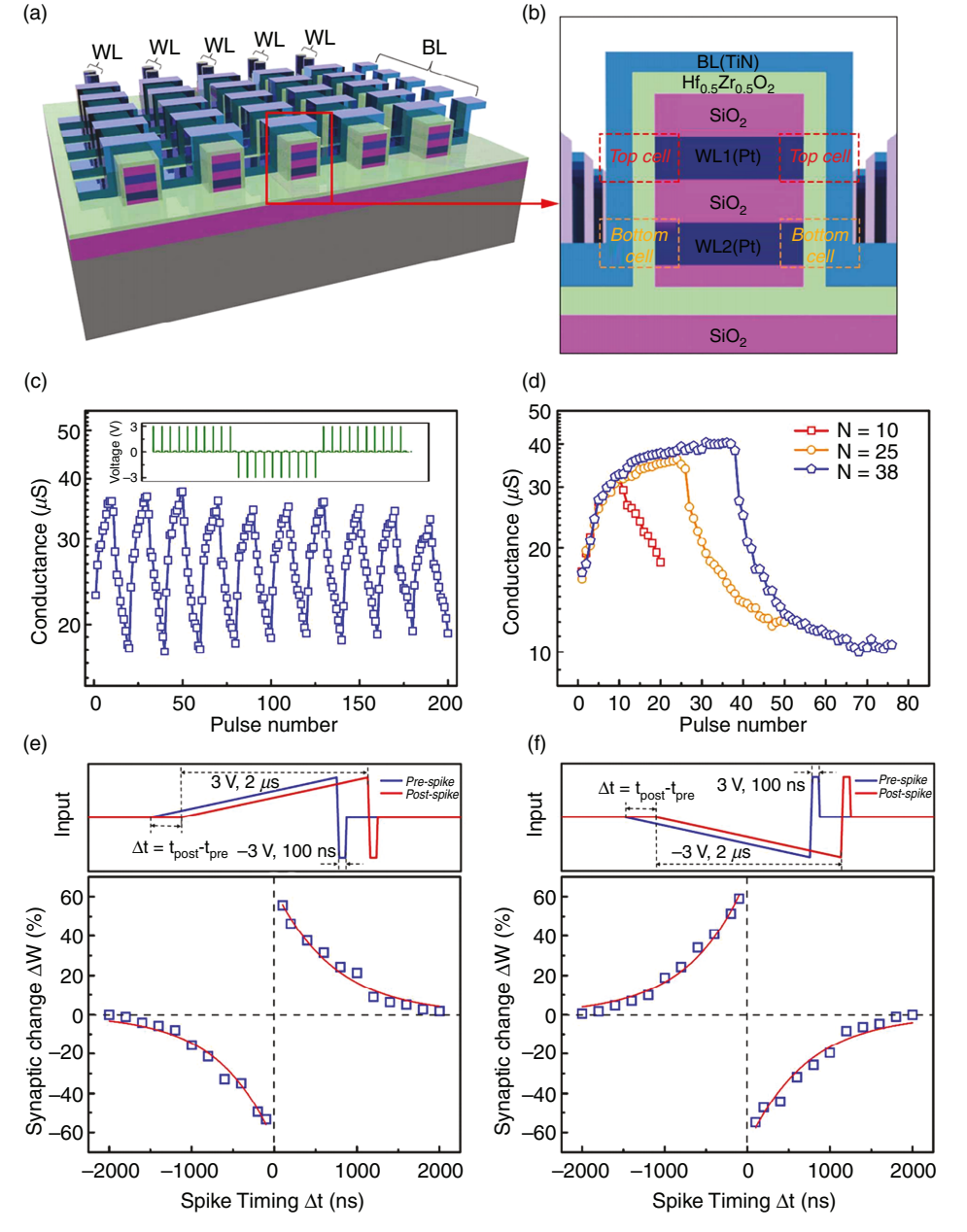


FIG. 16. 3D vertical ferroelectric HZObased FTJ array characterization. (a) The schematic diagram of high-density 3D vertical HZO-based FTJ array. (b) Zoomed-in schematic of the 3D TiN/FE-HZO/Pt devices located at the sidewall. Key features of biological synapse implementation in HZO-based FTJs. (c) The synaptic longterm potentiation and depression characteristics in HZO-based FTJs. Potentiation/ depression pulse: ±3 V, 100 ns. Read pulse: 0.1 V, 1 μ s. (d) Synaptic long-term potentiation and depression characteristics under different potentiation/depression pulse numbers (N = 10, 25, 38). (e) Hebbian STDP rule scheme and (f) anti-Hebbian STDP rule scheme in the HZObased synaptic array. The red lines are the exponential fits to the experimental data. Reproduced with permission from et al., Nanoscale Chen 15826-15833 (2018).⁵ Copyright 2018, Royal Society of Chemistry.

et al. 171 demonstrated an FTJ with ferroelectric Si-doped HfO₂, but the electrode materials were not written in the report. Interestingly, the self-rectifying behavior with an on current lower than 100 nA was also confirmed. The programed and erased conductivity state could be distinguished even after 10 years from the extrapolation of the retention test result, but a decrease in the TER ratio could also be observed. Ambriz-Vargas et al. 192 reported a CMOS-compatible FTJ based on a \sim 3-nm-thick Hf_{0.5}Zr_{0.5}O₂ tunneling layer and bottom TiN electrode formed on a p-type Si substrate. A TER ratio of 15 could be achieved, and the result could be consistently understood based on the theoretical band structure of the ferroelectric capacitor. 192 Tian and Toriumi 170 also reported the polarization-dependent control of the tunneling current in an

asymmetric Ag/Y:HfO₂/TiN capacitor, whereby the thickness of Y:HfO₂ was only 3 nm. A TER ratio of 100 could be achieved, and a reliable operation could be confirmed with 100 repetitive switching cycles. When the current density is compared to the FTJs with conventional ferroelectrics, both the ON and OFF current densities are lower than those of conventional ferroelectrics. Go and Jeon⁶ comprehensively studied the effect of bottom electrode materials, such as TiN, Si, SiGe, and Ge, on the performance of an FTJ with a 6-nm-thick Hf_{0.5}Zr_{0.5}O₂ tunneling oxide. Among the four examined bottom electrodes, the FTJ formed on the Ge substrate showed the most promising performance with a TER ratio of 30, extrapolated retention up to 10 years at 85 °C, and endurance of up to 10^7 switching cycles.⁶

In the publications cited in the previous paragraph, the FTJs were considered for classical NVM devices with two distinguishable tunneling current levels. However, it has been shown that the FTJ can be utilized for synaptic devices with multilevel tunneling current density, which is governed by the polarization state of the ferroelectric tunneling layer. ^{153,156,157,159,162,165} Boyn *et al.* ¹⁵² reported the synaptic STDP behavior of their Pt/Co/BiFeO₃/(Ca,Ce)MnO₃ FTJ formed on a YAlO₃ substrate with a 4.6-nm-thick BiFeO₃ tunneling layer. Guo *et al.* ¹⁵⁵ examined the synaptic plasticity of 5-unit-cell-thick BaTiO₃ with BO₂-and AO-type interfaces, and showed that the synaptic behavior could be controlled by interface engineering.

In addition to previous reports on ferroelectric synaptic devices with perovskite-structured ferroelectrics, FTJs with fluorite-structured ferroelectrics have been reported by several research groups despite their relatively short research history. Chen et al. 5 fabricated Pt/ Hf_{0.5}Zr_{0.5}O₂/TiN FTJs with the nanoscale three-dimensional structure shown in Figs. 16(a) and 16(b). Figure 16(a) shows a schematic diagram of a high-density three-dimensional vertical HZO-based FTJ array, while Fig. 16(b) shows the zoomed-in schematic of the threedimensional TiN/FE-HZO/Pt devices located at the sidewall.5 As shown in Fig. 16(a), the FTJ array is based on a crossbar array, which is considered suitable for artificial arrays of synaptic devices, while each FTJ unit consists of top and bottom cells separated by insulating SiO₂, as shown in Fig. 16(b), and Fig. 16(c) shows the synaptic longterm potentiation and depression characteristics in the HZO-based FTJs depicted in Figs. 16(a) and 16(b). The potentiation and depression processes consist of 10 positive and negative electrical pulses with 10 different conductivity states. Figure 16(d) shows the synaptic longterm potentiation and depression characteristics under different potentiation/depression pulse numbers (N = 10, 25, 38). Figures 16(e) and 16(f) show the Hebbian STDP rule scheme and the anti-Hebbian STDP rule scheme (top panel), respectively, with the resulting synaptic change in percentage as a function of time difference between the spiking pulses of pre-synaptic and post-synaptic neurons in the HZObased synaptic array. The red lines in Figs. 16(e) and 16(f) are the exponential fits to the experimental data, while the blue open squares represent the experimental data. Besides the FTJ synapses based on single ferroelectric layers, there have been reports on FTJ synapses based on ferroelectric/dielectric bilayers. 189,190 While FTJs with single ultrathin ferroelectric layers suffer from rather small polarization and high leakage current even at high TER state, high polarization and low leakage current could be utilized for the bilayer FTJs.1

C. Artificial neurons based on fluorite-structured ferroelectrics

In the previous paragraphs, the synaptic behavior of FeFETs and FTJs has been reviewed, but other important devices are artificial neurons, whose typical characteristics are described with the well-known leaky integrate-and-fire (IF) model. On the one hand, with synaptic devices the gradual changes in conductance can be induced by the potentiation and depression pulse trains, while with artificial neurons, on the other hand, the electric pulses are expected to be integrated without external change in conductivity, but the abrupt firing is expected when the number of electric pulses reaches a critical number.

Mulaosmanovic *et al.*^{123,150,161} examined the polarization switching kinetics of nanoscale ferroelectric transistors, with a channel length of 28 nm, when excited with sub-coercive pulse trains. Figure 17(a)

shows the schematic structure of the FeFET utilized in their study with the downward polarization vector P, while Fig. 17(b) shows the crosssectional TEM image of a device with a channel length (L) of 30 nm and a channel width (W) of 80 nm. The "G," "D," and "S" shown in Fig. 17(b) indicate the gate, drain, and source terminals, respectively. The device structure of the FeFET is, in principle, identical to that of the MOSFETs used in CMOS; thus, proving the CMOS compatibility of FeFETs with fluorite-structured ferroelectrics. The only difference is that the crystalline phase of the HfO2 gate oxide ferroelectric orthorhombic phase is induced by doping of a small amount of Si and additional annealing for crystallization, which is different from the amorphous phase used in MOSFETs. It should be noted that the channel length and width of the FeFET is several orders of magnitude lower than that used for the synaptic device shown in Fig. 15. Figures 17(c) and 17(d) show the IF behavior evolving with the positive and negative sub-coercive pulses shown as schemes in insets of Figs. 17(c) and 17(d). The transition from the OFF to the ON state [Fig. 17(c)] was conducted with positive pulses (V_P) with a height and width of 2.2 V and $1 \mu s$, respectively, while the transition from the ON to the OFF state [Fig. 17(d)] was conducted with negative pulses (V_N) with a height and width of $-3.25\,\mathrm{V}$ and $1\,\mu\mathrm{s}$, respectively. The IF behavior that is different from the large-scale FeFET device could be attributed to a much lower number of switchable ferroelectric domains in the gate stack. Mulaosmanovic et al. 123,150,161 suggested that a critical number of nanodomains are nucleated, which triggers the abrupt polarization reversal of the entire grain connecting the two terminals when the number of sub-coercive pulses reaches a critical value. With any lower number of pulses, the dispersed (not fully connected) nanodomains cannot induce a conducting path through the semiconducting channel.

Figure 17(e) shows the pulsing scheme for implementing an IF cycle and an arbitrary refractory period, after which a new IF cycle begins (upper panel) and consecutively repeats the IF cycles for different V_P values, while maintaining t_P at 1 μs (bottom panel). It can be observed that the critical number of pulses required for the firing process decreases with the V_P. This result implies that the nucleation of nanodomains is more frequent with higher V_P values. The properties of the FeFETs described in Figs. 17(c)-17(e) are IF behaviors with no leaky characteristics. Notably, it is different from the dynamics of neurons with the absence of a leaky behavior; thus, the other part would be required to mimic biological neurons. However, the additional device for the leaky behavior should increase the size of the artificial neurons, which is one key merit of the NVM approach. Mulaosmanovic et al. 150 suggested that the leaky behavior could be added to ideal FeFETs by utilizing the depolarization field, which had been considered harmful for the nonvolatility of FeFETs. When the polarization of the ferroelectric layer cannot be fully compensated by the charge carriers in the semiconductor channel due to the nonferroelectric interfacial layer, there should be an internal depolarization field. To simulate such cases, Mulaosmanovic et al. 150 utilized the inhibiting voltage (V_{inh}) between the V_P pulses. Figure 17(f) depicts the situation when V_{inh} is applied in the intervals between consecutive V_{P} pulses (t $_{\rm inh}=10~\mu s$). Moreover, $V_{\rm inh}$ emulates the effect that would have the depolarization field in a device with a thicker interface as it tends to reduce the integration efficiency of the V_P pulses (upper panel), and the number of pulses required for switching increases as V_{inh} increases in magnitude, which is equivalent to an increase in the

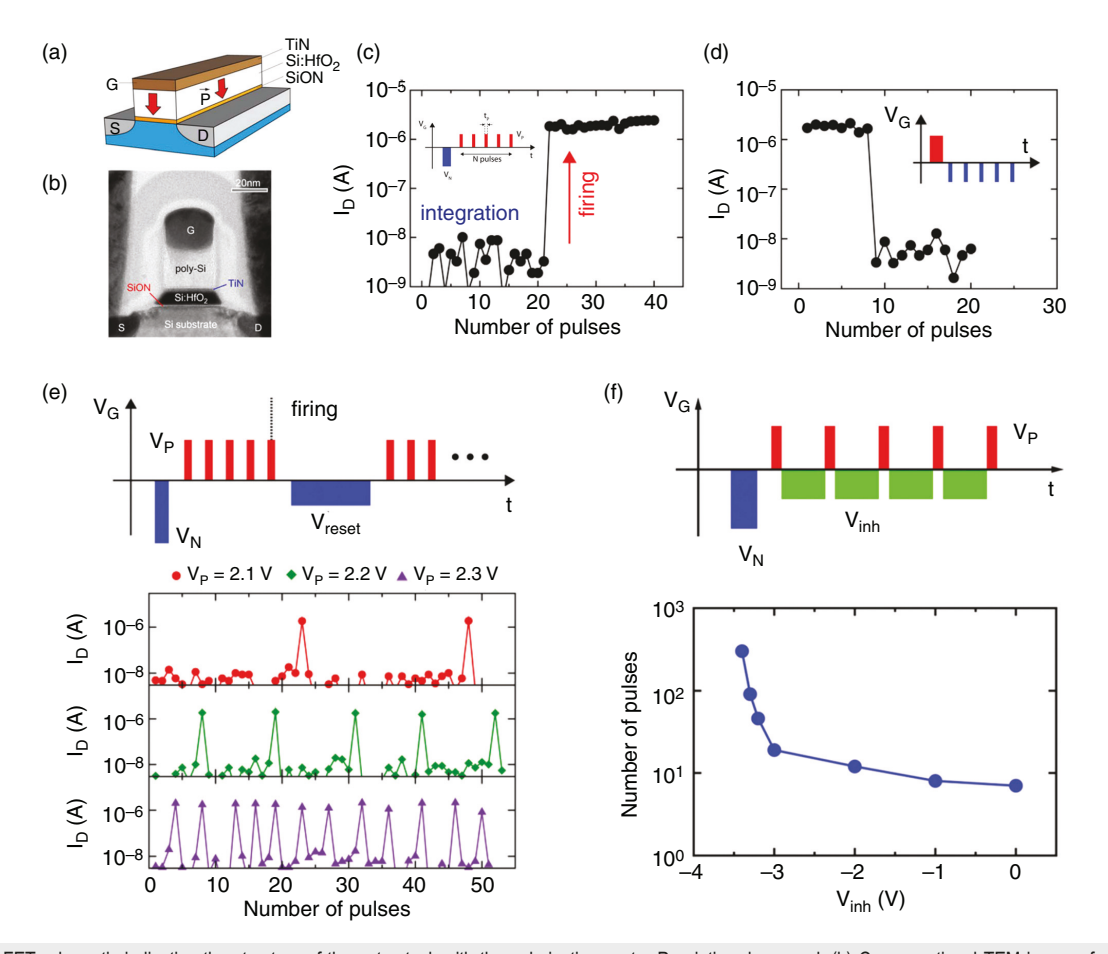


FIG. 17. (a) FeFET schematic indicating the structure of the gate-stack with the polarization vector P pointing downward. (b) Cross-sectional TEM image of a device having L = 30 nm and W = 80 nm for the channel length and width, respectively. The "G," "D," and "S" indicate the gate, drain, and source terminals, respectively. (c) Transition from the OFF to the ON state with pulses $V_P = 2.2 \text{ V}$, $t_P = 1 \mu \text{s}$ and (d) from the ON to the OFF state with negative pulses $V_N = -3.25 \text{ V}$, $t_P = 1 \mu \text{s}$ with pulsing schematics (inset). (e) Pulsing scheme for implementing an IF cycle and an arbitrary refractory period, whereafter a new IF cycle begins (upper panel) and consecutively repeated IF cycles occur for different V_P while keeping $t_P = 1 \mu \text{s}$ (bottom panel). (f) Inhibiting voltage V_{inh} was applied in the intervals between consecutive V_P pulses ($t_{inh} = 10 \mu \text{s}$). $V_{inh} = 0.0 \mu \text{s}$). V_P is always kept constant at 2.2 V, $v_P = 0.0 \mu \text{s}$. T (bottom panel). Reproduced with permission from Mulaosmanovic *et al.*, Nanoscale 10(46), 21755–21763 (2018).

leakage effect. In practical devices, the depolarization field originating from the incomplete compensation of the ferroelectric polarization is expected to have an effect equivalent to that of $V_{\rm inh}$ used in the work by Mulaosmanovic and co-workers. ¹⁵⁰

By using the FeFETs with emerging fluorite-structured ferroelectrics, the circuital complexity could be significantly reduced. Several units, such as membrane capacitors, amplification circuity, and thresholding circuitry required in CMOS-based neuron circuits, are not required. Consequently, the energy and area efficiency were expected to be significantly improved. As shown in Figs. 17(c) and 17(d), both positive and negative excitation can be integrated, which is expected to provide flexibility in neuromorphic circuit design for both excitatory and inhibitory stimuli. The CMOS-based compatibility and scalability of fluorite-structured ferroelectrics are expected to provide significant values based on the conventional CMOS technology.

D. Perspectives on neuromorphic computing based on fluorite-structured ferroelectrics

In this section, previous studies on artificial synapses and neurons based on fluorite-structured ferroelectrics are reviewed. Although the history of this research topic is rather short, some promising properties for both artificial synapses and neurons could be achieved. However, there are several issues to be considered for the practical utilization of fluorite-structured ferroelectrics in neuromorphic computing systems, and these issues will be discussed from the viewpoint of the material.

For ferroelectric synaptic devices, reliable multilevel conductivity, which can be controlled by polarization, is required. In large-scale FeFETs and FTJs, multilevel conductivities of up to 64 levels have been experimentally achieved. However, the dimensions of the fabricated FeFETs ranged from 10^2 nm to 10^2 μ m, which surpassed the

state-of-the-art feature size by 1-4 orders of magnitude. The number of grains in the aforementioned large-scale devices would be in the range of 10² to 10⁸ when the lateral grain size was assumed to be \sim 10 nm. Therefore, the situation in nanoscale FeFETs or FTJs should be different from that observed in large-scale devices. Mulaosmanovic et al. 150 experimentally reported that the switching behavior observed in nanoscale FeFETs was completely different from that in large-scale devices, and that nanoscale FeFETs could be utilized for artificial neurons. The ideally achievable number of polarization states can be discussed based on the recent computer simulation conducted by Lee and co-workers. 92 As discussed in Sec. II, they suggested that each active layer contributing to polarization switching is separated by an inactive spacer layer; thus, the polarization state could be controlled layer by layer. For the case of the FeFET with a 28-nm-long channel, the number of active layers and the resulting number of polarization states is expected to be \sim 56, which is already smaller than that achieved by Kim and Lee. 92 When the channel length is decreased to 10 nm, the maximum achievable number of polarization states through layer-by-layer switching is only ~20. Notably, this issue affects FTJs, especially when metal-ferroelectric-metal, metalferroelectric-semiconductor, metal-ferroelectric-insulator-metal, or metal-ferroelectric-insulator-semiconductor capacitors are formed in a planar structure, which can be easily noticed from their principle of operation.

Thus, a potential issue for synaptic devices based on fluoritestructured ferroelectrics is the maximum achievable number of conductivity states, which is strongly coupled to the active interfacial area between the ferroelectric and semiconductor channels in FeFETs (or the metal electrodes in FTJs). To maintain a sufficient number of conductivity levels with decreasing feature sizes, vertical FDSOIs or ferroelectric fin field-effect transistors (FinFETs) can be solutions, and they are capable of increasing the vertical interfacial area without increasing the lateral feature size. Since the established ALD techniques can be used for both HfO2 and ZrO2 for depositing ferroelectric gate oxides in FinFET structures, ferroelectric FinFETs can be fabricated. Krivokapic et al. 193 fabricated and characterized 14 nm ferroelectric FinFET technology with Hf_{0.5}Zr_{0.5}O₂ gate oxide, although the controllability of multilevel conductivity was not studied in their report. A similar approach can be applied to FTJs. It has already been proven that three-dimensional metal-ferroelectric-metal capacitors with a ferroelectric capacitive layer can be fabricated in several previous works. 168,169 As shown in Fig. 16, Chen et al. 5 already demonstrated the synaptic operation of FTJs with vertical ferroelectric Hf_{0.5}Zr_{0.5}O₂ thin films, and according to the authors, the vertical width of the active Hf_{0.5}Zr_{0.5}O₂ thin film was defined using a 50-nm-thick Pt electrode.⁵ Another approach is the grain size engineering of the fluoritestructured ferroelectrics. As suggested by Mulosmanovic et al., 194 the polarization switching in fluorite-structured ferroelectric thin films occurs with the single domain switching in each columnar grain. Thus, increasing areal density of grains by decreasing the lateral grain size would be one effective way to increase the available polarization states. The insertion of Al₂O₃ interlayer was suggested to effectively decrease the lateral grain size in previous works. 195 The other strategy is to increase the thickness of the ferroelectric gate oxide in FeFETs. The memory window of FeFETs is theoretically $(2 \times E_c \times thickness)$ so it is linearly proportional to the film thickness. The wide saturated memory window suggests that the available number of ΔV_{th} values of

partially switched states increased as suggested by Mulaos manovic and co-workers. $^{196}\,$

The other issue related to ferroelectric artificial synapses entails that a pulse train with increasing height [scheme in Fig. 14(c)] is required, rather than ideal identical pulse trains [scheme in Fig. 14(a)]. This implies that an additional external circuit is required to control the height of the pulse train. This might be attributed to the spatially inhomogeneous distribution of the coercive voltage, which can originate from various factors such as spatially inhomogeneous texture, doping concentration, impurity concentration, and strain. Among these various factors, the mixed texture with a randomly distributed orientation is critical. Thus, the deposition technique for ferroelectric thin films with a preferred orientation serves as a promising solution to mitigate the distribution of coercive voltage. For FTJs, the bottom electrode materials can be changed for the local epitaxial growth of fluorite-structured ferroelectric thin films. In previous reports, the (111) Pt bottom electrode is effective ¹⁹⁷ for the growth of (111)oriented $Hf_{0.5}Zr_{0.5}O_2$ or ZrO_2 thin films, ^{198,199} and it remains a potential solution to decrease the distribution of coercive voltage. In 2020, Mulaosmanovic et al. showed that synaptic potentiation and depression are possible with identical pulses, which are highly desirable for neuromorphic on-chip applications. Continuous multilevel tuning is possible across the entire conductance range of an FeFET. The linearity of the synaptic weight update can be easily tuned by varying the pulse height of the train of identical pulses, which should be an important step in the progress of ferroelectricbased synaptic devices.

In the case of artificial neurons based on fluorite-structured ferroelectrics, the neuronal IF behavior was proven in nanoscale FeFETs with a 28-nm-long channel. Thus, the operation of the single device would be free from the unexpected issues accompanied by size shrinking different from the artificial synapses. However, when arrays consisting of numerous artificial neurons are formed for practical devices, the device-to-device variation can be a critical issue. When the arrays of FeFETs with fluorite-structured ferroelectrics are fabricated, quite large device-to-device variations have been reported in several previous studies.² Such variations could be attributed to the spatial inhomogeneities already discussed in the previous paragraphs on potential issues of ferroelectric artificial synapses. Cycle-to-cycle variation might be another issue, although it has been suggested that the stochastic nature can be harnessed for emulating the probabilistic activity of biological neurons. The device-to-device and cycle-to-cycle variations might affect the accuracy of neuronal processes with arrays of large numbers of artificial neurons. As studies on the stochastic nature of ferroelectric neurons remain insufficient to date, this issue requires further study.

V. CONCLUSION

In this review, we comprehensively assess the current state of knowledge and opportunities related to domains and domain dynamics in emerging fluorite-structured ferroelectrics. The polymorphism in fluorite-structured ferroelectrics is complicated because of the competition among various crystalline phases with small free energy differences. Several phases can coexist even in a single grain, which can transform to the other phases in response to external factors, including electric fields and defects. The non-ferroelectric phase, as well as defects including residual impurities, dopants, and grain boundaries,

can be a source for spatial inhomogeneities in fluorite-structured ferroelectrics. Thus, the polarization switching kinetics of fluorite-structured ferroelectrics could be described considering spatial inhomogeneities based on an NLS model or inhomogeneous field model.

Furthermore, the nanoscale FeFET containing ferroelectric Sidoped HfO_2 can exhibit a stochastic behavior, which is expected when polarization switching is purely governed by the nucleation process. Because of the stochastic nature, nanoscale fluorite-structured ferroelectrics can have promising applications as artificial neurons in neuromorphic computing, as demonstrated by Mulaosmanovic *et al.*, ¹⁵⁰ which manifests a leaky IF behavior. By using electric pulses lower than the coercive field, the abrupt stochastic polarization switching can be confirmed.

Another striking property of fluorite-structured ferroelectrics has been discovered in domain walls from computational simulations. It was shown that the domain wall thickness of the fluorite-structured ferroelectrics could be zero with the existence of the *Pbca* orthorhombic phase at the 180° domain wall, whereas the free energy is even lower than that at the *Pca2*₁ ferroelectric phase. Moreover, the coupling between the neighboring threefold-coordinated oxygen ions, whose displacement is the origin of the polarization switching, is negligible, thereby suggesting that the partially switched states with mixed up and down domains are expected to have sufficient retention. Thus, the ability of fluorite-structured ferroelectrics to have numerous polarization states promotes their application in neuromorphic computing because artificial synapses can be achieved.

AUTHORS' CONTRIBUTIONS

D.H.L. and Y.L. contributed equally to this work.

ACKNOWLEDGMENTS

This work was supported by the National Research Foundation of Korea funded by the Ministry of Science and ICT (Grant Nos. 2020R1C1C1008193, 2020M3F3A2A01081593). This research was partly supported by the BK21 FOUR (Fostering Outstanding Universities for Research) funded by the Ministry of Education (MOE, Korea) and National Research Foundation of Korea (NRF). M.H.P. is supported by the POSCO Science Fellowship of the TJ Park Science Foundation. J.L.J. and Y.L. acknowledge support from the National Science Foundation (NSF), as part of the Center for Dielectrics and Piezoelectrics (CDP), under Grant Nos. IIP-1841453 and IIP-1841466.

DATA AVAILABILITY

Data sharing is not applicable to this article as no new data were created or analyzed in this study.

REFERENCES

- ¹J. Müller, E. Yurchuk, T. Schlösser, J. Paul, R. Hoffmann, S. Müller, D. Martin, S. Slesazeck, P. Polakowski, and J. Sundqvist, 2012 Symposium on VLSI Technology (VLSIT) (2012), pp. 25–26.
- ²S. Dünkel, M. Trentzsch, R. Richter, P. Moll, C. Fuchs, O. Gehring, M. Majer, S. Wittek, B. Müller, and T. Melde, 2017 IEEE International Electron Devices Meetingtell (IEDM) (2017), pp. 19.17.11–19.17.14.
- ³F. Ambriz-Vargas, G. Kolhatkar, M. Broyer, A. Hadj-Youssef, R. Nouar, A. Sarkissian, R. Thomas, C. Gomez-Yáñez, M. A. Gauthier, and A. Ruediger, ACS Appl. Mater. Interfaces 9(15), 13262–13268 (2017).

- ⁴S. S. Cheema, N. Shanker, C.-H. Hsu, A. Datar, J. Bae, D. Kwon, and S. Salahuddin, arXiv:2007.06182 (2020).
- ⁵L. Chen, T.-Y. Wang, Y.-W. Dai, M.-Y. Cha, H. Zhu, Q.-Q. Sun, S.-J. Ding, P. Zhou, L. Chua, and D. W. Zhang, Nanoscale 10(33), 15826–15833 (2018).
- ⁶Y. Goh and S. Jeon, Nanotechnology **29**(33), 335201 (2018).
- ⁷J. Okuno, T. Kunihiro, K. Konishi, H. Meamura, Y. Shuto, F. Sugaya, M. Materano, R. Ali, K. Kuehnel, K. Seidel, U. Schroeder, T. Mikolajick, M. Tsukamoto, and T. Umebayashi, in 2020 IEEE Symposium on VLSI Technology (IEEE, 2020).
- ⁸M. H. Park, Y. H. Lee, T. Mikolajick, U. Schroeder, and C. S. Hwang, MRS Commun. 8(3), 795–808 (2018).
- ⁹T. Mikolajick, S. Slesazeck, M. H. Park, and U. Schroeder, MRS Bull. 43(5), 340–346 (2018).
- 10 T. Böscke, J. Müller, D. Bräuhaus, U. Schröder, and U. Böttger, Appl. Phys. Lett. 99(10), 102903 (2011).
- ¹¹X. Sang, E. D. Grimley, T. Schenk, U. Schroeder, and J. M. LeBeau, Appl. Phys. Lett. **106**(16), 162905 (2015).
- ¹²M. H. Park, T. Schenk, C. M. Fancher, E. D. Grimley, C. Zhou, C. Richter, J. M. LeBeau, J. L. Jones, T. Mikolajick, and U. Schroeder, J. Mater. Chem. C 5(19), 4677–4690 (2017).
- ¹³Y. Wei, P. Nukala, M. Salverda, S. Matzen, H. J. Zhao, J. Momand, A. S. Everhardt, G. Agnus, G. R. Blake, and P. Lecoeur, Nat. Mater. 17(12), 1095–1100 (2018).
- ¹⁴R. Materlik, C. Künneth, and A. Kersch, J. Appl. Phys. 117(13), 134109 (2015).
- 15 T. D. Huan, V. Sharma, G. A. Rossetti, Jr., and R. Ramprasad, Phys. Rev. B 90(6), 064111 (2014).
- ¹⁶M. H. Park, Y. H. Lee, H. J. Kim, Y. J. Kim, T. Moon, K. Do Kim, S. D. Hyun, T. Mikolajick, U. Schroeder, and C. S. Hwang, Nanoscale 10(2), 716–725 (2018)
- ¹⁷M. H. Park, Y. H. Lee, T. Mikolajick, U. Schroeder, and C. S. Hwang, Adv. Electron. Mater. 5(3), 1800522 (2019).
- ¹⁸M. H. Park, Y. H. Lee, and C. S. Hwang, Nanoscale 11(41), 19477–19487 (2019).
- ¹⁹M. Materano, T. Mittmann, P. D. Lomenzo, C. Zhou, J. L. Jones, M. Falkowski, A. Kersch, T. Mikolajick, and U. Schroeder, ACS Appl. Electron. Mater. 2(11), 3618–3626 (2020).
- ²⁰R. Batra, T. D. Huan, G. A. Rossetti, Jr., and R. Ramprasad, Chem. Mater. 29(21), 9102–9109 (2017).
- ²¹U. Schroeder, E. Yurchuk, J. Müller, D. Martin, T. Schenk, P. Polakowski, C. Adelmann, M. I. Popovici, S. V. Kalinin, and T. Mikolajick, Japanese J. Appl. Phys. 53(8S1), 08LE02 (2014).
- ²²S. Starschich and U. Boettger, J. Mater. Chem. C 5(2), 333–338 (2017).
- ²³L. Xu, T. Nishimura, S. Shibayama, T. Yajima, S. Migita, and A. Toriumi, J. Appl. Phys. **122**(12), 124104 (2017).
- ²⁴K. D. Kim, Y. H. Lee, T. Gwon, Y. J. Kim, H. J. Kim, T. Moon, S. D. Hyun, H. W. Park, M. H. Park, and C. S. Hwang, Nano Energy 39, 390-399 (2017).
- ²⁵K. Kim, M. Park, H. Kim, Y. Kim, T. Moon, Y. Lee, S. Hyun, T. Gwon, and C. Hwang, J. Mater. Chem. C 4(28), 6864–6872 (2016).
- ²⁶M. Hoffmann, U. Schroeder, T. Schenk, T. Shimizu, H. Funakubo, O. Sakata, D. Pohl, M. Drescher, C. Adelmann, and R. Materlik, J. Appl. Phys. 118(7), 072006 (2015).
- ²⁷S. J. Kim, J. Mohan, J. S. Lee, H. S. Kim, J. Lee, C. D. Young, L. Colombo, S. R. Summerfelt, T. San, and J. Kim, ACS Appl. Mater. Interfaces 11(5), 5208–5214 (2019).
- ²⁸J. Y. Park, K. Yang, D. H. Lee, S. H. Kim, Y. Lee, P. S. Reddy, J. L. Jones, and M. H. Park, J. Appl. Phys. 128(24), 240904 (2020).
- ²⁹G. Catalan, J. Seidel, R. Ramesh, and J. F. Scott, Rev. Mod. Phys. 84(1), 119 (2012).
- 30W. Zheng, K. H. Bowen, J. Li, I. Dąbkowska, and M. Gutowski, J. Phys. Chem. A 109(50), 11521–11525 (2005).
- ³¹R. D. Shannon, Acta Crystallograph. **32**(5), 751–767 (1976).
- ³²F. A. Cotton, G. Wilkinson, C. A. Murillo, M. Bochmann, and R. Grimes, Advanced Inorganic Chemistry (Wiley, 1988).
- ³³O. Ohtaka, H. Fukui, T. Kunisada, T. Fujisawa, K. Funakoshi, W. Utsumi, T. Irifune, K. Kuroda, and T. Kikegawa, J. Am. Ceram. Soc. 84(6), 1369–1373 (2004).

- ³⁴O. Ohtaka, H. Fukui, T. Kunisada, T. Fujisawa, K. Funakoshi, W. Utsumi, T. Irifune, K. Kuroda, and T. Kikegawa, Phys. Rev. B 63(17), 174108 (2001).
- 35D. Shin and Z.-K. Liu, Scr. Materialia 57(3), 201–204 (2007).
- ³⁶L. Lopato, A. Shevchenko, and G. Gerasimyuk, Neorganicheskie Materialy 12(9), 1623–1626 (1976).
- ³⁷L. Komissarova, K. Wang, V. Spitsyn, and Y. P. Simanov, Zh. Neorg. Khim. 9(3), 693–697 (1964).
- ³⁸F. Spiridinov, V. Stepanov, L. Komissarova, and V. Spitsyn, J. Less-Common Met. 14(4), 435–443 (1968).
- ³⁹F. Spiridonov, L. Komissarova, A. Kocharov, and V. Spitsyn, Zh. Neorg. Khim. 14(9), 2535–2540 (1969).
- ⁴⁰A. Shevchenko, L. Lopato, G. Gerasimyuk, and Z. Zaitseva, Izv. Akad. Nauk. SSSR Neorg. Mater. 23(9), 1495 (1987).
- ⁴¹R. Magunov, G. Shklyar, and V. Katridi, Inorg. Mater. **25**(7), 1035–1037 (1989)
- ⁴²M. H. Park, C. C. Chung, T. Schenk, C. Richter, K. Opsomer, C. Detavernier, C. Adelmann, J. L. Jones, T. Mikolajick, and U. Schroeder, Adv. Electron. Mater. 4(7), 1800091 (2018).
- ⁴³M. H. Park, H. J. Kim, G. Lee, J. Park, Y. H. Lee, Y. J. Kim, T. Moon, K. D. Kim, S. D. Hyun, and H. W. Park, Appl. Phys. Rev. 6(4), 041403 (2019).
- ⁴⁴M. H. Park, Y. H. Lee, H. J. Kim, T. Schenk, W. Lee, K. Do Kim, F. P. Fengler, T. Mikolajick, U. Schroeder, and C. S. Hwang, Nanoscale 9(28), 9973–9986 (2017).
- ⁴⁵E. H. Kisi, C. J. Howard, and R. J. Hill, J. Am. Ceram. Soc. 72(9), 1757–1760 (1989)
- ⁴⁶R. Batra, T. D. Huan, J. L. Jones, G. Rossetti, Jr., and R. Ramprasad, J. Phys. Chem. C 121(8), 4139–4145 (2017).
- ⁴⁷E. D. Grimley, T. Schenk, T. Mikolajick, U. Schroeder, and J. M. LeBeau, Adv. Mater. Interfaces 5(5), 1701258 (2018).
- ⁴⁸T. Shimizu, K. Katayama, T. Kiguchi, A. Akama, T. J. Konno, O. Sakata, and H. Funakubo, Sci. Rep. 6(1), 32931 (2016).
- ⁴⁹M. H. Park, H. J. Kim, Y. J. Kim, W. Lee, H. K. Kim, and C. S. Hwang, Appl. Phys. Lett. **102**(11), 112914 (2013).
- ⁵⁰ M. H. Park, H. J. Kim, Y. J. Kim, W. Lee, T. Moon, and C. S. Hwang, Appl. Phys. Lett. **102**(24), 242905 (2013).
- ⁵¹A. Chernikova, M. Kozodaev, A. Markeev, Y. Matveev, D. Negrov, and O. Orlov, Microelectron. Eng. 147, 15–18 (2015).
- ⁵²M. G. Kozodaev, A. G. Chernikova, R. R. Khakimov, M. H. Park, A. M. Markeev, and C. S. Hwang, Appl. Phys. Lett. 113(12), 123902 (2018).
- ⁵³S. J. Kim, D. Narayan, J.-G. Lee, J. Mohan, J. S. Lee, J. Lee, H. S. Kim, Y.-C. Byun, A. T. Lucero, and C. D. Young, Appl. Phys. Lett. 111(24), 242901 (2017).
- ⁵⁴ K. Lee, T. Y. Lee, S. M. Yang, D. H. Lee, J. Park, and S. C. Chae, Appl. Phys. Lett. 112(20), 202901 (2018).
- ⁵⁵L. Xu, T. Nishimura, S. Shibayama, T. Yajima, S. Migita, and A. Toriumi, Appl. Phys. Express 9(9), 091501 (2016).
- ⁵⁶T. Mimura, K. Katayama, T. Shimizu, H. Uchida, T. Kiguchi, A. Akama, T. J. Konno, O. Sakata, and H. Funakubo, Appl. Phys. Lett. 109(5), 052903 (2016).
- 57T. Shimizu, T. Yokouchi, T. Oikawa, T. Shiraishi, T. Kiguchi, A. Akama, T. J. Konno, A. Gruverman, and H. Funakubo, Appl. Phys. Lett. 106(11), 112904 (2015).
- ⁵⁸ R. Batra, H. D. Tran, and R. Ramprasad, Appl. Phys. Lett. **108**(17), 172902 (2016).
- ⁵⁹S. Starschich and U. Böttger, J. Appl. Phys. **123**(4), 044101 (2018).
- ⁶⁰S. Starschich, T. Schenk, U. Schroeder, and U. Boettger, Appl. Phys. Lett. 110(18), 182905 (2017).
- ⁶¹T. Mimura, T. Shimizu, and H. Funakubo, Appl. Phys. Lett. **115**(3), 032901 (2019).
- ⁶²M. Kohli, P. Muralt, and N. Setter, Appl. Phys. Lett. **72**(24), 3217–3219 (1998).
- ⁶³N. Menou, C. Muller, I. S. Baturin, V. Y. Shur, and J.-L. Hodeau, J. Appl. Phys. **97**(6), 064108 (2005).
- ⁶⁴F. C. Kartawidjaja, C. H. Sim, and J. Wang, J. Appl. Phys. **102**(12), 124102 (2007).
- ⁶⁵G. L. Yuan, J.-M. Liu, S. T. Zhang, D. Wu, Y. P. Wang, Z. G. Liu, H. L. W. Chan, and C. L. Choy, Appl. Phys. Lett. 84(6), 954–956 (2004).

- ⁶⁶D. Zhou, J. Xu, Q. Li, Y. Guan, F. Cao, X. Dong, J. Müller, T. Schenk, and U. Schröder, Appl. Phys. Lett. **103**(19), 192904 (2013).
- ⁶⁷A. Chouprik, M. Spiridonov, S. Zarubin, R. Kirtaev, V. Mikheev, Y. Lebedinskii, S. Zakharchenko, and D. Negrov, ACS Appl. Electron. Mater. 1(3), 275–287 (2019).
- ⁶⁸ H. J. Kim, M. H. Park, Y. J. Kim, Y. H. Lee, T. Moon, K. Do Kim, S. D. Hyun, and C. S. Hwang, Nanoscale 8(3), 1383–1389 (2016).
- ⁶⁹M. H. Park, H. J. Kim, Y. J. Kim, Y. H. Lee, T. Moon, K. Do Kim, S. D. Hyun, F. Fengler, U. Schroeder, and C. S. Hwang, ACS Appl. Mater. Interfaces 8(24), 15466–15475 (2016).
- ⁷⁰ M. H. Park, H. J. Kim, Y. J. Kim, Y. H. Lee, T. Moon, K. Do Kim, S. D. Hyun, and C. S. Hwang, Appl. Phys. Lett. **107**(19), 192907 (2015).
- ⁷¹T. Schenk, M. Hoffmann, J. Ocker, M. Pešić, T. Mikolajick, and U. Schroeder, ACS Appl. Mater. Interfaces 7(36), 20224–20233 (2015).
- 72 T. Schenk, U. Schroeder, M. Pešić, M. Popovici, Y. V. Pershin, and T. Mikolajick, ACS Appl. Mater. Interfaces 6(22), 19744–19751 (2014).
- ⁷³S. Starschich, S. Menzel, and U. Böttger, J. Appl. Phys. **121**(15), 154102 (2017)
- ⁷⁴P. D. Lomenzo, P. Zhao, Q. Takmeel, S. Moghaddam, T. Nishida, M. Nelson, C. M. Fancher, E. D. Grimley, X. H. Sang, J. M. LeBeau, and J. L. Jones, J. Vacuum Sci. Technol. B 32(3), 03D123 (2014).
- ⁷⁵M. Pešić, F. P. G. Fengler, L. Larcher, A. Padovani, T. Schenk, E. D. Grimley, X. Sang, J. M. LeBeau, S. Slesazeck, U. Schroeder, and T. Mikolajick, Adv. Funct. Mater. 26(25), 4601–4612 (2016).
- ⁷⁶S. Clima, D. J. Wouters, C. Adelmann, T. Schenk, U. Schroeder, M. Jurczak, and G. Pourtois, Appl. Phys. Lett. **104**(9), 092906 (2014).
- 78. V. Barabash, D. Pramanik, Y. Zhai, B. Magyari-Kope, and Y. Nishi, ECS Trans. 75(32), 107–121 (2017).
- ⁷⁸S. E. Reyes-Lillo, K. F. Garrity, and K. M. Rabe, Phys. Rev. B **90**(14), 140103(R) (2014).
- ⁷⁹S. Dutta, H. Aramberri, T. Schenk, and J. Íñiguez, Physica Status Solidi (RRL) 14(6), 2000047 (2020).
- ⁸⁰P. Fan, Y. K. Zhang, Q. Yang, J. Jiang, L. M. Jiang, M. Liao, and Y. C. Zhou, J. Phys. Chem. C 123(35), 21743–21750 (2019).
- ⁸¹S. Goedecker, J. Chem. Phys. **120**(21), 9911–9917 (2004).
- 82 S. V. Barabash, J. Comput. Electron. 16(4), 1227–1235 (2017).
- 83Y. Kudoh, H. Takeda, and H. Arashi, Phys. Chem. Miner. 13(4), 233–237 (1986).
- 84D. M. Adams, S. Leonard, D. R. Russell, and R. J. Cernik, J. Phys. Chem. Solids 52(9), 1181–1186 (1991).
- 85T. Maeda, B. Magyari-Kope, and Y. Nishi, in 2017 IEEE International Memory Workshop (IMW) (IEEE, 2017).
- ⁸⁶V. Fridkin and S. Ducharme, Phys. Solid State **43**(7), 1320–1324 (2001).
- 87 M. H. Park, H. J. Kim, Y. H. Lee, Y. J. Kim, T. Moon, K. Do Kim, S. D. Hyun, and C. S. Hwang, Nanoscale 8(29), 13898–13907 (2016).
- ⁸⁸M. H. Park, Y. H. Lee, H. J. Kim, Y. J. Kim, T. Moon, K. D. Kim, S. D. Hyun, and C. S. Hwang, ACS Appl. Mater. Interfaces 10(49), 42666–42673 (2018).
- 89 J. E. Daniels, C. Cozzan, S. Ukritnukun, G. Tutuncu, J. Andrieux, J. Glaum, C. Dosch, W. Jo, and J. L. Jones, J. Appl. Phys. 115(22), 224104 (2014).
- ⁹⁰J. E. Daniels, T. R. Finlayson, M. Davis, D. Damjanovic, A. J. Studer, M. Hoffman, and J. L. Jones, J. Appl. Phys. **101**(10), 104108 (2007).
- ⁹¹W. Ding, Y. Zhang, L. Tao, Q. Yang, and Y. Zhou, Acta Materialia 196, 556–564 (2020).
- ⁹²H.-J. Lee, M. Lee, K. Lee, J. Jo, H. Yang, Y. Kim, S. C. Chae, U. Waghmare, and J. H. Lee, Science 369(6509), 1343–1347 (2020).
- ⁹³M. H. Park, H. J. Kim, Y. J. Kim, W. Lee, T. Moon, K. D. Kim, and C. S. Hwang, Appl. Phys. Lett. **105**(7), 072902 (2014).
- ⁹⁴T. Kiguchi, T. Shiraishi, T. Shimizu, H. Funakubo, and T. J. Konno, Jpn. J. Appl. Phys. 57(11S), 11UF16 (2018).
- 95T. Y. Lee, K. Lee, H. H. Lim, M. S. Song, S. M. Yang, H. K. Yoo, D. I. Suh, Z. Zhu, A. Yoon, M. R. MacDonald, X. Lei, H. Y. Jeong, D. Lee, K. Park, J. Park, and S. C. Chae, ACS Appl Mater Interfaces 11(3), 3142–3149 (2019).
- ⁹⁶R. R. Keller and R. H. Geiss, J. Microscopy **245**(3), 245–251 (2012).
- ⁹⁷M. Lederer, T. Kämpfe, R. Olivo, D. Lehninger, C. Mart, S. Kirbach, T. Ali, P. Polakowski, L. Roy, and K. Seidel, Appl. Phys. Lett. 115(22), 222902 (2019).
- ⁹⁸M. Lederer, T. Kämpfe, N. Vogel, D. Utess, B. Volkmann, T. Ali, R. Olivo, J. Müller, S. Beyer, and M. Trentzsch, Nanomaterials 10(2), 384 (2020).

- ⁹⁹K. Katayama, T. Shimizu, O. Sakata, T. Shiraishi, S. Nakamura, T. Kiguchi, A. Akama, T. J. Konno, H. Uchida, and H. Funakubo, J. Appl. Phys. 119(13), 134101 (2016)
- ¹⁰⁰T. Shimizu, T. Mimura, T. Kiguchi, T. Shiraishi, T. Konno, Y. Katsuya, O. Sakata, and H. Funakubo, Appl. Phys. Lett. 113(21), 212901 (2018).
- ¹⁰¹H. A. Hsain, P. Sharma, H. Yu, J. L. Jones, F. So, and J. Seidel, Appl. Phys. Lett. 113(2), 022905 (2018).
- 102P. Buragohain, C. Richter, T. Schenk, H. Lu, T. Mikolajick, U. Schroeder, and A. Gruverman, Appl. Phys. Lett. 112(22), 222901 (2018).
- 103 Z. Quan, M. Wang, X. Zhang, H. Liu, W. Zhang, and X. Xu, AIP Adv. 10(8), 085024 (2020).
- 104 R. K. Vasudevan, N. Balke, P. Maksymovych, S. Jesse, and S. V. Kalinin, Appl. Phys. Rev. 4(2), 021302 (2017).
- ¹⁰⁵H. Yokokawa, N. Sakai, T. Kawada, and M. Dokiya, Sci. Technol. Zirconia V 1993, 59–68.
- 106Phase Equilibria Diagrams Online Database (NIST Standard Reference Database 31), The American Ceramic Society and the National Institute of Standards and Technology (the ACerS) (2021); www.nist.gov/srd.nist31.cfm.
- ¹⁰⁷D. J. Kim, J. Am. Ceram. Soc. **72**(8), 1415–1421 (1989).
- ¹⁰⁸W. J. Merz, Phys. Rev. **95**(3), 690 (1954).
- 109 H. Orihara, S. Hashimoto, and Y. Ishibashi, J. Phys. Soc. Jpn. 63(3), 1031–1035 (1994).
- no A. N. Kolmogorov, Bull. Acad. Sci. USSR, Math. Ser. 1(3), 355–359 (1937).
- ¹¹¹M. Avrami, J. Chem. Phys. **8**(2), 212–224 (1940).
- ¹¹²V. Shur, E. Rumyantsev, and S. Makarov, J. Appl. Phys. **84**(1), 445–451 (1998).
- 113 V. Y. Shur and E. L. Rumyantsev, Ferroelectrics 151(1), 171–180 (1994).
- ¹¹⁴V. Y. Shur and E. L. Rumyantsev, Ferroelectrics **142**(1), 1–7 (1993).
- ¹¹⁵E. J. Guo, K. Dörr, and A. Herklotz, Appl. Phys. Lett. **101**(24), 242908 (2012).
- ¹¹⁶J. Y. Jo, S. M. Yang, T. H. Kim, H. N. Lee, J. G. Yoon, S. Park, Y. Jo, M. H. Jung, and T. W. Noh, Phys. Rev. Lett. **102**(4), 045701 (2009).
- 117Y. W. So, D. J. Kim, T. W. Noh, J.-G. Yoon, and T. K. Song, Appl. Phys. Lett. 86(9), 092905 (2005).
- ¹¹⁸A. K. Tagantsev, I. Stolichnov, N. Setter, J. S. Cross, and M. Tsukada, Phys. Rev. B 66(21), 214109 (2002).
- ¹¹⁹S. Mueller, S. R. Summerfelt, J. Muller, U. Schroeder, and T. Mikolajick, IEEE Electron Device Lett. 33(9), 1300–1302 (2012).
- ¹²⁰S. D. Hyun, H. W. Park, Y. J. Kim, M. H. Park, Y. H. Lee, H. J. Kim, Y. J. Kwon, T. Moon, K. D. Kim, Y. B. Lee, B. S. Kim, and C. S. Hwang, ACS Appl Mater Interfaces 10(41), 35374–35384 (2018).
- ¹²¹K. Lee, H. J. Lee, T. Y. Lee, H. H. Lim, M. S. Song, H. K. Yoo, D. I. Suh, J. G. Lee, Z. Zhu, A. Yoon, M. R. MacDonald, X. Lei, K. Park, J. Park, J. H. Lee, and S. C. Chae, ACS Appl Mater Interfaces 11(42), 38929–38936 (2019).
- 122M. Materano, P. D. Lomenzo, H. Mulaosmanovic, M. Hoffmann, A. Toriumi, T. Mikolajick, and U. Schroeder, Appl. Phys. Lett. 117(26), 262904 (2020).
- 123 H. Mulaosmanovic, J. Ocker, S. Müller, U. Schroeder, J. Müller, P. Polakowski, S. Flachowsky, R. van Bentum, T. Mikolajick, and S. Slesazeck, ACS Appl. Mater. Interfaces 9(4), 3792–3798 (2017).
- 124 Y.-C. Chen, Q. Lin, and Y. Chu, Appl. Phys. Lett. 94(12), 122908 (2009).
- 125J. Y. Son, C. S. Park, S. K. Kim, and Y. H. Shin, J. Appl. Phys. 104(6), 064101 (2008)
- 126Y. Kim, W. Kim, H. Choi, S. Hong, H. Ko, H. Lee, and K. No, Appl. Phys. Lett. 96(1), 012908 (2010).
- ¹²⁷S. Zhukov, Y. A. Genenko, and H. von Seggern, J. Appl. Phys. **108**(1), 014106 (2010).
- 128 A. Q. Jiang, H. J. Lee, C. S. Hwang, and J. F. Scott, Adv. Funct. Mater. 22(1), 192–199 (2012).
- 129 M. H. Park and C. S. Hwang, Rep. Prog. Phys. 82(12), 124502 (2019).
- ¹³⁰M. H. Park, T. Schenk, M. Hoffmann, S. Knebel, J. Gärtner, T. Mikolajick, and U. Schroeder, Nano Energy 36, 381–389 (2017).
- ¹⁵¹M. H. Park, H. J. Kim, Y. J. Kim, T. Moon, K. D. Kim, and C. S. Hwang, Adv. Energy Mater. 4(16), 1400610 (2014).
- ¹³²M. H. Park, H. J. Kim, Y. J. Kim, T. Moon, K. D. Kim, Y. H. Lee, S. D. Hyun, and C. S. Hwang, Adv. Mater. 28(36), 7956–7961 (2016).
- 133M. Hoffmann, U. Schroeder, C. Künneth, A. Kersch, S. Starschich, U. Böttger, and T. Mikolajick, Nano Energy 18, 154–164 (2015).

- 134P. D. Lomenzo, S. Slesazeck, M. Hoffmann, T. Mikolajick, U. Schroeder, and B. Max, in 2019 19th Non-Volatile Memory Technology Symposium (NVMTS) (IEEE, 2019), pp. 1–8.
- 135S. Ducharme, V. M. Fridkin, A. V. Bune, S. Palto, L. Blinov, N. Petukhova, and S. Yudin, Phys. Rev. Lett. 84(1), 175 (2000).
- 136 L. Landau and I. Khalatnikov, Dokl. Akad. Nauk SSSR **96**(469), 25 (1954).
- 137D. Ricinschi, C. Harnagea, C. Papusoi, L. Mitoseriu, V. Tura, and M. Okuyama, J. Phys.: Condens. Matter 10(2), 477 (1998).
- 138 M. Hoffmann, M. Pešić, K. Chatterjee, A. I. Khan, S. Salahuddin, S. Slesazeck, U. Schroeder, and T. Mikolajick, Adv. Funct. Mater. 26(47), 8643–8649 (2016).
- 139 A. K. Saha, K. Ni, S. Dutta, S. Datta, and S. Gupta, Appl. Phys. Lett. 114(20), 202903 (2019).
- ¹⁴⁰R. Landauer, J. Appl. Phys. **28**(2), 227–234 (1957).
- ¹⁴¹X. Du and I.-W. Chen, MRS Online Proc. Library Archive **493**, 261–266 (1997).
- 142 I. Ford, Proc. Inst. Mech. Eng., Part C: J. Mech. Eng. Sci. 218(8), 883–899 (2004).
- ¹⁴³K. Kimura and H. Ohigashi, Japanese J. Appl. Phys. **25**(3R), 383 (1986).
- ¹⁴⁴H. Kay and J. Dunn, Philosoph. Mag. 7(84), 2027–2034 (1962).
- 145 A. K. Tagantsev, Ferroelectrics 184(1), 79–88 (1996).
- 146 A. K. Tagantsev, Integrated Ferroelectrics 16(1-4), 237-244 (1997).
- ¹⁴⁷A. Toriumi, L. Xu, Y. Mori, X. Tian, P. D. Lomenzo, H. Mulaosmanovic, M. Materano, T. Mikolajick, and U. Schroeder, 2019 IEEE International Electron Devices Meeting (IEDM) (2019), pp. 15.11.11–15.11.14.
- 148U. Schroeder, C. S. Hwang, and H. Funakubo, Ferroelectricity in Doped Hafnium Oxide: Materials, Properties and Devices (Woodhead Publishing, 2019)
- 149J. Lyu, I. Fina, R. Solanas, J. Fontcuberta, and F. Sánchez, ACS Appl. Electron. Mater. 1(2), 220–228 (2019).
- 150H. Mulaosmanovic, E. Chicca, M. Bertele, T. Mikolajick, and S. Slesazeck, Nanoscale 10(46), 21755–21763 (2018).
- 151S.-M. Yoon, E. Tokumitsu, and H. Ishiwara, IEEE Electron Device Lett. 20(10), 526–528 (1999)
- 152S. Boyn, J. Grollier, G. Lecerf, B. Xu, N. Locatelli, S. Fusil, S. Girod, C. Carrétéro, K. Garcia, S. Xavier, J. Tomas, L. Bellaiche, M. Bibes, A. Barthélémy, S. Saïghi, and V. Garcia, Nat. Commun. 8, 14736 (2017).
- ¹⁵³G. W. Burr, R. M. Shelby, A. Sebastian, S. Kim, S. Sidler, K. Virwani, M. Ishii, P. Narayanan, A. Fumarola, L. L. Sanches, I. Boybat, M. L. Gallo, K. Moon, J. Woo, H. Hwang, and Y. Leblebici, Adv. Phys.-X 2(1), 89–124 (2017).
- 154S. Dutta, C. Schafer, J. Gomez, K. Ni, S. Joshi, and S. Datta, Front. Neurosci. 14, 634 (2020).
- 155R. Guo, W. N. Lin, X. B. Yan, T. Venkatesan, and J. S. Chen, Appl. Phys. Rev. 7(1), 011304 (2020).
- 156 D. S. Jeong and C. S. Hwang, Adv. Mater. 30(42), 1704729 (2018).
- 157D. S. Jeong, K. M. Kim, S. Kim, B. J. Choi, and C. S. Hwang, Adv. Electron. Mater. 2(9), 1600090 (2016).
- 158 M. K. Kim and J. S. Lee, Nano Lett. 19(3), 2044–2050 (2019).
- 159 Y. B. Li, Z. R. Wang, R. Midya, Q. F. Xia, and J. J. Yang, J. Phys. D-Appl. Phys. 51(50), 503002 (2018).
- ¹⁶⁰V. Mikheev, A. Chouprik, Y. Lebedinskii, S. Zarubin, Y. Matveyev, E. Kondratyuk, M. G. Kozodaev, A. M. Markeev, A. Zenkevich, and D. Negrov, ACS Appl. Mater. Interfaces 11(35), 32108–32114 (2019).
- 161H. Mulaosmanovic, J. Ocker, S. Müller, M. Noack, J. Müller, P. Polakowski, T. Mikolajick, and S. Slesazeck, 2017 Symposium on VLSI Technology (2017), pp. 7176. 7177
- pp. T176–T177.

 162S. Oh, H. Hwang, and I. K. Yoo, APL Mater. 7(9), 091109 (2019).
- 163S. Oh, T. Kim, M. Kwak, J. Song, J. Woo, S. Jeon, I. K. Yoo, and H. Hwang, IEEE Electron Device Lett. 38(6), 732–735 (2017).
- 164 G. L. Tian, J. S. Bi, G. B. Xu, K. Xi, Y. N. Xu, X. Q. Yang, H. X. Yin, Q. X. Xu, and Y. L. Li, Electron. Lett. 56(16), 840–842 (2020).
- 165 S. M. Yu, Proc. IEEE 106(2), 260–285 (2018).
- ¹⁶⁶M. H. Park, Y. H. Lee, H. J. Kim, Y. J. Kim, T. Moon, K. Do Kim, J. Müller, A. Kersch, U. Schroeder, T. Mikolajick, and C. S. Hwang, Adv. Mater. 27(11), 1811–1831 (2015).
- 167 J. Müller, P. Polakowski, S. Mueller, and T. Mikolajick, ECS J. Solid State Sci. Technol. 4(5), N30-N35 (2015).
- 168M. Pešić, M. Hoffmann, C. Richter, T. Mikolajick, and U. Schroeder, Adv. Funct. Mater. 26(41), 7486–7494 (2016).

- ¹⁶⁹P. Polakowski, S. Riedel, W. Weinreich, M. Rudolf, J. Sundqvist, K. Seidel, and J. Muller, 2014 IEEE 6th International Memory Workshop (IMW) (2014), pp. 1–4.
- 170 X. Tian and A. Toriumi, 2017 IEEE Electron Devices Technology and Manufacturing Conference (EDTM) (2017), pp. 36–64.
- ¹⁷¹S. Fujii, Y. Kamimuta, T. Ino, Y. Nakasaki, R. Takaishi, and M. Saitoh, 2016 IEEE Symposium on VLSI Technology (2016), pp. 1–2.
- ¹⁷²Z. P. Dong, X. Cao, T. Wu, and J. Guo, J. Appl. Phys. **123**(9), 094501 (2018).
- 173B. Max, M. Hoffmann, S. Slesazeck, and T. Mikolajick, 2018 48th European Solid-State Device Research Conference (ESSDERC) (2018), pp. 142–145.
- 174). Yoon, S. Hong, Y. W. Song, J.-H. Ahn, and S.-E. Ahn, Appl. Phys. Lett. 115(15), 153502 (2019).
- 175 A. L. Esaki, R. Laibowitz, and P. Stiles, IBM Tech. Discl. Bull. 13(2161), 114 (1971).
- 176A. Gruverman, D. Wu, H. Lu, Y. Wang, H. W. Jang, C. M. Folkman, M. Y. Zhuravlev, D. Felker, M. Rzchowski, C. B. Eom, and E. Y. Tsymbal, Nano Lett. 9(10), 3539–3543 (2009).
- 177V. Garcia, S. Fusil, K. Bouzehouane, S. Enouz-Vedrenne, N. D. Mathur, A. Barthélémy, and M. Bibes, Nature 460(7251), 81–84 (2009).
- ¹⁷⁸A. Chanthbouala, A. Crassous, V. Garcia, K. Bouzehouane, S. Fusil, X. Moya, J. Allibe, B. Dlubak, J. Grollier, S. Xavier, C. Deranlot, A. Moshar, R. Proksch, N. D. Mathur, M. Bibes, and A. Barthélémy, Nat. Nanotechnol. 7(2), 101–104 (2012).
- ¹⁷⁹A. Dörfler, G. Kolhatkar, U. Wagner, and A. Ruediger, J. Phys.: Condens. Matter 32(18), 185302 (2020).
- ¹⁸⁰V. Garcia and M. Bibes, Nat. Commun. 5, 4289 (2014).
- ¹⁸¹V. Garcia, M. Bibes, L. Bocher, S. Valencia, F. Kronast, A. Crassous, X. Moya, S. Enouz-Vedrenne, A. Gloter, D. Imhoff, C. Deranlot, N. D. Mathur, S. Fusil, K. Bouzehouane, and A. Barthélémy, Science 327(5969), 1106–1110 (2010).
- ¹⁸²D. J. Kim, H. Lu, S. Ryu, C. W. Bark, C. B. Eom, E. Y. Tsymbal, and A. Gruverman, Nano Lett. 12(11), 5697–5702 (2012).
- ¹⁸³M. Kobayashi, Y. Tagawa, F. Mo, T. Saraya, and T. Hiramoto, IEEE J. Electron Devices Soc. 7, 134–139 (2019).
- ¹⁸⁴M. Y. Zhuravlev, A. Alexandrov, L. L. Tao, and E. Y. Tsymbal, Appl. Phys. Lett. 113(17), 172405 (2018).

- ¹⁸⁵S. Slesazeck and T. Mikolajick, Nanotechnology **30**(35), 352003 (2019).
- 186B. Max, M. Hoffmann, S. Slesazeck, and T. Mikolajick, IEEE J. Electron Devices Soc. 7, 1175–1181 (2019).
- 187B. Max, T. Mikolajick, M. Hoffmann, and S. Slesazeck, 2019 IEEE 11th International Memory Workshop (IMW) (2019), pp. 1–4.
- 188B. Max, M. Hoffmann, S. Slesazeck, and T. Mikolajick, Electron. Lett. 56(21), 1108–1110 (2020).
- 189B. Max, M. Hoffmann, H. Mulaosmanovic, S. Slesazeck, and T. Mikolajick, ACS Appl. Electron. Mater. 2(12), 4023–4033 (2020).
- ¹⁹⁰H. Ryu, H. N. Wu, F. B. Rao, and W. J. Zhu, Sci. Rep. **9**, 20383 (2019).
- ¹⁹¹A. Chernikova, M. Kozodaev, A. Markeev, D. Negrov, M. Spiridonov, S. Zarubin, O. Bak, P. Buragohain, H. D. Lu, E. Suvorova, A. Gruverman, and A. Zenkevich, ACS Appl. Mater. Interfaces 8(11), 7232–7237 (2016).
- 192F. Ambriz-Vargas, G. Kolhatkar, R. Thomas, R. Nouar, A. Sarkissian, C. Gomez-Yáñez, M. Gauthier, and A. Ruediger, Appl. Phys. Lett. 110(9), 093106 (2017).
- 193 Z. Krivokapic, U. Rana, R. Galatage, A. Razavieh, A. Aziz, J. Liu, J. Shi, H. Kim, R. Sporer, and C. Serrao, 2017 IEEE International Electron Devices Meeting (IEDM) (2017), pp. 15.11.11–15.11.14.
- 194H. Mulaosmanovic, S. Slesazeck, J. Ocker, M. Pesic, S. Muller, S. Flachowsky, J. Müller, P. Polakowski, J. Paul, and S. Jansen, 2015 IEEE International Electron Devices Meeting (IEDM) (2015), pp. 26.28.21–26.28.23.
- ¹⁹⁵H. J. Kim, M. H. Park, Y. J. Kim, Y. H. Lee, W. Jeon, T. Gwon, T. Moon, K. Do Kim, and C. S. Hwang, Appl. Phys. Lett. **105**(19), 192903 (2014).
- ¹⁹⁶H. Mulaosmanovic, E. T. Breyer, T. Mikolajick, and S. Slesazeck, IEEE Trans. Electron Devices 66(9), 3828–3840 (2019).
- 197 H. Mulaosmanovic, S. Dünkel, M. Trentzsch, S. Beyer, E. T. Breyer, T. Mikolajick, and S. Slesazeck, IEEE Trans. Electron Devices 67(12), 5804–5809 (2020).
- ¹⁹⁸B. T. Lin, Y. W. Lu, J. Shieh, and M. J. Chen, J. Eur. Ceram. Soc. 37(3), 1135–1139 (2017).
- ¹⁹⁹M. H. Park, H. J. Kim, Y. J. Kim, T. Moon, and C. S. Hwang, Appl. Phys. Lett. 104(7), 072901 (2014).